Intersystem Crossing in Acetylene:
A Mechanistic Study

by

Selen Altunata

Submitted to the Department of Chemistry
in partial fulfillment of the requirements for the degree of

Doctor of Philosophy

at the

MASSACHUSETTS INSTITUTE OF TECHNOLOGY

July 2001
[September 2001]

Author ....
Department of Chemistry
July 27, 2001

Certified by... ....
Robert W. Field
Haslam and Dewey Professor of Chemistry
Thesis Supervisor

Accepted by ....
Robert W. Field
Chairman, Department Committee on Graduate Students

Intersystem Crossing in Acetylene:
A Mechanistic Study

by

Selen Altunata

Submitted to the Department of Chemistry
on July 27, 2001, in partial fulfillment of the
requirements for the degree of
Doctor of Philosophy

Abstract

The triplet electronic states of acetylene and the intersystem crossing process that populates these states were studied using a second-generation, supersonic jet molecular beam machine with a multispectral capability. Surface Electron Ejection (SEELEM), Ultraviolet Laser Induced Fluorescence (UV-LIF), and Infrared Laser Induced Fluorescence (IR-LIF) spectra were acquired simultaneously following excitation in the vicinity of the $\tilde{A}^1A_u$ $\nu_3 = 3 \leftarrow \tilde{X}^1\Sigma_g^+$ $\nu_4 = 0$ transition of acetylene. The $\tilde{A}^1A_u$ $\nu_3 = 3$ level of acetylene is known to be coupled strongly to a background of near-degenerate triplet states. Simultaneous analysis of the complementary SEELEM and UV-LIF data using a set of recently developed analytical tools, yielded mechanistic insights into the non-radiative relaxation (*i.e.* intersystem crossing) process that distributes the optically accessible bright state over the background of dark states. The potential of the IR-LIF signal as an indirect probe of the triplet states of acetylene has also been demonstrated. Mechanistic insights into the SEELEM detection process itself were gained through a comparison of SEELEM data obtained separately in the first-generation and second-generation molecular beam machines. The two versions of the apparatus differed in their respective operating pressures. The operating background pressure has been found to be an important external factor in the SEELEM process. The much higher sensitivity (a factor of 10^3) of low-work function SEELEM surfaces such as Cs ($\Phi = 2.1$ eV) compared to that of other metals such as Au ($\Phi = 5.1$ eV) is observed only under low operating background pressures (4×10^{-7} Torr).

Thesis Supervisor: Robert W. Field
Title: Haslam and Dewey Professor of Chemistry

Acknowledgments

I would like to extend my warmest thanks to my advisor Robert W. Field for his enthusiasm, guidance, understanding, valuable insights, encouragement, and positivism throughout this project. It has been a unique and most pleasant experience working with him.

I would also like to acknowledge all of my teachers whose contributions to my education throughout the years have provided me with a firm basis I can always rely on.

I would like to thank my parents, in their native language Turkish, for raising me the way I am:

Sevgili Annem ve Babam,

Beni kendine güvenli, tutarli, hayat dolu biri olarak sevgi içinde yetiştirdiğiniz için size en içten teşekkürlerimi sunuyorum. Bugüne sizin hiçbir zaman eksik olmayan sevgi ve desteğinizin kanatlari altinda ulaştim.

I would like to thank all the excellent scientists I have had the privilege to interact with in regards to my project: Dr. Manjula Canagaratna, Dr. Kevin L. Cunningham, Ryan Thom, Dr. Stephen Drucker, Dr. Gabe Morgan, and Dr. Sergey Panov.

I would like to thank the past and present members of the Robert W. Field group for all the wonderful memories I am taking with me.

I would like to thank my younger brother, Serhan, for being a great buddy since the day he was born. It was his optimism and sense of humor that helped me through the turbulences of graduate school.

I would like to thank Chel for being a wonderful source of support and inspiration during the conclusion of this research. I would like to thank him for his patience as he was subjected to regular updates about my research-related progress, concerns, and frustrations. I would like to thank him for being genuinely interested in hearing about a field he is foreign to. I would like to thank him for always managing to put a smile on my face even when I am in the mood to sulk.

I would like to thank my thesis committee for accompanying me in the final phase

of the biggest (so far) chapter in my life.

For World Peace

Contents

List of Figures

List of Tables

Chapter 1

Introduction

1.1 Objective

The main goal of the project described in this thesis is to develop experimental and analytical capabilities to study the properties of small gas phase molecules in long-lived "metastable" ($\tau > 100\mu$s), electronically excited ($E_{elect} > 2$ eV) states. Of particular interest is understanding the mechanism of the non-radiative electronic relaxation (*i.e.* intersystem crossing) process that populates the electronically excited, metastable states of small molecules.

The primary experimental apparatus of this project is a two-chamber vacuum system, which houses a pulsed, skimmed, supersonic molecular beam, equipped with four complementary detection schemes:

1) Surface Electron Ejection by Laser Excited Metastable Molecules (*SEELEM*) - In this detection scheme, long-lived, electronically excited molecules (*i.e.* metastable molecules) collide with a metal surface and transfer their electronic excitation energy to the surface. If this energy exceeds the work function of the metal, an electron is ejected and detected. The molecules traverse a flight zone ($\sim$ 12 - 22 cm) before colliding with the SEELEM surface. Only molecules that do not lose their electronic excitation energy in transit give rise to a SEELEM signal. Therefore, the SEELEM channel has selectivity for long-lived molecules (in our apparatus the lifetime τ of the metastable states detected by SEELEM can vary from $> 40\mu$s to $> 100\mu$ depending

on the exact location of the SEELEM surface with respect to the laser excitation region).

The two largest contributions to the SEELEM detection process are dipole-dipole (long-range) and exchange (short-range) interactions [58]. The matrix elements governing these interactions are given in Eq. (1.1).

$$\begin{aligned} < H >_{dipole-dipole} &= [\int\int U_F^*(2)U_G^*(1)(e^2/r_{12})U_E(1)U_M(2)d\tau_1 d\tau_2] \\ &\quad \times[\int \chi_G^*\chi_E d\tau_{vib}] \\ < H >_{exchange} &= [\int\int U_F^*(1)U_G^*(2)(e^2/r_{12})U_E(1)U_M(2)d\tau_1 d\tau_2] \\ &\quad \times[\int \chi_G^*\chi_E d\tau_{vib}] \end{aligned} \tag{1.1}$$

The integrations in Eq. (1.1) are over the space and spin variables of the two electrons and all of the vibrational coordinates of the molecule.

The ejection of an electron from the SEELEM detector surface by a molecule which is vibrationally hot but is not electronically excited, will be much less efficient. Hagstrum shows that ejection of an electron by simple transfer of kinetic energy to the surface occurs much closer to the surface than the dipole-dipole and exchange interactions and does not become important until the incident species has >100 eV of kinetic energy [53]. The average kinetic energy in molecular vibration is approximately 1/2 the total vibrational energy [58]. Since we are only concerned with excitation energies ≤ 10 eV in our experiments, the maximum average kinetic energy in vibration is 5 eV. Therefore, if the excitation energy does not remain localized in electronic energy, the molecule will not be efficiently detected. In other words, in the excitation energy regime relevant to our experiments, vibrational energy is not expected to contribute to the SEELEM signal.

2) Time-of-Flight Spectra (*TOF*) - We can monitor the arrival of the metastable species at the SEELEM surface as a function of time. This capability allows us to distinguish intact metastable molecules from earlier-arriving species (*i.e.* metastable photofragments).

3) Infrared Laser Induced Fluorescence (*IR-LIF*) - A Germanium near infrared (800 - 1700 nm) detector that views the laser excitation region directly, collects the infrared component of the fluorescence from molecules excited by a UV-tunable laser.

4) Ultraviolet Laser Induced Fluorescence (*UV-LIF*) - A photomultiplier tube (190 - 500 nm) that views the laser excitation region directly, collects the UV component of the fluorescence from the laser excited molecules.

The *multispectral* capability of the experimental apparatus provides unique insights into the electronic character of the metastable molecules that are created upon laser excitation. Each molecular eigenstate can be a mixture of several electronic states (excited singlet state S_1, lowest triplet state T_1, excited triplet state T_i (i>1), and electronic ground state S_0). Each detection channel described previously has different detectivities for the fractional characters of each type of electronic state. For example, the UV-LIF channel serves as a probe of the fractional singlet character (or bright state character) since it is the singlet fractional character that gives rise to the UV-fluorescence signal. The SEELEM channel, on the other hand, serves as a probe of the dark state (*i.e.* triplet) character of the eigenstates since it is the dark state character that renders a state long-lived (the lifetime of a pure singlet state is on the order of 300 ns whereas that of a pure triplet state is on the order of tens of ms [68]) and, hence, SEELEM-detectable. Simultaneous analysis of the *complementary* data from the different channels using our recently developed statistical pattern-recognition methods allows us to understand the fundamental excitation and decay mechanisms that govern intramolecular energy flow.

1.2 The Model System - Acetylene

Acetylene (HCCH), in its ground state, is a centrosymmetric molecule that belongs to the point group of $D_{\infty h}$ and electric dipole-transitions are restricted by the $g \leftrightarrow u$ selection rule. In the ground state the acetylene molecule is linear and has the electronic configuration

$$(1\sigma_g)^2(1\sigma_u)^2(2\sigma_g)^2(2\sigma_u)^2(3\sigma_g)^2(1\pi_u)^4$$

The LUMO of acetylene is π_g^*. The excited electronic states can have either *cis* or *trans* geometry. The ground potential energy surface of acetylene also has a second minimum, the vinylidene isomer, which lies at $T_e = 15770 \pm 230$ cm^{-1} [110] above the linear geometry and corresponds to a structure in which both hydrogens are attached to the same carbon. The labels of the potential energy surfaces of acetylene, which are ordered in increasing energy of excitation, are:

$$\begin{array}{cc} {}^1\Sigma_g^+ & S_0 \\ \tilde{a}^3B_2 & cis - T_1 \\ \tilde{a}^3B_u & trans - T_1 \\ \tilde{b}^3A_u & trans - T_2 \\ \tilde{b}^3A_2 & cis - T_2 \\ \tilde{A}^1A_u & trans - S_1 \end{array}$$

Figure 1-1 shows the normal modes of vibration and the principal axes of acetylene in the linear and *trans*−bent geometries. The *trans*−bending mode, which is most important in the present project, is $\nu_4(\pi_g)$ for the linear molecule and $\nu_3(a_g)$ for the *trans*−bent molecule. The conventional way to refer to the *trans*−bending mode is to designate it as mode V. For example, the transition $m\nu_3\tilde{A}, K = w \leftarrow n\nu_4\tilde{X}, l = z$ is described by the symbol $V_n^m K_z^w$. K is the quantum number of the projection of the total angular momentum onto the internuclear axis (it is designated as l for the linear ground state $\tilde{X}$). In our experiments we excite in the vicinity of the $V_0^3K_0^1(\tilde{A}^1A_u \leftarrow \tilde{X}^1\Sigma_g^+)$ sub-band of acetylene, since this region has been shown to be extensively coupled to a background manifold of triplet states as will be discussed [35, 43, 28].

The acetylene molecule has played a key role in the development of modern electronic spectroscopy. This was due primarily to the pioneering research of Ingold and King [69, 79] and of Innes [70]. The idea that the shape of an excited state of a molecule might differ qualitatively from that of the ground state was a novel idea in the early days of modern electronic spectroscopy and was suggested by Mulliken [101] for the CS_2 molecule in 1941. The experimental demonstration [69, 79, 70] of the bent excited state of acetylene may be viewed as the first evidence of this general

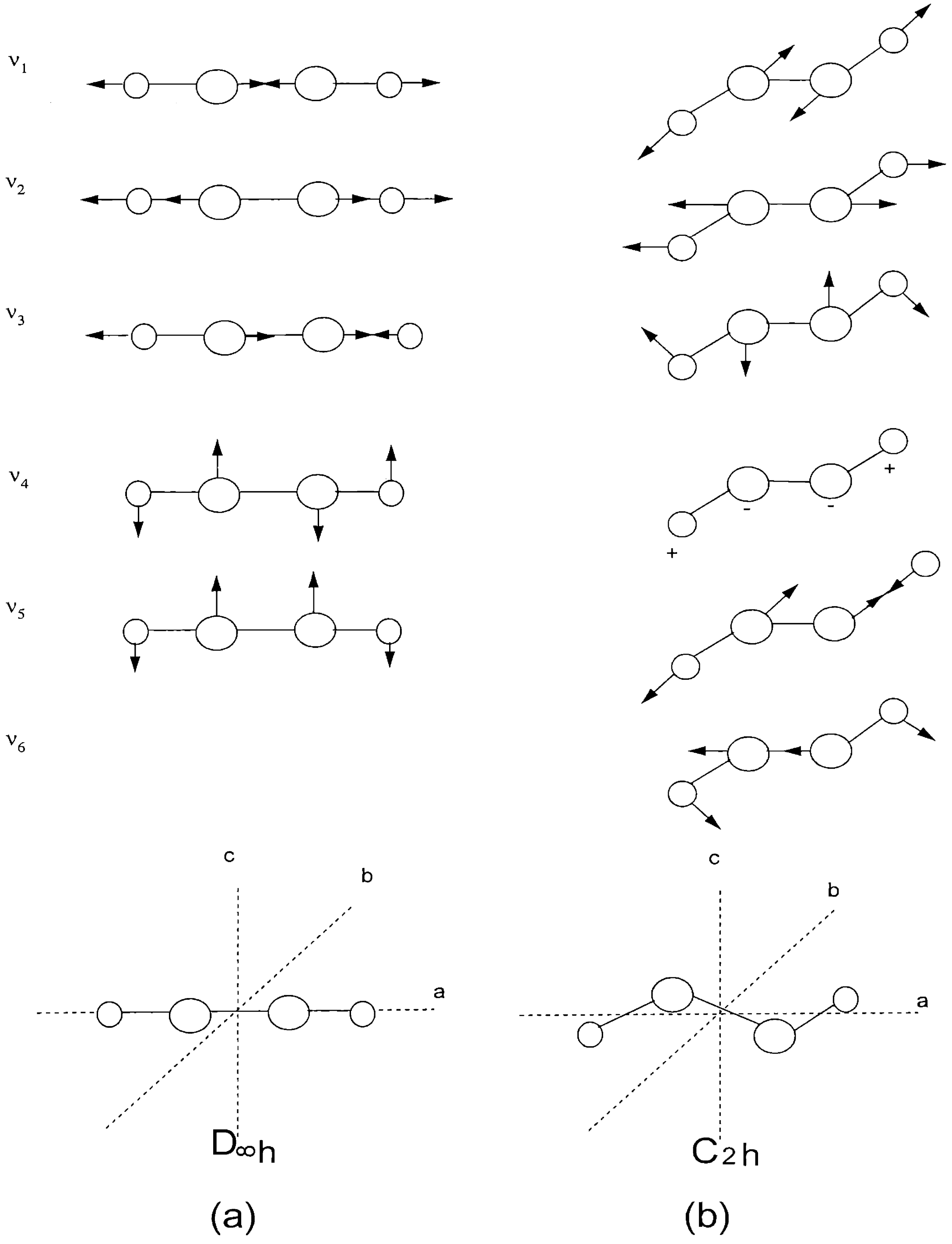

Figure 1-1: A schematic of the normal vibrational modes and the principal axes of acetylene in the linear (a) and *trans*–bent (b) geometries. The ν_4 and ν_5 modes in the linear geometry are doubly degenerate.

sort of behavior [147].

The experimental work done on acetylene that is relevant to the present project is summarized in chronological order:

1) 1952 - 1954: Ingold and King [69, 79] recorded an absorption spectrum of acetylene and, from the observed moments of inertia, determined that the excited singlet state has a *trans*-bent equilibrium structure (working independently, Innes also arrived at the same conclusion regarding the geometry of the excited singlet state of acetylene [70]). Ingold and King also reported an oscillator strength of 1×10^{-4} for the $\tilde{A}^1A_u \leftarrow \tilde{X}^1\Sigma_g^+$ electronic transition. This transition is $10^3 - 10^4$ times weaker than an ordinary allowed electric-dipole transition whose oscillator strength would be in the range 0.1-1. Ingold and King argued that the $\tilde{A}^1A_u \leftarrow \tilde{X}^1\Sigma_g^+$ transition had a small oscillator strength because it was "Franck-Condon forbidden" since the geometry change was very drastic (*trans*-bent ← linear).

2) 1979: Wendt, Hippler, and Hunziker recorded the near-infrared absorption spectrum of an electronic transition between triplet states ($T_2(cis) \leftarrow T_1(cis)$) [146]. The same spectrum was acquired at higher resolution by Kanamori and colleagues [137].

3) 1980: Lisy and Klemperer, in metastable deflection experiments, seemed to show that the lowest SEELEM detectable triplet state of acetylene must be linear or *trans*−bent since it lacks an electric dipole moment [91]. This result seemed at odds with the findings of Wetmore and Schaefer who presented in 1978 *ab initio* theoretical results which placed the *cis*−well on the first excited triplet surface of acetylene (T_1) lower than the *trans*−well [147]. The prediction of Wetmore and Schaefer had even been confirmed within a year by the observation of the ${}^3A_2 \leftarrow {}^3B_2$ spectrum by Hunziker and co-workers [146]. Lundberg and Field [93] brought a resolution to this situation in 1993. They explained that there is, in fact, no contradiction between the Lisy and Klemperer experiment [91] and either the Hunziker experiment [146] or the *ab initio* ordering of *cis* ${}^3B_2$ below *trans* ${}^3B_u$. Lundberg and Field argued that any *cis*−bent ${}^3B_2$ acetylene formed in the Lisy-Klemperer experiment was rendered SEELEM undetectable due to electronically allowed spin-orbit mixing with high vibrational levels of the ground electronic state. The *trans* ^3B_u state experiences much weaker spin-orbit mixing with the ground electronic state, since such mixing is only *vibronically* allowed.

4) 1982: The first laser-induced-fluorescence (LIF) study of the $\tilde{A}^1A_u$ state was conducted by Abramson and co-workers [3]. In this LIF study, which specifically targeted the $3\nu_3$ vibrational level, it was observed that the fluorescing states had long radiative lifetimes (2-5 μs) and large collisional quenching rates ($17 - 23 \times 10^6$ s^{-1} Torr^{-1}). These observations were the first indication that some of the levels in the $\tilde{A}$ state could be strongly coupled to a manifold of long-lived background states.

5) 1984: The collisional quenching rates of the LIF signal from the $\nu_3 = 0, 1, 2$ vibrational levels of the $\tilde{A}$ state were measured by Stephenson and co-workers and were found to increase as a function of *trans*-bending vibrational energy of excited acetylene [130]. This result was interpreted as being a consequence of increasingly stronger coupling of the $\tilde{A}$ state to non-fluorescing background states as a function of quanta of ν_3 excitation.

6) 1987 - 1991: Ochi and Tsuchiya recorded the LIF spectrum of the $\mathrm{V}_0^2\mathrm{K}_0^1$, $\mathrm{V}_0^3\mathrm{K}_0^1$, and $\mathrm{V}_0^4\mathrm{K}_0^1$ sub-bands of acetylene in a molecular beam with a resolution of 0.1 cm^{-1} [105]. They observed that the rotational lines of $\mathrm{V}_0^3\mathrm{K}_0^1$ are more fractionated than others. They also observed quantum beats in the fluorescence decay of some of the $\mathrm{V}_0^3\mathrm{K}_0^1$ rotational levels. The frequency and intensity of the beats changed in the presence of magnetic fields [104]. Based on these observations, Ochi and Tsuchiya put forth the idea that the $\tilde{A}$ $3\nu_3$ level of acetylene is strongly mixed with a background of triplet states. They also proposed that a rovibrational level of the T_3 state played a role in this coupling since a surface crossing between S_1 and T_3 had been calculated to occur in the energy region of the $\tilde{A}$ $3\nu_3$ level [90, 25, 28, 26]. Since T_3 does not have the vibrational state density at the energy of the $\tilde{A}$ $3\nu_3$ level to account for the observed degree of fractionation, it was hypothesized that T_3 played a role in mediating the coupling of the $\tilde{A}$ $3\nu_3$ level to the background of $\mathrm{T}_{1,2}$ states.

7) 1992 - 1995: Dai and co-workers studied the fluorescence decay of $\mathrm{C_2H_2(S_1)\cdot Ar}$ van der Waals complexes [19, 20, 74]. Different vibrational levels of the $\tilde{A}$-state were excited. It was observed that the fluorescence decay lifetime of the $C_2H_2(S_1)\cdot$Ar complex excited to the vibrationless level of the $\tilde{A}$- state was much shorter than that of the monomer excited to the same vibrationless level of the $\tilde{A}$-state. Dai and *et al.* attributed this to the enhancement of nonradiative decay processes upon complexation [1]. The same enhancement in the rate of intersystem crossing was not observed when there was some vibrational excitation in the complex ($\tilde{A}$-state) because the vibrational excitation caused the Ar to dissociate on a timescale of 10-50 ps (intersystem crossing rate is typically $\sim 10^{10}$ s^{-1}). The observation that presence of Ar enhances intersystem crossing in the vibrationless level of the $\tilde{A}$-state is an important one since metastable signal from this level has been very difficult to observe in our experiments.

8) 1994: Drabbels and co-workers recorded an 18 MHz-resolution LIF spectrum of the $V_0^3K_0^1$ and $V_0^4K_0^1$ sub-bands of acetylene [35]. These LIF spectra are, to this day, the most detailed look at the fractionated levels of the $V_0^3K_0^1$ and $V_0^4K_0^1$ sub-bands. The observed density of dark states in the vicinity of the S_1 $3\nu_3$ level based on this spectrum was 10/cm^{-1}, a number which is comparable with the expected density of T_1 states in the energy region of $\tilde{A}$ $3\nu_3$ and $\tilde{A}$ $4\nu_3$ levels. The fact that the LIF-detectable states also split into Zeeman components in the presence of magnetic fields confirmed the earlier predictions that these states have triplet character. Drabbels and colleagues used the Lawrance-Knight deconvolution algorithm [83] to calculate

---

[1] It is important to recognize a crucial difference between the Dai experiments and the experiments described in this thesis. Dai and co-workers excite a coherent superposition of eigenstates because, in the complex, the vibrational density of states and the strength of the spin-orbit coupling are both much larger. The same laser pulse would only excite a "quasi-eigenstate" in the monomer as is the case in the experiments described in this thesis. The decay of quasi-eigenstates excited in our experiments are purely radiative and this radiative decay rate is proportional to the fractional S_1 character. If the fractional S_1 character is small, then the fractional triplet character is large, especially if S_0 can be ignored. Therefore, long fluorescence decay in our experiments is associated with large triplet character, and hence, efficient intersystem crossing. However, in the case of Dai *et al.*, the decay is not purely radiative, it is the dephasing of a coherent superposition of states and happens fast. However, each eigenstate in the coherent superposition will radiatively decay very slowly because each has a small (diluted) fractional S_1 character. Since Dai measures the dephasing decay rate in his experiments, short decay times are associated with effective intersystem crossing.

the zero-order energies of the zero-order states (vibrational levels of the "dark" $T_{1,2,3}$ states) and the coupling strengths of these "dark" states to the bright singlet state.

9) 1991 - 1995: Dupré, Green, and Field conducted Zeeman Anticrossing (ZAC) studies of the $\tilde{A}\ ^1A_u(\nu_3 = 0 - 3)$ levels of acetylene [43]. In ZAC experiments, LIF is recorded as a function of magnetic field strength (the magnetic field was scanned between 0 - 8 T in the experiments of Dupré *et al.*). States that have triplet character tune in the presence of magnetic fields, and if one of these background triplet states tunes into degeneracy with an LIF-detectable state, then it mixes strongly with the LIF-detectable bright state and turns it into a longer-lived state (the lifetime change of the bright state is typically a factor of 2). Long-lived states are quenched by collisions before they can emit. Therefore, whenever a bright state mixes with a Zeeman-tuning background state, its fluorescence signal goes down and this is observed as a "dip" (*i.e.* anticrossing) in the ZAC spectra. The number of anticrossings in ZAC spectra can be correlated with density of background states. In ZAC experiments, it was again observed that the number of anticrossings increased dramatically as higher numbers of quanta of the $\tilde{A}$ ν_3 mode were excited. The quantum beat frequencies observed in the vicinity of anticrossings can yield local Landé factors (g_l) and triplet$\sim$singlet basis state coupling strengths. g_l factors ($g_l = 2$ for a free electron) can be regarded as approximate measures of the fractional triplet character in an eigenstate. Based on the observations from ZAC studies [40, 41, 42], Dupré and colleagues were able to propose an ordering of the interaction matrix elements between the acetylene electronic states according to their strengths: $\mathrm{S_0} \sim\mathrm{S_1} \ll \mathrm{S_0} \sim\mathrm{T} \ll \mathrm{S_1} \sim\mathrm{T} \ll \mathrm{T_1} \sim\mathrm{T_2}$.

10) 1997 - 1998: Suzuki and co-workers measured the lifetimes of the metastable states produced by intersystem crossing from the $\mathrm{V_0^3K_0^1}$ and $\mathrm{V_0^4K_0^1}$ levels of the $\tilde{A}$ state. They excited the acetylene molecules in a jet. The molecules travelled for 40 μs before colliding with a biacetyl-coated surface. Sensitized phosphorescence produced upon energy transfer from the incident metastable acetylene molecule to the biacetyl surface was measured. The experiments of Suzuki *et al.* were very much in the spirit of the experiments described in this thesis. Suzuki and colleagues determined the lifetimes of the metastable states to be 100 μs ($\mathrm{V_0^3K_0^1}$) and 80 μs ($\mathrm{V_0^4K_0^1}$). They also determined that the absolute fluorescence quantum yield from the $V_0^3K_0^1$ and $V_0^4K_0^1$ bands is around 0.13±0.1, indicating strong mixing of these levels with a background of non-fluorescing states.

11) 1999: Ahmed, Peterka, and Suits reported [4] for the first time an experimentally determined value for the excitation energy of the lowest triplet state T_1 ($\tilde{a}^3B_2$) of acetylene: 28900 cm^{-1} or 82.65 kcal mol^{-1}. Ahmed and co-workers used the velocity map imaging technique to study the photodissociation (243 nm) of the vinyl radical, C_2H_3. One of the minor products of the photodissociation process was identified as acetylene in the $\tilde{a}^3B_2$ state. The experimentally determined value of 28900 cm^{-1} for the excitation energy of the T_1 ($\tilde{a}^3B_2$) state does not agree well with recent *ab initio* calculations [110] which yield a value of 30500 cm^{-1} for this excitation. Ahmed *et al.* have stated it is possible that the experimentally determined value underestimates the true value.

There have also been electron energy loss studies of the triplet states of acetylene which will be discussed in Chapter 8.

The highlights from the theoretical work done on acetylene include the predictions of the geometries and the excitation energies of the excited triplet states (T_1 and T_2) [141, 147, 111, 110] and descriptions of the features of the low-lying triplet potential energy surfaces [25, 28, 26] such as their crossing with the singlet state S_1.

One of the goals of the theoretical studies was to explain the anomalous sudden increase of detectable Zeeman anticrossings reported by Dupré *et al.* [43]. It has been proposed that S_1 might cross with T_1 and T_2 around their respective $cis-trans$ isomerization transition state and that interaction would be strongest if the transition state is linear. However, in previous theoretical studies, no linear transition state has been found on T_1 or T_2 [28], and the non-linear isomerization barrier on T_2 is predicted to lie 4400 cm^{-1} below the $\tilde{A}$ $3\nu_3$ level [111]. It is possible that a linear higher order saddle point on T_2/T_3 is responsible for the ZAC observations [28], however, a more likely explanation is the possibility that the interaction might come from the T_3 state. In fact, Cui, Morokuma, and Stanton [28] have reported a crossing between the S_1 and T_3 surfaces (45500 cm^{-1} or 5.64 eV), which is nearly coincident

Table 1.1: Optimized energies (relative to S_0) for the minima on the seam of crossing (MSX) between some of the excited states of acetylene at different geometries and spin-orbit coupling matrix elements (H_{SO}) at the MSX's [28].

Electronic states	MSX energy eV	MSX symmetry	H_{SO} cm^{-1}
S_1/T_1	5.94	C_2	1.6
S_1/T_3	5.73	C_{2h}	13.9
S_1/T_3	6.02	C_{2v}	12.5
S_1/T_3	5.64	C_2	13.7
T_2/T_3	5.45	C_2	–
T_3^*	5.32	C_2	–

(*Findings for the T_3 stationary point)

energetically with the onset of the anomalous ZAC effects (~5.64 eV). The absolute value of the spin-orbit coupling element for the $S_1 \sim T_3$ interaction was calculated to be 13.7 cm^{-1} [28]. Table 1.1 is a list of optimized energies for minima on the seam of crossing (MSX) between some of the excited states of acetylene theoretically determined by Cui *et al.*. The calculated spin-orbit coupling elements at the MSX's and the symmetries are also given.

1.3 Progress Made

During the course of this thesis work, a second-generation doubly differentially pumped molecular beam machine was constructed with certain features superior to the first-generation apparatus. The first-generation apparatus was a single vacuum chamber and is described in Kevin L. Cunningham's thesis [29]. The second-generation apparatus is described in **Chapter 2**.

Lower (by a factor of 50) operating pressures achieved in the second-generation apparatus and the presence of a skimmer that collimates the molecular jet made it possible to perform certain experiments that could not be carried out successfully in the first-generation apparatus. Two-point lifetime measurements on the SEELEM-detectable states of ^1A_u $3\nu_3$ and ^1A_u $4\nu_3$ levels of acetylene were done and the results were used to estimate the S_1 fractional bright state character of the SEELEM-detectable eigenstates. Being able to quantitate the S_1 fractional bright state character of the eigenstates is an important step in constructing a mechanistic picture of the intersystem crossing process that distributes the bright state character over a manifold of background states. These measurements are discussed in **Chapter 3**.

Preliminary results were obtained that provided insight into the mechanism of the SEELEM process in which metastable species are quenched upon impact with a surface. It has been shown that de-excitation of a mixed molecular state on a SEELEM surface can proceed through either of two pathways: the singlet-mediated pathway (dipole-dipole or long-range interaction) or the triplet-mediated pathway (exchange or short-range interaction). The efficiency of the triplet-mediated pathway is very sensitive to external conditions, such as the background pressure during detection or the condition of the SEELEM surface. Under high background pressures, the triplet-mediated pathway can become exceedingly inefficient. Distinguishing the singlet-mediated pathway from the triplet-mediated pathway and recognizing the different tolerances of these two channels for external factors such as background pressure, allowed us to explain some of the unexpected results that were obtained in the first-generation apparatus. These findings are described in **Chapter 4**.

Analytical tools were developed that can be used to understand the simultaneously acquired SEELEM and UV-LIF spectra and to extract underlying coupling mechanisms from the observed spectral features. A mechanistic picture of the intersystem crossing process that distributes the bright state character over a background of dark states should specifically include the details of how the bright state is coupled to the background of dark states. These statistical tools are presented in **Chapter 5**.

An unexpected application of the Lawrance-Knight spectral deconvolution procedure [83] has been uncovered. This application is based on the recognition of a pattern of patterns in LIF spectra (meta-pattern-recognition). Using this technique, it is possible to distinguish between two extreme coupling mechanisms from experimental UV-LIF spectra: *direct* coupling in which the bright state fractionates statistically over a manifold of dark states, and *doorway-mediated* coupling in which a special state mediates the coupling of the bright state to the background of dark states. This technique was applied to an 18 MHz resolution UV-LIF spectrum of the $S_1(\nu_3 = 3) \leftarrow S_0(\nu_4 = 0)$ transition of acetylene recorded by Drabbels *et al.* [35]. It was shown that the bright state $\sim$ dark state coupling that gives rise to the spectral fractionation patterns in the UV-LIF spectrum is *doorway-mediated* and the crossing between the doorway state and the bright state occurs approximately at $J = 3$. An estimate for the rotational constant of the doorway state (which is suspected to be a rovibrational level of the T_3 surface [28]) has also been calculated as 1.06 cm^{-1} (to be contrasted with the B-value of S_1 $3\nu_3$ which is 1.031 cm^{-1}[35]). This unexpected application of the Lawrance-Knight technique is outlined in **Chapter 6**.

Further investigations of the IR-component of the fluorescence that results from exciting in the vicinity of the $S_1(\nu_3 = 0) \leftarrow S_0(\nu_4 = 0)$, $S_1(\nu_3 = 2) \leftarrow S_0(\nu_4 = 0)$, $S_1(\nu_3 = 3) \leftarrow S_0(\nu_4 = 0)$, and $S_1(\nu_3 = 4) \leftarrow S_0(\nu_4 = 0)$ transitions of acetylene have revealed that this IR signal is a result of a multiphoton excitation process and could be exploited in a two-color experiment to indirectly probe the intermediate states that belong to $S_1(\nu_3 = 3)$ and that are thought to be heavily mixed with background triplet states. A description of such a two-color scheme is presented in **Chapter 7**.

The questions that were formulated based on our findings so far and possible experiments that could be performed to address them are summarized in **Chapter 8**.

Chapter 2

Experimental

Most of the data described in this thesis have been recorded in a second-generation version of an apparatus described previously [68, 5]. The first-generation molecular beam machine, in which the SEELEM spectra displayed as Fig. 4-3 (Chapter 4) and Fig. 7-5 (Chapter 7) were acquired, consisted of a single vacuum chamber which contained three detectors: a photomultiplier tube (PMT, RCA), a Ge infrared detector (EI-A, Edinburgh Instruments, time response of 0.1 - 0.2 ms) and a SEELEM detector (designed by K. L. Cunningham, machined at the MIT Central Machine shop, brass unit with dimensions approximately 30 cm by 10 cm) [29]. The operating pressure in this chamber was $2 * 10^{-5}$ Torr. The current apparatus is a doubly-differentially pumped vacuum chamber, where the operating pressure in the "detector" compartment that houses the SEELEM detector is $4 * 10^{-7}$ Torr.

Although the pioneering experiments were done in the first-generation apparatus, the background pressure in this chamber soon became a limitation. The high background pressure especially hindered experiments which involved vacuum deposition of Cs on the detector surface to be able to acquire SEELEM spectra on this low work-function metal (Chapter 4). The fact that the molecular beam was a freely-expanding jet and was uncollimated in the first-generation apparatus, also complicated lifetime measurements as explained in Chapter 3. It was necessary to improve the background pressure to be able collect data not corrupted by the effects of crude vacuum conditions ($2 * 10^{-5}$ Torr).

2.1 Apparatus

The first-generation apparatus was composed of a stainless steel six-way cross and a three-way cross (MDC Vacuum Products). The total volume was approximately 12652 cm^3. This chamber was pumped by a diffusion pump (Varian VHS-6, pumping speed of 940 l/s for He with a cryotrap) which was interfaced to the chamber through a liquid nitrogen baffle and a manual gate valve. The foreline of the VHS-6 was pumped on by a mechanical pump (Welch, 1.1 hp, Model 1374, 650 l/m). A detailed description of this chamber can be found in [29].

The second generation apparatus is composed of a long stainless steel tube (36 cm long, 15 cm diameter) (Kurt J. Lesker, custom-made piece), a short stainless steel tube (16 cm long, 15 cm diameter)(MDC Vacuum Products piece, altered at the MIT Central Machine shop) and a stainless steel six-way cross (MDC Vacuum Products). A schematic drawing of the second-generation apparatus is provided in Fig. 2-1. The long stainless steel tube (6362 cm^3) constitutes the "source" chamber where the acetylene / He mixture is introduced into vacuum through a nozzle (Gentry-style R. M. Jordan Pulsed Valve, custom-made cylinder 42 cm long). The short tube and the six-way cross constitute the "detector" chamber (9260 cm^3) which houses the SEELEM detector. All the flanges are Conflat. Each chamber is pumped by a VHS-6 type diffusion pump (Varian and NRC). The forelines of the diffusion pumps are kept at 5 - 10 mTorr and are pumped on by two mechanical pumps (Welch 1374, 1.1 hp, 650 l/m). The detector chamber is interfaced to the diffusion pump through a manual gate valve and a liquid nitrogen baffle (the pumping speed of the diffusion pump through a cryotrap is 940 l/s for He). The source chamber is not equipped with a liquid nitrogen or a water baffle (the pumping speed of the diffusion pump with no traps is 3000 l/s for He). The diffusion pump which pumps the source chamber has an extended cap (*i.e.* "Mexican hat", Varian diffusion pump accessory) which is in thermal contact with the cooled outer wall of the diffusion pump, and hence, is expected to minimize the escape of diffusion pump oil into the source chamber.

The diffusion pump oil that is used is Santovac 5 (Varian), which is a polyphenylether

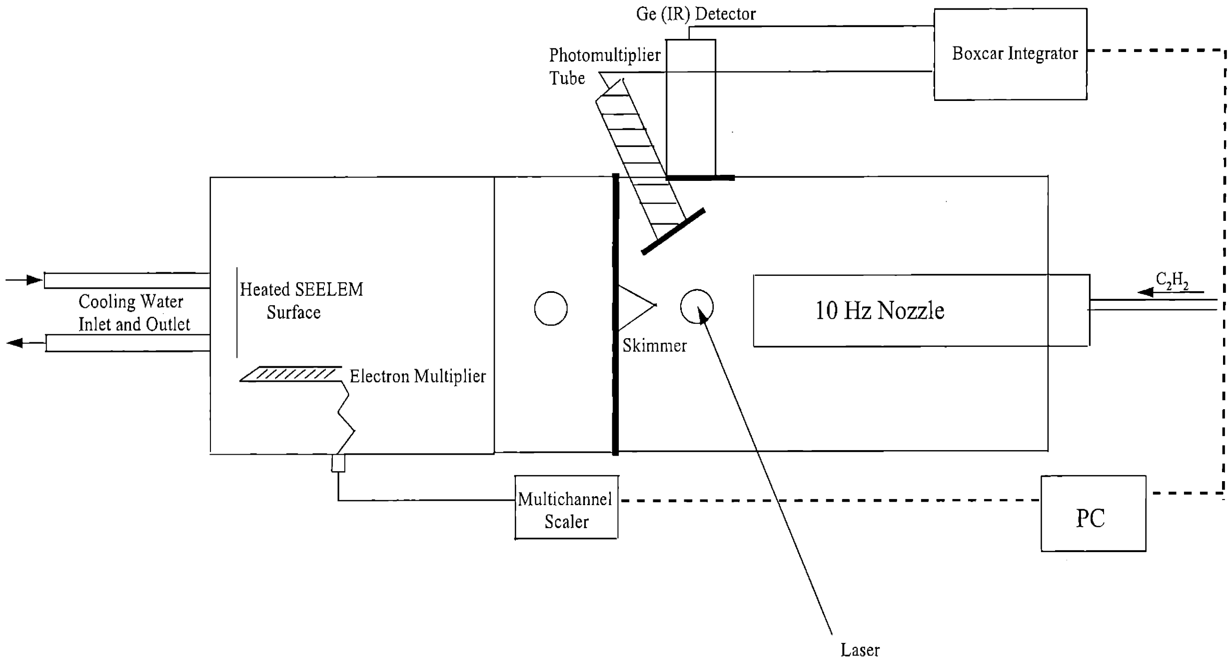

Figure 2-1: A schematic of the second-generation apparatus.

based oil with a very low vapor pressure, recommended for ultra-high vacuum applications. It was assumed that with Santovac 5, there would be no danger of oil contamination in the source chamber, therefore, an extended cap was used to trap oil vapor instead of a more drastic measure such as a baffle. It is known that baffles cut down on the pumping speed of the diffusion pump. However, we have had problems with oil getting into the chamber and coating the walls as well as the collection optics which reside inside the chamber. It is not clear if this is diffusion pump oil or mechanical pump oil migrating along the 9 m long PVC plumbing and finding its way into the chamber through the foreline outlet. Attempts to identify the oil contaminant by gas chromatography proved fruitless since diffusion and mechanical pump oils turn out to be too heavy to be effectively volatilized at the operating temperatures accessible at the MIT gas chromatography facility. Therefore, an Al foil was placed inside the source chamber to provide a cool surface to trap the oil vapor. This decreased the oil contamination plaguing the source chamber. However, a more permanent and effective modification would be to incorporate a water baffle.

We have never had problems with oil contamination in the detector chamber. In addition to the presence of the baffle, the PVC tubing which connects the foreline of the detector chamber diffusion pump to the mechanical pump is equipped with molecular sieves to guard against back-flow of mechanical pump oil.

The detector chamber is equipped with a relay box which monitors the level of the liquid nitrogen in the baffle, the foreline pressure of the diffusion pump, and the water flow rate to the diffusion pump. If any of these parameters falls below the specified threshold level, the relay box triggers an alarm and turns off the diffusion pump. The water flow is measured by a Proteus Industries Inc. flow meter (Model 0100B110) and the trap is filled continuously with liquid nitrogen through a Valcor Scientific valve controlled by a J.C. Controls LN_2 level sensor. The source chamber is not equipped with a relay box, but the water flow rate to the diffusion pump is continuously monitored (Proteus Industries flow meter).

The source chamber and the detector chamber are separated by a flange on which the skimmer is mounted. The skimmer flange is a design by Dr. Sergey Panov and serves as a valve which can be manually opened and closed to connect or isolate the source and the detector chambers. The skimmer is a 3-mm diameter electroformed skimmer (Precision Instruments).

The source chamber and the detector chamber are equipped with several ports (7 cm diameter, 7 cm long cylindrical tubes welded onto a conflat flange at one end, MDC Vacuum Products). The ports are used for entry / exit of the laser beam, mounting of collection optics for UV and IR fluorescence, mounting of ionization gauges (Varian 571 Bayard-Alpert ionization gauges, calibrated, controlled by a Varian senTorr unit and a Granville-Phillips series 271 gauge controller) and thermocouple gauges (Varian 531 thermocouple gauges controlled by a Varian 810 thermocouple gauge controller and a Hastings CVT-16 vacuum gauge controller). The ports were positioned so as to be able to carry out crossed-beam experiments as well, should there be any future interest. The molecules can be excited either in the source chamber or in the detector chamber. Excitation after the skimmer has the advantage of potentially reducing the

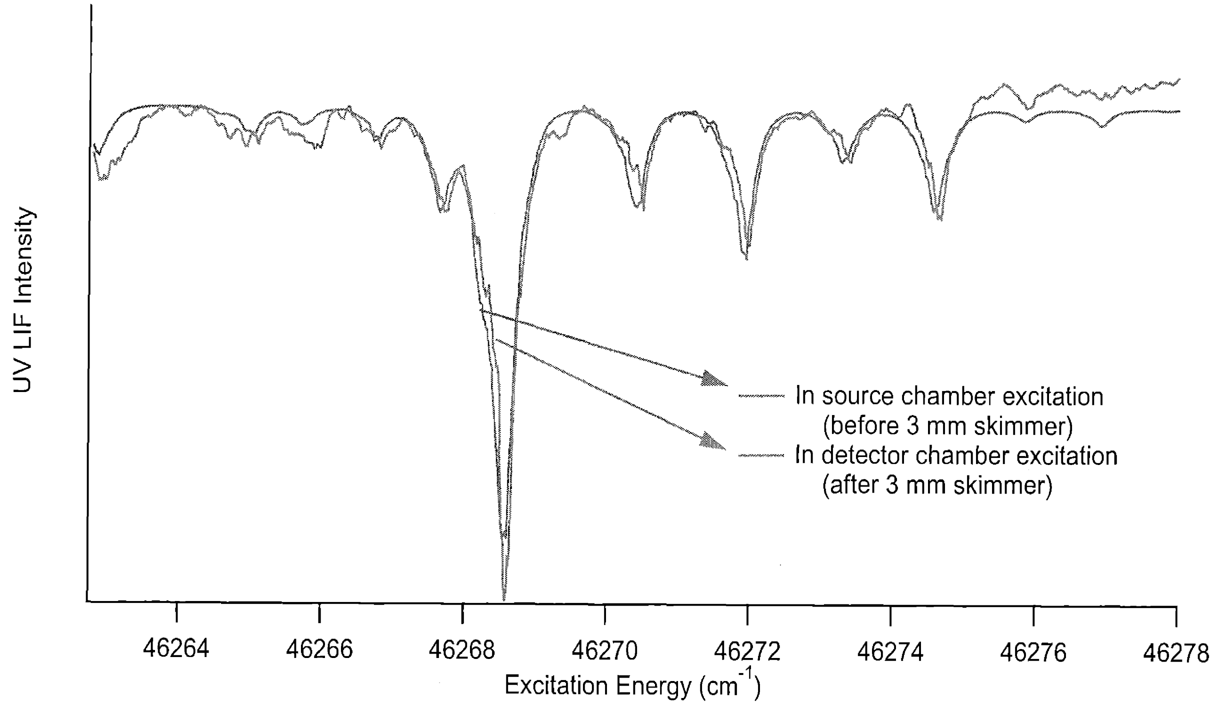

Figure 2-2: A linewidth comparison of the UV-LIF signal from the Q-branch of the $V_0^4K_0^1$ band of acetylene.

Doppler width in the Laser Induced Fluorescence spectra. However, the disadvantage is a reduction in the number of excited molecules. A comparison of UV-Laser Induced Fluorescence (UV-LIF) spectra recorded with excitation before and after the skimmer revealed that the improvement in Doppler width (Fig. 2-2) is not sufficient to justify the loss in signal ($\sim$ 70%) which especially hurts the SEELEM and IR-LIF channels. Therefore, molecules are always excited before the skimmer and the UV-LIF and IR-LIF signals are collected in the source chamber.

2.2 Experiment

A 1 atm mixture of C_2H_2 (BOC Gases, atomic absorption grade 2.6, purified by a freeze-thaw cycle using liquid nitrogen) seeded in He (BOC Gases) in a 1:5 ratio

[1] is expanded through a 0.5 mm diameter pulsed nozzle (Jordan Valve, open time 35 μs), operated at 10 Hz, into vacuum as a freely expanding jet. The unskimmed molecular jet is crossed 1.5 cm downstream from the nozzle by laser light linearly polarized parallel to the molecular beam propagation direction . A Nd:YAG pumped (5 ns pulse duration, 100 mJ pulse energy, 10 Hz repetition rate), frequency doubled (BBO Type I crystal) dye laser (5 ns pulse duration, tuned between 250 and 215 nm, 300 μJ pulse energy at the doubled frequency, 4 mJ pulse energy at the fundamental frequency, 3 mm diameter, 0.08 cm^{-1} spectral full width at half maximum (FWHM)), excites the $\tilde{A} \leftarrow \tilde{X} \;\; V_k^n K_m^l$ transition of $^{12}C_2H_2$ [2]. The background pressure in the "source" chamber with the nozzle operating is $2 * 10^{-5}$ Torr, as it was in the first-generation chamber.

A PMT (RCA, model 4501/V4, time response < 2.5 ns) and a Ge detector (Edinburgh Instruments, model EI-S, time response 8-10 μs) directly view the excitation region and collect the UV (200 to 300 nm) and IR (700 nm to 1.8 micron) components of the fluorescence, respectively. Both the UV and IR signals are integrated by a gated integrator and boxcar averagor (Stanford Systems, Model SR 250) and fed into a personal computer through a data-acquisition board (National Instruments, Version 4.6, 1994 Edition). Typical gates used for UV-fluorescence collection have a delay of 0.2 μs and a width of 2-4 μs. Typical gates used for IR-fluorescence collection have a delay of 0 μs and a width of 10-30 μs. Delaying the UV-gate with respect to the firing of the laser (which marks time 0 in the experiment) serves the purpose of avoiding the large scatter signal from the laser. The IR detector is blind to this signal (which is in the $\sim$ 220 nm wavelength region), therefore the IR-gate does not need to be delayed with respect to the firing of the laser. The program used to acquire the data is LabView (National Instruments) and was written by Kevin L. Cunningham and C. Gabe Morgan. The programs used to scan the laser remotely in the grating and etalon modes were written by Selen Altunata. The frequency calibration of the

---

[1] Slight variations from this ratio cause the molecular beam to be rotationally hotter or colder and can give rise to differences in the appearance of the spectra of identical wavelength regions.

[2] Here "V" stands for the *trans*-bending mode, and "K" stands for the projection of **J**, the total angular momentum, along the *a*-axis.

laser is done to ± 0.01 cm^{-1} accuracy from the absorption spectrum of $^{130}\text{Te}_2$ acquired simultaneously with the acetylene fluorescence / SEELEM spectra. The $^{130}\text{Te}_2$ cell is heated to 520^oC. Attenuation of the laser with the fundamental frequency as it goes through the $^{130}\text{Te}_2$ cell is monitored by a photodiode and an absorption spectrum is acquired for calibration [15].

The UV and IR fluorescence signals are collected by two pairs of 1 inch-diameter bi-convex quartz and BK7 lenses (JML Direct Optics), respectively. These lenses reside inside the source chamber. The first UV lens and the first IR lens are both located 1" above the molecular beam axis. The first UV lens has an effective focal length (EFL) of 38 mm and the first IR lens has an EFL of 42 mm. The second UV lens and the second IR lens are located above the first ones and both have an EFL of 75 mm. Each pair of lenses is stacked so as to collimate the fluorescence collected. The UV and IR fluorescence is then imaged onto the active surfaces of the PMT and Ge detectors (which are outside the vacuum chamber) through a quartz and a sapphire window, respectively. The focus of each lens pair is optimized on the bench using the output of a Hg lamp (253 nm) for the UV optics and the output of a Helium/Neon laser (632.8 nm) for the IR optics. UV-LIF spectra and IR-LIF spectra are recorded simultaneously with SEELEM spectra. 1.5 cm downstream from the excitation region, the molecular beam, now containing laser excited metastables, passes through a 3-mm diameter electroformed skimmer (Precision Instruments) into the detector chamber where the operating pressure is $4 * 10^{-7}$ Torr. The excited molecules travel another 5 - 25 cm before colliding with the SEELEM detector surface. The SEELEM detector comprises a metal surface and an electron multiplier. On impact with the SEELEM detector surface, the metastable molecules are deexcited and the deexcitation energy causes electrons to be ejected from the metal surface. These electrons are captured by the electron multiplier (ETP, SGE Instruments, Model AF831H, 10^5 gain), sent through an amplifier (x200) and a discriminator unit (EG&G, Ortec 9302) and counted by a multichannel scaler (Oxford Instruments, MCS-II). Both SEELEM and time-of-flight (TOF) spectra can be collected.

The distance from the excitation region to the SEELEM surface is variable and permits measurement of the lifetimes of the metastable molecules. The measured lifetimes of the SEELEM detected eigenstates excited in the vicinity of the $\tilde{A} \leftarrow \tilde{X}$ $V_0^3 K_0^1$ band cluster around 60 μs, with the states associated with the R(1) rotational transition (J'=2 $\leftarrow$ J"=1) exhibiting the longest lifetimes, at $\sim$ 100μs (Chapter 3). Lifetime measurements are more accurately performed in the second-generation apparatus because the collimation of the molecular beam, brought about by the presence of the skimmer, ensures that all the photoexcited molecules in the supersonic molecular beam are captured on the active surface of the SEELEM detector (a circle of radius 1 cm situated between 15 - 25 cm from the nozzle, which corresponds to a 0.014 - 0.005 sr solid angle relative to the nozzle orifice) (Chapter 3).

Another important variable in the experiment is the metal used as the SEELEM detector surface. The use of different metals as the SEELEM detector surface (Au, Ag, Cu, Y, Sm, Cs) permits variation of the relative sensitivities to $T_{1,2}$ vs. T_3 excited triplet electronic states because the conversion of the electronic energy of an electronically excited metastable state to an ejected electron occurs only if the vertical electronic de-excitation energy exceeds the work function of the SEELEM metal (Eq. (2.1)). Neither excess vibrational excitation nor translational energy contributes significantly to SEELEM detectivity [121, 91, 53].

$$\begin{aligned} E_k &= E_{T_i} - \Phi_{metal} \\ E_k &> 0 \text{ if } E_{T_i} > \Phi_{metal} \end{aligned} \tag{2.1}$$

where E_k is the kinetic energy of an ejected electron, E_{T_i} is the vertical electronic energy of the state T_i, and Φ_{metal} is the work function of the metal.

2.3 Highlights from Data Acquired in the Second-Generation Apparatus

The key feature of the experimental setup is its ability to detect simultaneously, in two separate detection channels (UV-LIF and SEELEM), signals due to both fast-decaying (lifetime $< 5\mu$s) and long-lived eigenstates (lifetime $> 100\mu$s).

Figure 2-3 shows rotationally resolved UV-LIF and SEELEM spectra acquired in the second-generation apparatus [3]. The SEELEM metal used was Au ($\Phi = 5.1$ eV). Of the acetylene electronic potential energy surfaces in the region of the excitation energy, S_1 and T_3 are the only ones which lie at vertical energies larger than the work function of Au [24, 137]. Therefore, the SEELEM detector in this particular case was sensitive exclusively to the T_3 and S_1 characters of the metastable eigenstates reaching its surface. The UV-LIF spectrum samples molecular eigenstates that have large (> 0.014) S_1 fractional character so that they can fluoresce before flying out of the viewing region of the PMT. The corresponding SEELEM spectrum is much more dense and complicated than the UV-LIF spectrum because it results from a *complementary* set of molecular eigenstates that have small (< 0.014) S_1 fractional character and, hence, can survive the flight time from the point of laser excitation to the SEELEM detector surface without losing their electronic excitation energy via spontaneous fluorescence. The UV-LIF spectrum has slightly lower resolution due to the Doppler broadening incurred through the uncollimated geometrical expansion of the acetylene molecules. It should be recalled at this point that the UV-LIF signal is recorded before the skimmer and the SEELEM signal is collected after the skimmer.

Figures 2-4 and 2-5 show a series of SEELEM spectra in order of increasing excitation energy of the $V_0^2K_0^1$, $V_1^3K_1^0$, $V_0^3K_0^1$ and $V_0^4K_0^1$ sub-bands of acetylene. The series of spectra reveal how indeed $3\nu_3(V_0^3K_0^1)$ is a special level in terms of its coupling to the background of dark triplet states. The SEELEM spectrum of the $V_0^3K_0^1$ sub-band exhibits the highest signal level and the fractionation pattern is indicative of extensive coupling to a background of dark states. In contrast, the SEELEM spectrum of $2\nu_3(V_0^2K_0^1)$ appears free of fractionation and is an exact replica of the UV-LIF spectrum. Lack of fractionation suggests minimal coupling to the background of dark states.

The $4\nu_3$ level exhibits a weaker SEELEM signal level than $3\nu_3$. A lifetime study was carried out both on $4\nu_3$ and $3\nu_3$ states. The findings for the $3\nu_3$ states are reported

---

[3] The mathematical descriptions of the SEELEM and UV-LIF signals will be presented in Chapter 5.

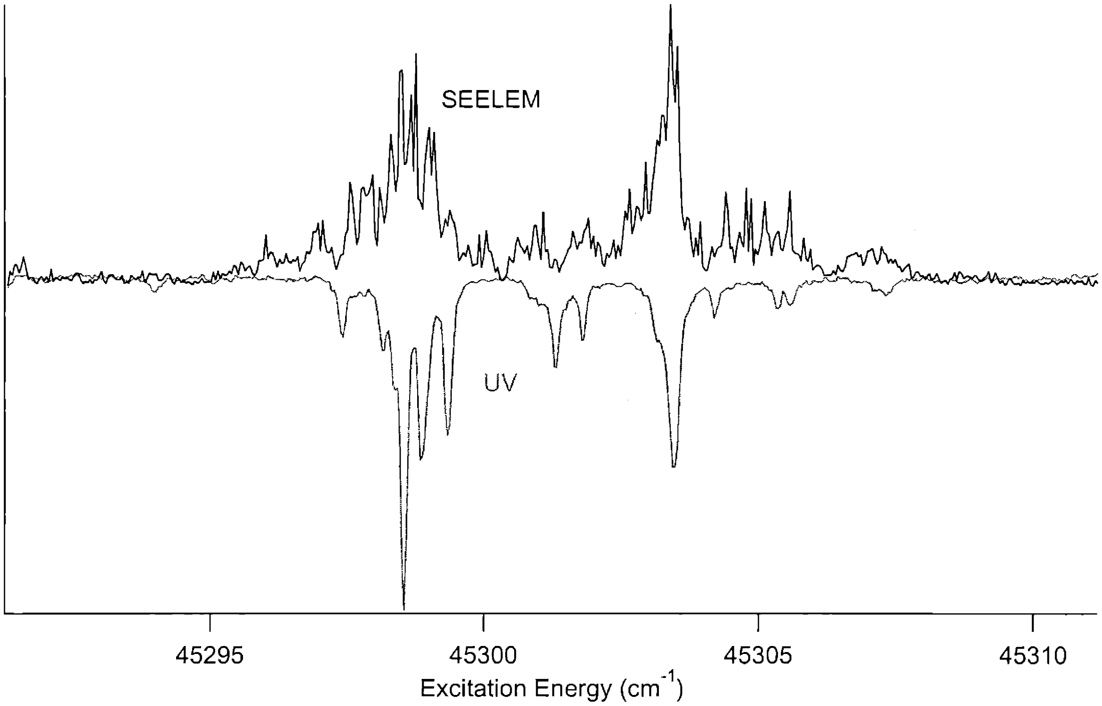

Figure 2-3: Simultaneously acquired SEELEM and UV-LIF spectra of the S_1 $V_0^3 K_0^1$ sub-band of acetylene. The spectra exhibit rotational structure.

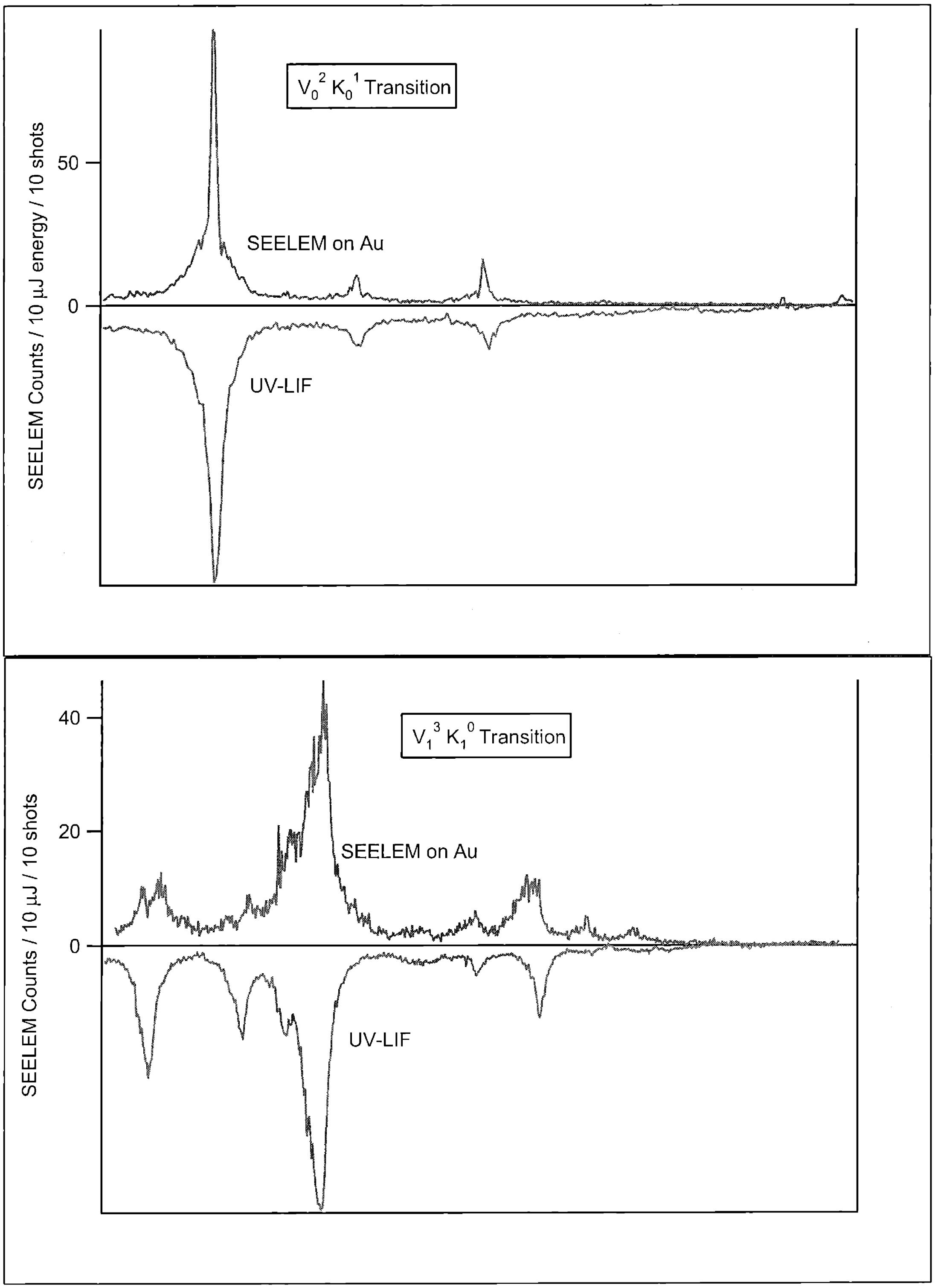

Figure 2-4: SEELEM and UV-LIF spectra of S_1 $V_0^2K_0^1$ and $V_1^3K_1^0$ bands, acquired under identical experimental conditions.

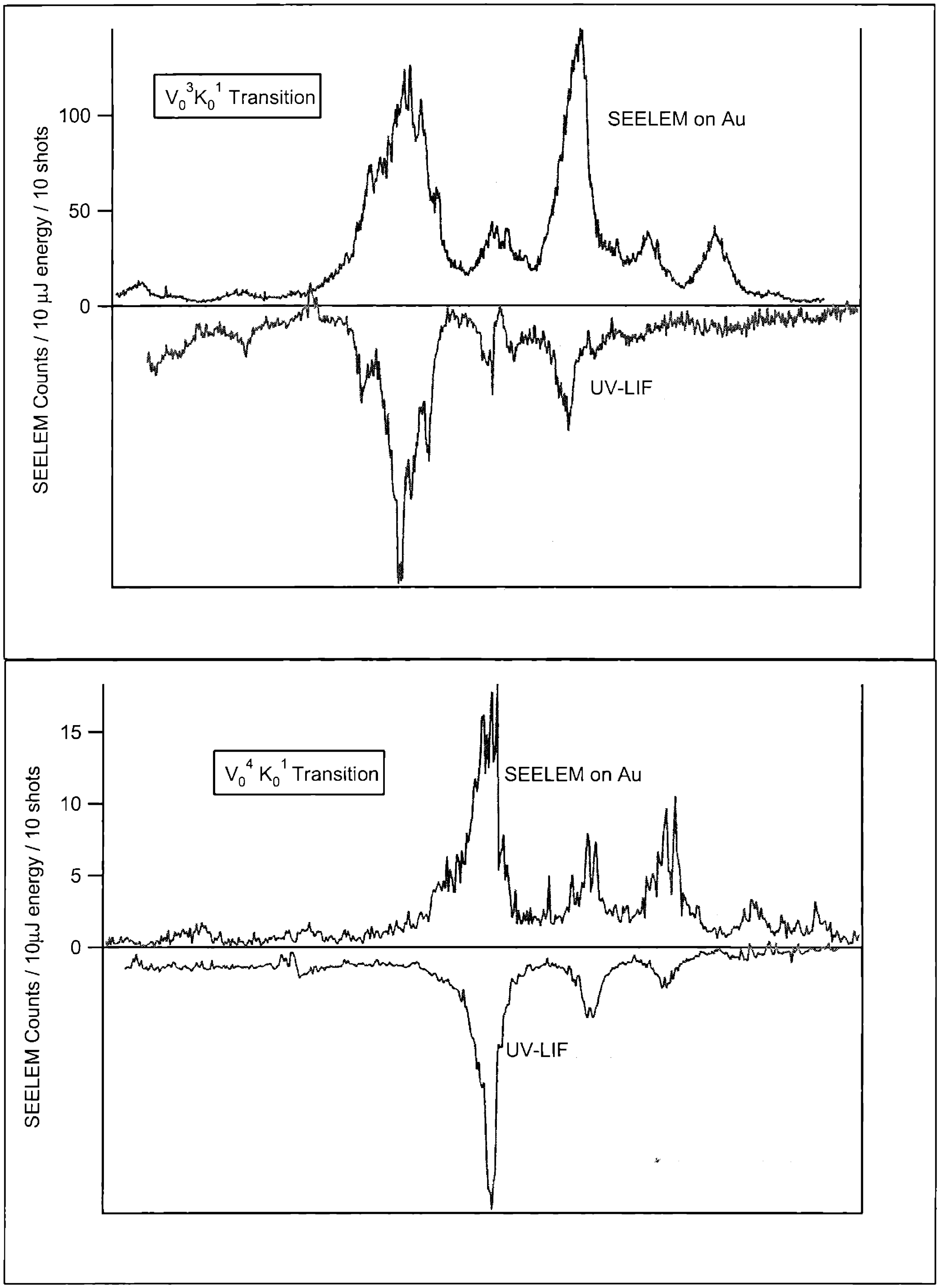

Figure 2-5: SEELEM and UV-LIF spectra of S_1 $V_0^3K_0^1$ and $V_0^4K_0^1$ bands, acquired under identical experimental conditions.

in Chapter 3. The lifetimes of the UV-LIF active states of $4\nu_3$ were in the range of 0.29 - 0.58 μs. This is to be contrasted with the measured lifetimes of around 1.1 μs of the UV-LIF active states of $3\nu_3$ (Chapter 3). The much shorter radiative lifetimes of $4\nu_3$ states imply that the coupling of this level to the background of dark states is weaker compared to that of the $3\nu_3$ level.

Of the 20 SEELEM active features sampled for lifetime measurements in the $4\nu_3$ level, only 7 states were found to be sufficiently long-lived to yield accurate measurements. Their lifetimes were around 100 μs. These states are excited via the Q-branch of the $4\nu_3$ spectrum, where the strongest UV-LIF peaks also appear. The SEELEM lifetime measurements were performed by recording two time-of-flight spectra at two different positions of the SEELEM detector surface relative to the laser excitation region, as explained in Chapter 3.

Alec Wodtke and colleagues, who collected the preliminary SEELEM spectra of the different vibrational levels of acetylene at the University of California at Santa Barbara, have actually calculated the integrated ratios of SEELEM to UV-LIF signals for a number of acetylene $\tilde{A} \leftarrow \tilde{X}$ vibronic bands [68]. The ratios were scaled to set $V_0^3 K_0^1$ equal to 1 and are tabulated in Table 2.1 in order of increasing energy of the final state.

2_n^k denotes the C-C stretching mode and V_n^k, as mentioned previously, denotes the *trans*-bending mode.

In addition to SEELEM and UV-LIF spectra, we can also collect IR-LIF spectra of the excited eigenstates. The IR signal has a non-linear dependence on laser intensity and is attributed to the electronically excited C_2H photofragments created subsequent to a multiphoton absorption event (Chapter 7). Figure 2-6 shows UV-LIF and IR-LIF spectra of the $3\nu_3$ band of acetylene acquired simultaneously.

The temporal profile of the IR emission is governed by the time response of the Ge detector ($\tau \approx 8 - 10\mu$s). In contrast, the PMT has a very short time response ($\approx$ 2 ns), therefore the temporal profile of the UV emission can be directly related to the lifetime of the emitting states. The lifetimes of the UV-active states were thus determined from the fluorescence decay curves (Chapter 3). Because the time

Table 2.1: Ratios of SEELEM to UV-LIF signal intensities for several acetylene $\tilde{A} \leftarrow \tilde{X}$ vibronic bands [68].

Vibronic band	Energy of final state (cm^{-1})	SEELEM:UV-LIF
$V_0^2K_0^1$	44350	0.12 ± 0.02
$2_0^1V_0^1K_0^1$	44650	<0.06
$2_0^1V_1^2K_1^2$	45120	0.2 ± 0.05
$V_1^3K_1^0$	45300	0.45 ± 0.1
$V_0^3K_0^1$	44300	1
$V_1^3K_1^2$	44362	0.9 ± 0.2
$2_0^1V_1^2K_1^0$	45692	0.4 ± 0.1
$V_0^4K_0^1$	46300	0.09 ± 0.02

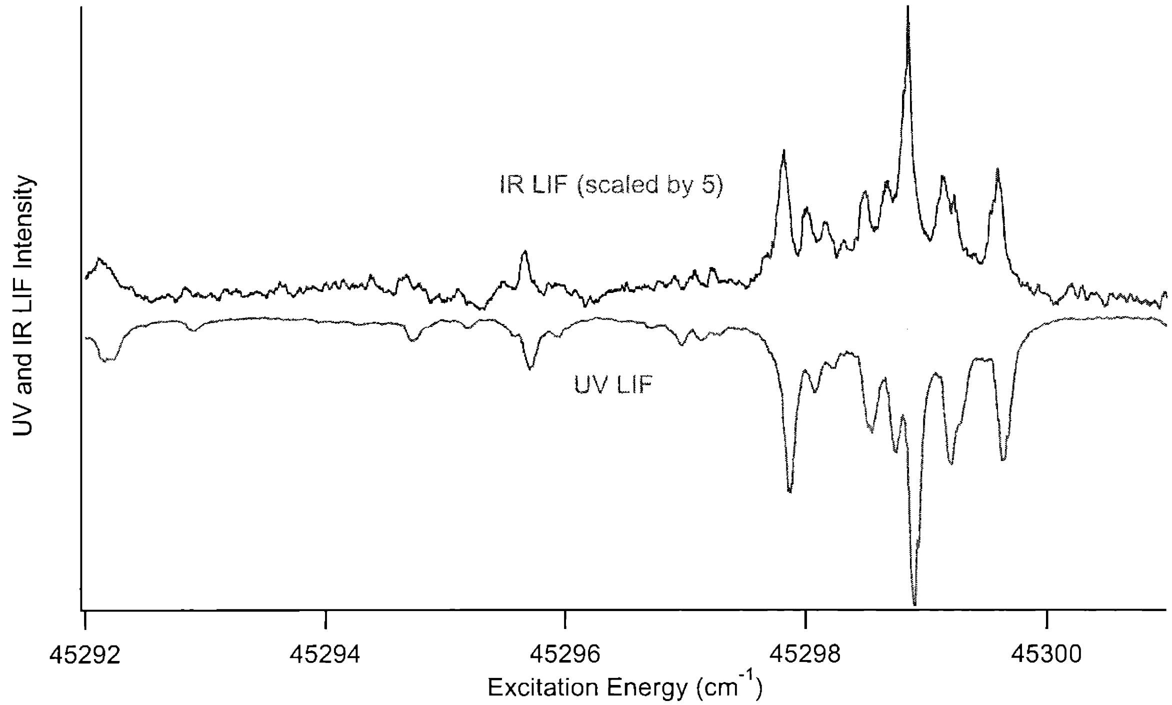

Figure 2-6: Simultaneously acquired UV-LIF and IR-LIF spectra of the Q-branch region of the S_1 $V_0^3K_0^1$ sub-band of acetylene.

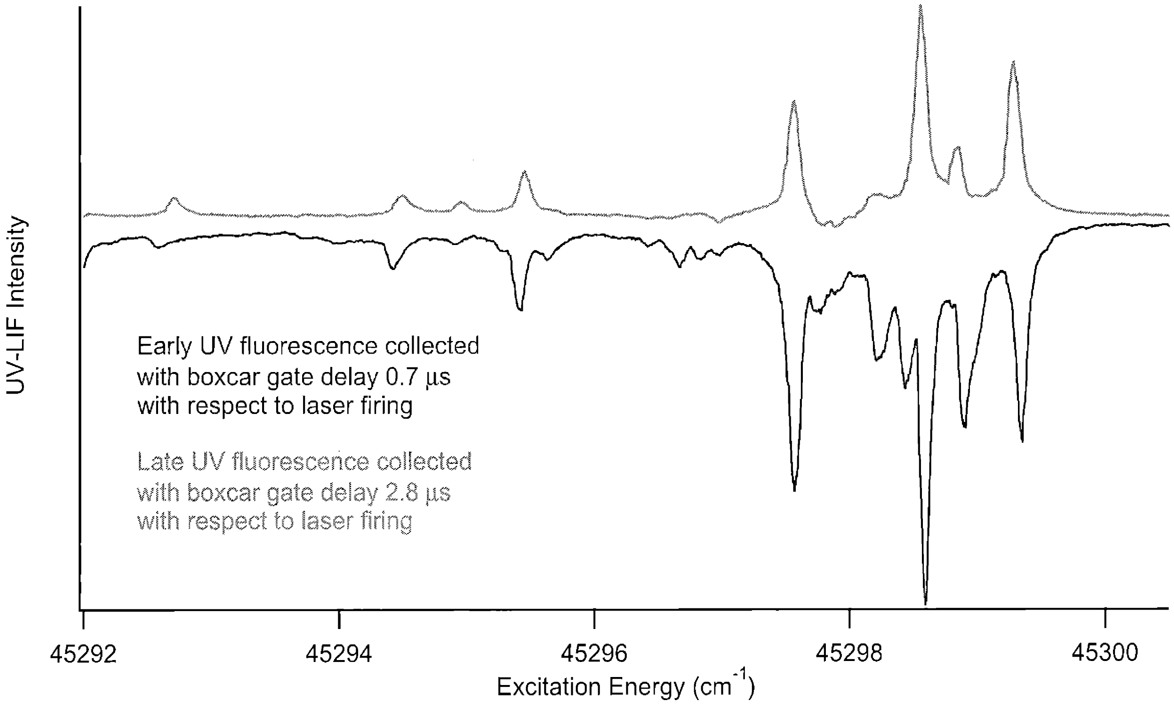

Figure 2-7: Early and late emitting UV-LIF active states excited in the Q-branch region of S_1 $V_0^3K_0^1$ sub-band of acetylene. The two spectra were acquired by changing the delay between the laser excitation pulse and the start of boxcar integration of UV-LIF signal. The delay of the early gate was 0.7 μs and its width was 1.1 μs. The delay of the late gate was 2.8 μs and its width was 2 μs.

response of the PMT is not a limiting factor, it is possible to collect the UV-LIF spectra of early-emitting (*i.e.* short-lived) and late-emitting (*i.e.* long-lived) states separately by adjusting the delay of the gate over which the fluorescence signal is integrated with respect to the firing of the laser (which marks $t = 0$ in the experiment). The spectra of the early-emitting UV-LIF states and the late-emitting UV-LIF states of $3\nu_3$ are compared in Fig. 2-7.

In this chapter I have presented some of the highlights from the data set acquired in the second-generation apparatus. The interpretation and the significance of the data will be presented in the following chapters.

Chapter 3

Lifetimes of Metastable Molecular Eigenstates

The lifetimes of the metastable molecular eigenstates that we detect in our experiments on acetylene can be related to their fractional bright state character. The radiative lifetime of a pure singlet (*i.e.* bright) state is about 270 ns whereas that of a pure triplet (*i.e.* dark) state is on the order of tens of ms [68]. Therefore, the radiative decay of an excited eigenstate will be largely governed by its fractional bright state character. Consequently, measuerement of the lifetimes of the SEELEM detectable eigenstates can provide valuable information about their electronic state composition and this information can in turn provide insight into the intersystem crossing process that distributes the bright state character over a manifold of several types of dark states. Deciphering the electronic state composition of the SEELEM detectable eigenstates would also make possible a detailed characterization of the SEELEM process and allow determination of parameters such as the relative SEELEM detectivities of the triplet and singlet characters of mixed states. The triplet and singlet characters of a mixed state are expected to have different SEELEM detectivities as explained in Chapter 4.

3.1 Earlier Work on Lifetime Measurements of S_1 $3\nu_3$ States of Acetylene

There have been several previous attempts to determine the lifetimes of the eigenstates created upon excitation in the vicinity of the S_1 $3\nu_3$ vibrational level of acetylene. The techniques used in these lifetimes measurements and their results are summarized below.

3.1.1 First SEELEM Experiments on Acetylene at UCSB

Wodtke *et al.* have determined the lifetimes of the $3\nu_3$ states of acetylene by recording the SEELEM intensity of these states in two different carrier gases: H_2 and He [68]. The velocity of the molecular beam is determined by the carrier gas. Therefore, the metastable molecules arrive at the SEELEM detector surface at different times when they are seeded in different carrier gases. The difference in the signal levels at the two arrival times is directly related to the decay of the excitation, and hence, the lifetime of the SEELEM detectable molecules.

One parameter that changes when the carrier gas is changed is the density of molecules of interest in the excitation region. The distribution of molecules of interest in a molecular beam is greatly affected by the type of the carrier gas. A well-known effect is the "mass-focussing effect" by which the heavier species is concentrated along the molecular beam axis in a supersonic expansion of two different species [73, 34]. In order to correct for the expected difference in the density of molecules of interest in the excitation region for the different carrier gases, the Wodtke team normalized their SEELEM intensities by the UV-LIF intensities.

Another parameter that can potentially be of concern is the velocity distribution perpendicular to the molecular beam. If this perpendicular velocity distribution is dependent on the carrier gas, then the angular expansion of the molecular beam will be different and the solid angle of the molecular beam intercepted by the SEELEM detector may change from one carrier gas to another, confounding the lifetime measurement. However, a set of experiments performed in different carrier gases where 2-dimensional images of the spatial distribution of excited CO molecules impacting a SEELEM surface were collected, revealed that the velocity distribution perpendicular to the molecular beam axis is in fact independent of the carrier gas [73]. The interpretation of this experimental observation was that, since the collisions between the carrier molecules and the molecule of interest occur predominantly along the molecular beam axis, these collisions are not capable of impacting the velocity distribution of the molecule of interest perpendicular to the molecular beam axis.

The average lifetime of the metastable states for the S_1 $3\nu_3$ level reported by Wodtke *et al.* is $80 \pm 30 \mu s$. The experimental error is large due to the fact that only two data points were used to fit an exponential decay curve (SEELEM signal in H_2 as the carrier gas and SEELEM signal in He as the carrier gas). This measurement is actually in reasonable agreement with the most recent lifetime measurements performed on the same vibrational level with our second-generation apparatus, as will be described in detail in Section 3.2.

3.1.2 Sensitized Phosphorescence Experiments

Suzuki *et al.* have also attempted to measure the lifetimes of the S_1 $3\nu_3$ states of acetylene using a different detection technique than SEELEM [133, 112]. In their experiments, excited molecules impacted a surface coated with biacetyl. The excited molecules transferred their excitation energy to the biacetyl surface, which then phosphoresced. The phosphorescence signal was collected with a photomultiplier tube. Suzuki and co-workers also used expansion in two different carrier gases, He and Ar, to determine the lifetimes of the S_1 $3\nu_3$ metastable states. Their finding for the lifetime was $100 \pm 50 \mu s$, which is in reasonable agreement with Wodtke *et al.*'s result.

3.1.3 SEELEM Experiments Performed in the First-Generation Apparatus at MIT

The first set of lifetime measurements performed on the S_1 $3\nu_3$ states of acetylene in the first-generation apparatus yielded conflicting results. The first attempt involved co-expanding the acetylene molecules with another gas, NO, whose excited a $^4\Pi$ state has a calculated lifetime of 100 ms [86]. Since the flight time was only $\sim$ 65 μs, metastable NO molecules did not undergo significant decay *en route* to the SEELEM detector. C_2H_2 and NO were excited in two different experiments where only the laser frequency was changed. Other than the excitation wavelength, all other parameters were kept constant between the two experiments. The two gases were seeded in He (6% NO and 33% C_2H_2). Time-of-flight (TOF) spectra were acquired and compared to deduce the lifetime of the C_2H_2 states [29]. The assumption was that since the lifetime of NO states was much longer than the flight time, the velocity distribution of the metastable NO molecules would be free from any effects of decay and would be described by a Gaussian function:

$$P(t) = C\frac{1}{t^4}e^{\frac{-B}{t^2}}, \qquad (3.1)$$

where B is given by

$$B = \frac{mL^2}{2kT}, \qquad (3.2)$$

C is a normalization constant, m is the molecular mass, k is Boltzmann's constant, T is the temperature of the gas in the collision region, and L is the distance between the excitation region and the detector.

On the other hand, the TOF profile of metastable C_2H_2 molecules would be characterized by an exponential decay superimposed on the Gaussian distribution of the velocities:

$$P(t) = C\frac{1}{t^4}e^{\frac{-B}{t^2}}e^{\frac{-t}{\tau}} \qquad (3.3)$$

Therefore, it was thought that it would be possible to simulate the C_2H_2 TOF profile by convoluting an exponential decay function with the Gaussian profile of the NO profile. However, this calculation yielded a best fit line whose decay constant τ was

10 μs, implying that this was the lifetime of the metastable acetylene states in the co-expansion. This approach clearly *significantly* underestimated the lifetimes of the metastable acetylene states.

The are a number of reasons why the co-expansion approach outlined above could have failed: A simplifying assumption could have been made in the analysis of the data which might have led to the erroneous decay constant for metastable acetylene molecules. For example, the molecular mass of NO is 30 amu whereas that of C_2H_2 is 26 amu. Although small, this difference in the molecular masses of the two species should have been taken into account when the best fit decay line was being searched for. It is not accurate to assume that in the absence of any decay, the velocity distribution of C_2H_2 would be superimposable on that of NO because the two molecules have different masses. In fact, Fig. 3-1 shows that even for a small difference in molecular mass, the velocity distribution profiles could look quite different for two co-expanded species. Therefore, a simple calculation which merely involves the convolution of the Gaussian profile of the NO TOF with an exponential decay function to simulate a profile that best matches that of the C_2H_2 TOF, may actually yield incorrect results. The author of the current thesis was not involved in the calculation of the best fit line, the details of which are not explained in [29], so it is not clear if this was a source of error.

Another point that should be considered is that because NO is slightly heavier relative to the carrier gas He than C_2H_2, it may experience a slightly different mass focussing effect than C_2H_2. The mass focussing effect serves to concentrate the heavy species along the molecular beam axis and, therefore, compresses the TOF profile of that species. The effect of the carrier to molecule-of-interest mass ratio on the width of the velocity distribution is in fact illustrated by some of our TOF spectra collected in the second-generation apparatus (Fig. 3-2). However, if there were a significant difference in the degree of the mass-focussing effect experienced by NO and C_2H_2, this would have biased the decay constant calculation in the opposite sense: the decay constant for acetylene would have been overestimated since NO would have experienced a stronger mass-focussing effect and, hence, the "decay-free" TOF

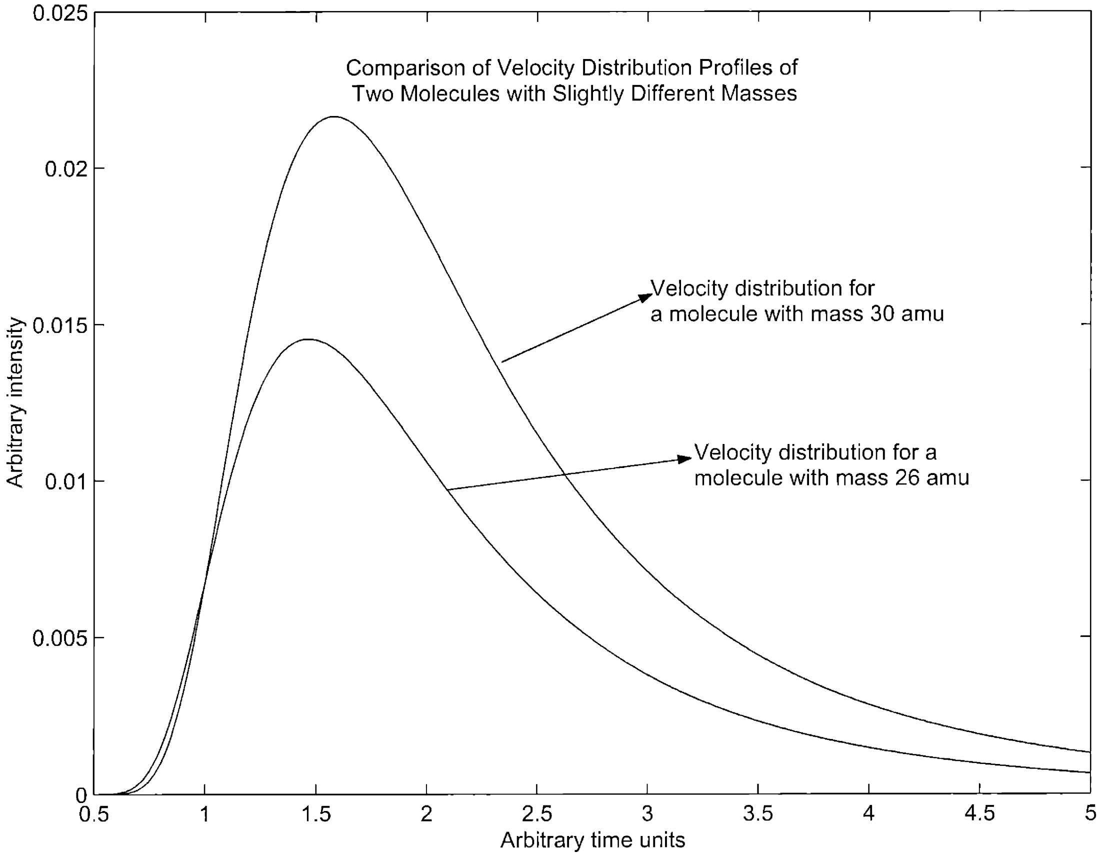

Figure 3-1: Simulated velocity distribution profiles for two molecules with similar masses (30 amu and 26 amu), assumed to be expanded under identical conditions. Although the difference in the molecular masses is small, the velocity distributions still look quite different. The integrated areas under the curves are different, which reflects the fact that different amounts of each species are being co-expanded in the hypothetical experiment.

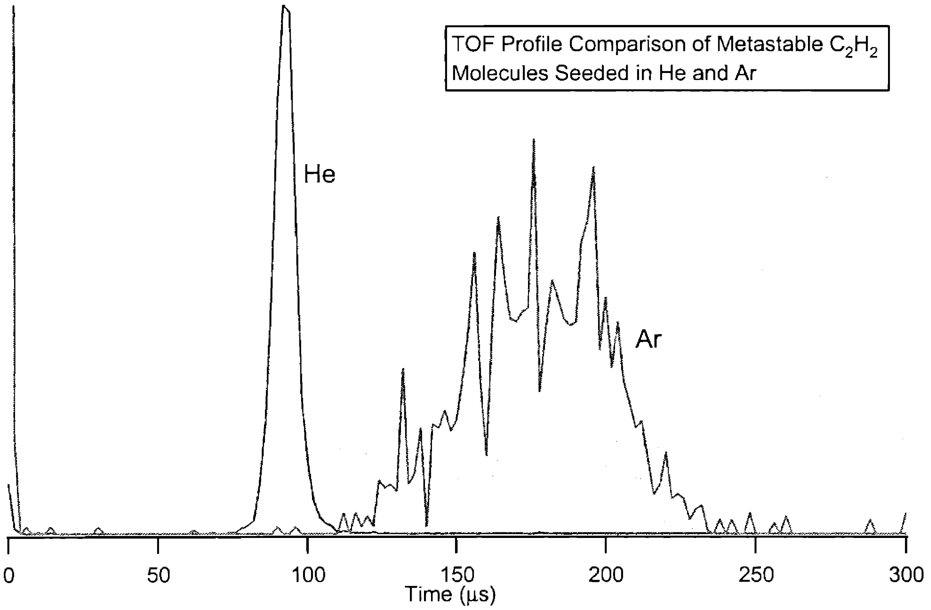

Figure 3-2: 18% C_2H_2 was expanded in a 1.5 atm mixture of either C_2H_2 / He or C_2H_2 / Ar. The TOF profiles show that, due to the mass focussing effect, the velocity distribution of metastable acetylene molecules is much tighter when acetylene is seeded in the lighter carrier gas, He.

extrapolated for C_2H_2 would have had a "tighter" profile (*i.e.* larger apparent B). In that case, it would have been necessary to convolute this "tighter" profile with an exponential function that had a "smaller" decay constant to simulate the experimental C_2H_2 velocity distribution. Since the decay constant obtained for acetylene is much larger than expected, the mass-focussing effect does not seem to be significant enough to be a source of error for this calculation.

A more fundamental factor which could have led to the erroneous result for the lifetimes of the metastable acetylene states is the possibility that NO and C_2H_2 have different SEELEM detectivities. Factors such as tendency of the molecule to absorb to the SEELEM surface, SEELEM de-excitation route followed, *etc.* all affect SEELEM efficiency and are specific to the molecular system being detected. A variant of the co-expansion method was successfully employed by Mason and Newell successfully [95], but they actually detected two different excited states with two different lifetimes of the *same* molecule ($N_2(a^1\Pi_g)$ and $N_2(A^3\Sigma_u^+)$). The co-expansion approach becomes tricky when two different species are used.

The second-set of experiments, which were targeted at measuring the lifetimes of the metastable acetylene molecules performed in the first-generation apparatus, involved comparison of SEELEM spectra with different flight times. The excitation region to SEELEM detector distance was manually changed by moving the SEELEM detector to achieve different flight times. The difference in the intensity of the SEELEM signal measured at two different locations of the SEELEM surface was correlated with lifetimes of the SEELEM detectable states.

Those measurements yielded lifetimes for the S_1 $3\nu_3$ states of acetylene that were longer than 200μs. This result was also inconsistent with previous findings from the literature [68, 133, 112]. The first-generation chamber measurements were corrupted by various factors which needed to be corrected for. The first factor was a geometrical consideration: the molecules were expanded as a free-jet in the first-generation apparatus and, therefore, the solid angle of the molecular beam intercepted by the SEELEM surface changed considerably at the two detector positions used for the lifetime measurements. There was also the concern that the detectivity could change as a function of SEELEM surface to excitation region distance. The operating background pressure in the first-generation apparatus was high ($\sim 2 * 10^{-5}$ Torr which corresponds to a mean free path (λ_p) of 2.5 m using the collision cross-section for N_2 which is 0.43 nm^2) and it was known that the SEELEM detectivity went down during the course of a detection event due to build-up of molecules from the jet on or in front of the SEELEM surface. Therefore, it was expected that SEELEM detectivity would go up when the SEELEM surface was moved back from the excitation region to a distance where the number density of molecules in the molecular beam had decreased causing less build-up on or in front of the SEELEM surface.

Since it was difficult to quantitatively describe the suspected surface contamination as a function of SEELEM surface to excitation region distance, no correction was attempted [29]. However, the geometrical effect *was* taken into account when the lifetimes of the SEELEM detectable states were computed [29]. Despite this correction, which involved assumptions about the shape and expansion of the volume of excited molecules as they travelled toward the SEELEM surface, the calculated lifetimes were too long to be reconciled with previous findings. One hypothesis which attempted to explain these long lifetimes proposed that the SEELEM detectable eigenstates had appreciable S_0 ground state character which would lengthen their lifetimes. Acquiring appreciable S_0 character would require a reasonably strong coupling between S_1 and S_0 and/or between T_i and S_0. However, the hierarchy of couplings between the electronic states of acetylene deduced by Dupré *et al.* in Zeeman Anticrossing (ZAC) and Zeeman Quantum Beat (ZQB) experiments ranks $S_0 \sim T$ and $S_0 \sim S_1$ couplings as very weak (~MHz) [43, 40, 41, 42]. Furthermore, SEELEM spectra of the S_1 $4\nu_3$ state of acetylene show no signatures of dissociation such as broadening, despite the fact that this level lies above the dissociation limit for S_0. The timescale for dissociation is much shorter than the timescale of the SEELEM experiment (ns vs. μs respectively)[1], therefore any dissociation due to S_0 character of the eigenstates would be expected to manifest itself in the SEELEM spectra of S_1 $4\nu_3$ if the eigenstates possessed significant S_0 character. Based on these two findings, it is difficult to justify invoking of the S_0 state to explain the observed lifetimes.

It is more likely that there was again a source of error that invalidated the lifetime measurements performed in the first chamber. The error could have led to inappropriate corrections for the geometrical factors, as these corrections *did* include certain assumptions about parameters not easily characterized. Alternatively, the accumulation of molecules from the jet on or in front of the SEELEM surface could have given rise to inaccurate measurements.

The more carefully we analyzed the questions regarding the SEELEM detectable states of acetylene, the more it became apparent that we needed to improve our

---

[1] The upper bound for the dissociation event from the S_1 manifold has been determined as 40 - 70 ns by Hashimoto *et al.* in a pump-probe measurement [56]. Specifically, Hashimoto and colleagues measured H-atom decay in 69 ns at V^5K^1, $J' = 2$ ($E_{excess} = 1192.6$ cm^{-1}) and in 38 ns at V^6K^1, $J' = 2$ ($E_{excess} = 2168.3$ cm^{-1}). The lower bound is set by the rotational period: since the $\tilde{A}$ - $\tilde{X}$ band of acetylene shows distinct rotational structure, any dissipation process from the S_1 manifold has to be slower than the molecular rotation period ($\sim$ 1 ps)

vacuum conditions to eliminate hindering conditions such as decline of SEELEM surface detectivity, and isolate the effects we wanted to observe. Since one of the questions that the first-generation apparatus failed to address conclusively was the issue of lifetimes, a new set of lifetime measurements was performed once the second-generation apparatus came online.

3.2 Lifetime Measurements in the Second-Generation Apparatus

The lifetime measurements performed in the second-generation apparatus were two-point measurements in which the SEELEM surface to excitation region distance was varied. The features of the second-generation apparatus that made this measurement successful are summarized below:

The operating pressure in the detector chamber of the second-generation apparatus is typically $4 * 10^{-7}$ Torr ($\lambda_p = 123$ m using the collision cross-section for N_2 which is 0.43 nm^2), or a factor of 50 better than what was achieved in the first-generation apparatus. This improvement in vacuum led to a significant improvement in SEELEM surface conditions. Spectra that were acquired at two different laser-nozzle delays to assess the effect of surface contamination and formation of pre-detector cloud by incoming metastable molecules yielded no significant differences (see Chapter 4 for details) implying that the second-generation apparatus does not suffer from at least one of the major problems that plagued the first-generation machine.

The molecular jet produced in the second-generation apparatus was skimmed and was well collimated. The collimation achieved was a consequence of both the presence of a skimmer and the higher He : C_2H_2 ratio (5:1) used in the second-generation apparatus (in fact, in most experiments performed in the first-generation apparatus, a pure acetylene beam was used). The higher He : C_2H_2 ratio enhanced the mass-focussing effect discussed in the previous section and contributed to the collimation of the molecules of interest along the molecular beam axis. Figure 3-3 depicts a simple geometrical argument which demonstrates that the second-generation apparatus does *not* suffer from the geometrical limitation that confounded the lifetime measurements in the first machine. For both "far" and "close" positions of the SEELEM surface relative to the laser excitation region, the entire cross section of the collimated molecular beam is captured by the SEELEM surface. This is determined by computing the transverse velocity of the molecules that *barely* make it through the skimmer. These molecules define the outer edge of the cone of expanding molecules after the skimmer. The transverse distance travelled by these molecules during the flight time from the nozzle to the SEELEM detector is calculated and compared to the radius of the SEELEM surface (Au in this case). As can be seen, even when the SEELEM surface is at its "far" position for the lifetime measurements, the entire cross-section of the molecular beam ($\sim$ 1.8 cm in diameter) is captured by the SEELEM surface ($\sim$ 2.3 cm in diameter).

The lifetime measurements were performed by first placing the SEELEM detector (Au metal) at the "close" position to the laser excitation region (15.8 cm away from laser excitation region), locking onto a UV-LIF peak (*i.e.* a certain rotational line of the $3\nu_3$ band) whose intensity was later used for signal normalization, and acquiring a TOF profile from which the SEELEM intensity for that particular peak was deduced. After one set of measurements was completed for the "close" position of the SEELEM detector, the detector was moved to the "far" position (27 cm away from laser excitation region) and the TOF data was acquired again. It should be emphasized at this point that the SEELEM states whose lifetimes were measured in this experiment are not necessarily those which have the largest intensity in the SEELEM spectrum. In order to ensure that the laser was at the same frequency both times the SEELEM intensity was measured, we had to use a strong and sharp feature to lock on to, and UV-LIF peaks were used to achieve this.

The results of these measurements are shown in Fig. 3-4. The error bars are relatively large because the decay constants were determined from only two data points.

The lifetimes of the S_1 $3\nu_3$ states cluster between 50-60 μs, a time interval which is

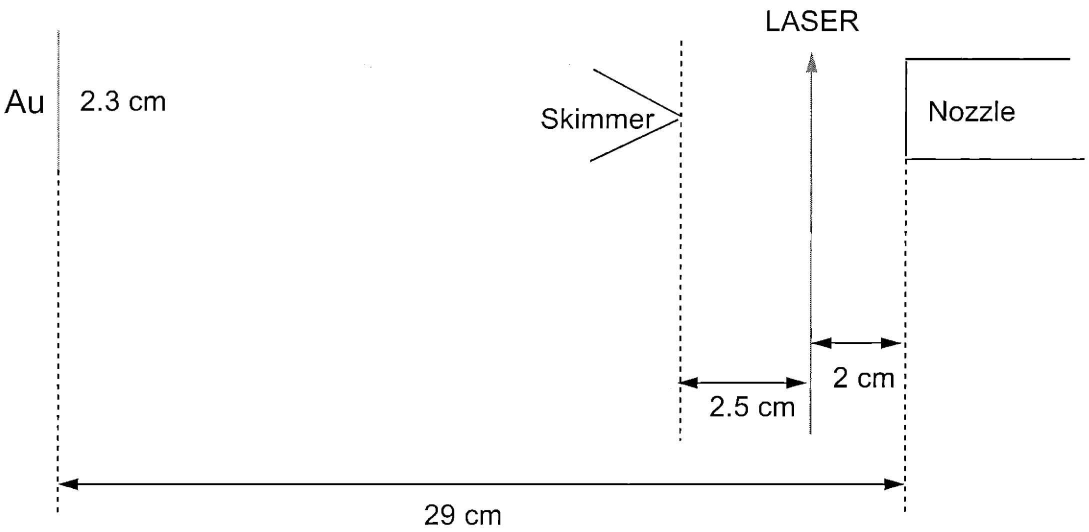

TOF arrival time = 170 microseconds

Speed of jet = 27/170 (laser-Au) = 0.16 cm/microseconds

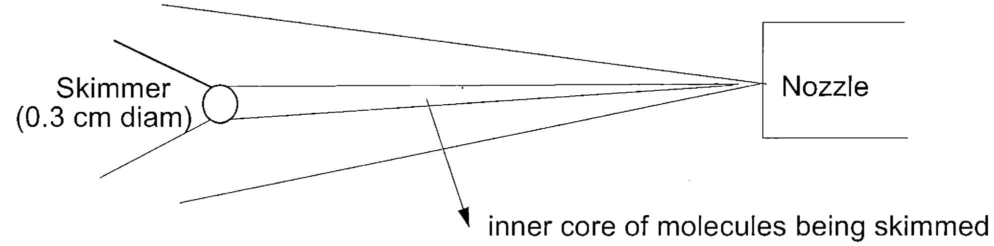

V_{trans} * 4.5 cm / 0.16 cm/μs = 0.15 cm

V_{trans} = 0.005 cm/μs

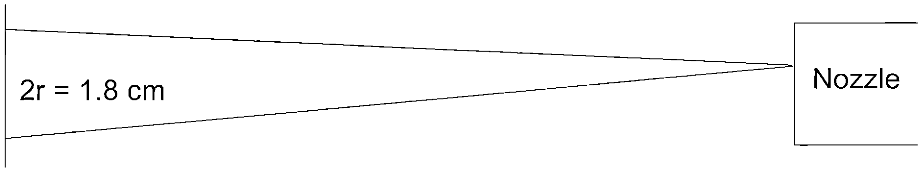

r = 0.005 cm/μs * 29 cm / 0.16 cm/μs = 0.9 cm

All molecules that make it into the detector chamber are captured on Au

Figure 3-3: The experimental configuration for the lifetime study of the S_1 $3\nu_3$ states of acetylene.

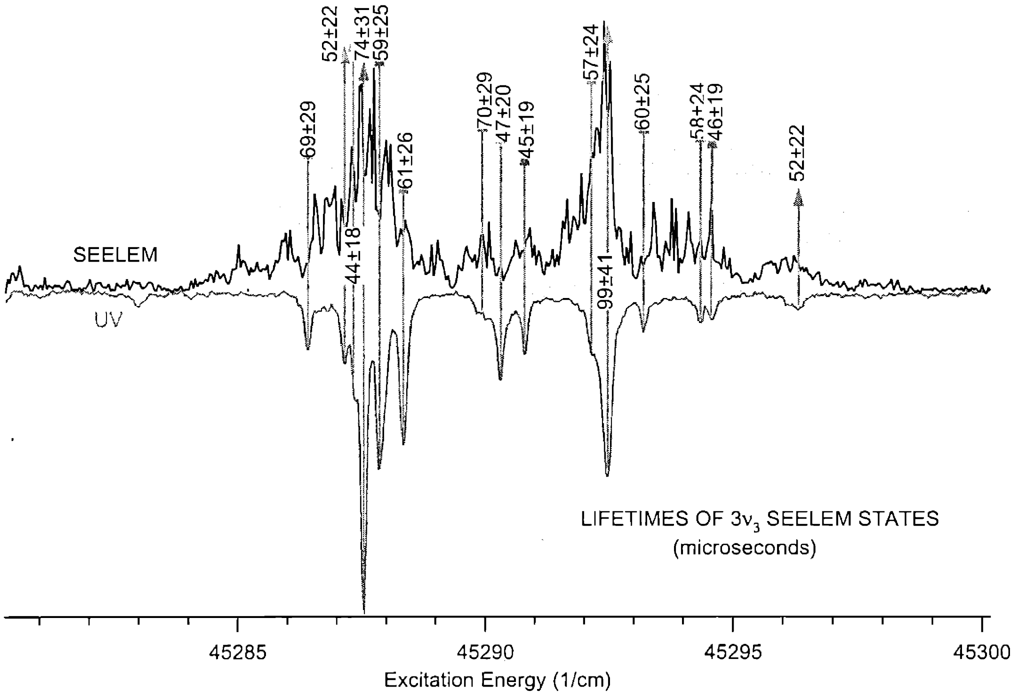

Figure 3-4: The measured lifetimes of SEELEM detectable states of S_1 $3\nu_3$. The measurements were made by locking onto UV-LIF peaks, therefore the SEELEM states selected for the lifetime measurements are not necessarily those that have the highest intensity in the SEELEM spectrum.

in good agreement with the predicted maximum of the theoretical SEELEM intensity curve as a function of lifetime, computed using the SEELEM intensity equation that will be introduced in Chapter 5. The theoretical curve is shown in Fig. 3-5. The SEELEM intensity expression for Au is a function of the fractional T_3 character of the eigenstates as well as the fractional S_1 state character. Although the fractional T_3 character of the eigenstates is not known *a priori*, it is still possible to calculate a SEELEM intensity vs. lifetime curve by assuming a reasonable fractional T_3 character for the eigenstates. Changing the value of the fractional T_3 character does not significantly change the profile of the SEELEM intensity curve as a function of lifetime, therefore the fractional T_3 character turns out not to be a crucial parameter for this calculation.

The lifetimes of the UV-LIF detectable states were also measured. The results are shown in Fig. 3-6. These lifetimes were determined simply by observing the fluorescence decay curve of the eigenstates on the oscilloscope. These lifetimes are in agreement with results reported by Ochi and Tsuchiya [105].

3.3 S_1 Bright State Character of the Metastable Eigenstates

The measured lifetimes of the SEELEM detectable states were converted into fractional S_1 bright state characters by the following equation:

$$\frac{1}{\tau_m} = \frac{C_{S_1}^2}{\tau_{S_1}} + \sum_i \frac{C_{T_i}^2}{\tau_{T_i}} \tag{3.4}$$

where τ_m is the lifetime of a mixed state ($\Psi_m = C_{S_1}|S_1> + \sum_i C_{T_i}|T_i>$). It was assumed that the lifetimes of the triplet electronic states are longer than that of S_1, and therefore, the above equation was simplified to:

$$C_{S_1}^2 \approx \frac{0.27}{\tau_m} \tag{3.5}$$

where 0.27 is τ_{S_1}, the radiative lifetime of the singlet state S_1. There have been experimental results from Hg-photosensitized reactions of acetylene [146] which report

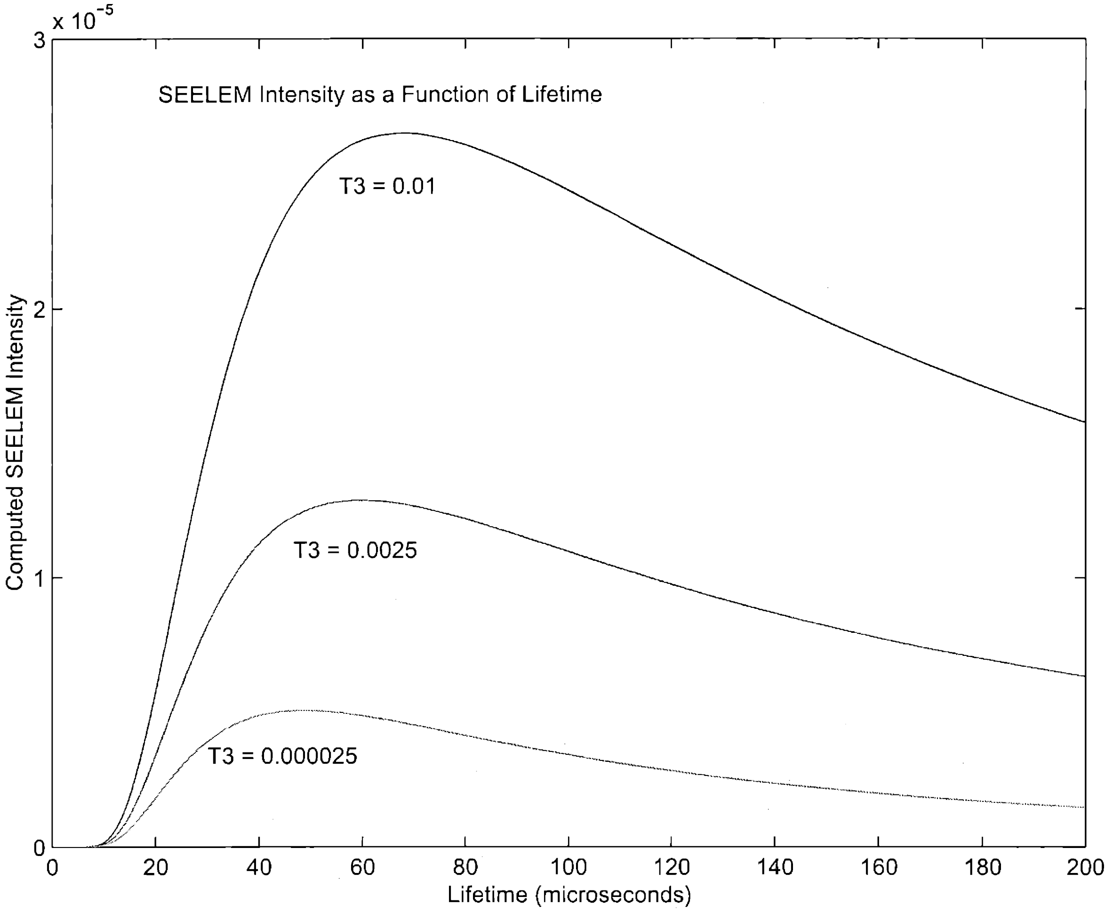

Figure 3-5: Calculated SEELEM intensity curve as a function of eigenstate lifetimes. Although the fractional T_3 character of the eigenstates is a parameter in the calculation and is not known *a priori*, its value does not affect the time window over which the maximum SEELEM intensity occurs. There is only a slight shift in the position of the maximum.

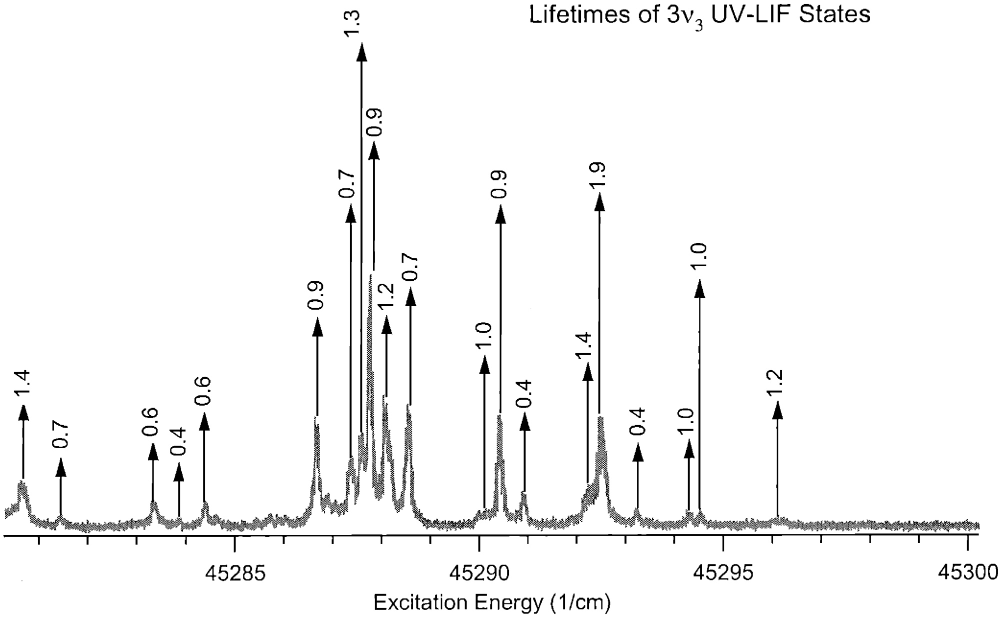

Figure 3-6: The lifetimes of the UV-LIF states of S_1 $3\nu_3$ measured in the second-generation apparatus from fluorescence decay curves. Indicated lifetimes are in microseconds.

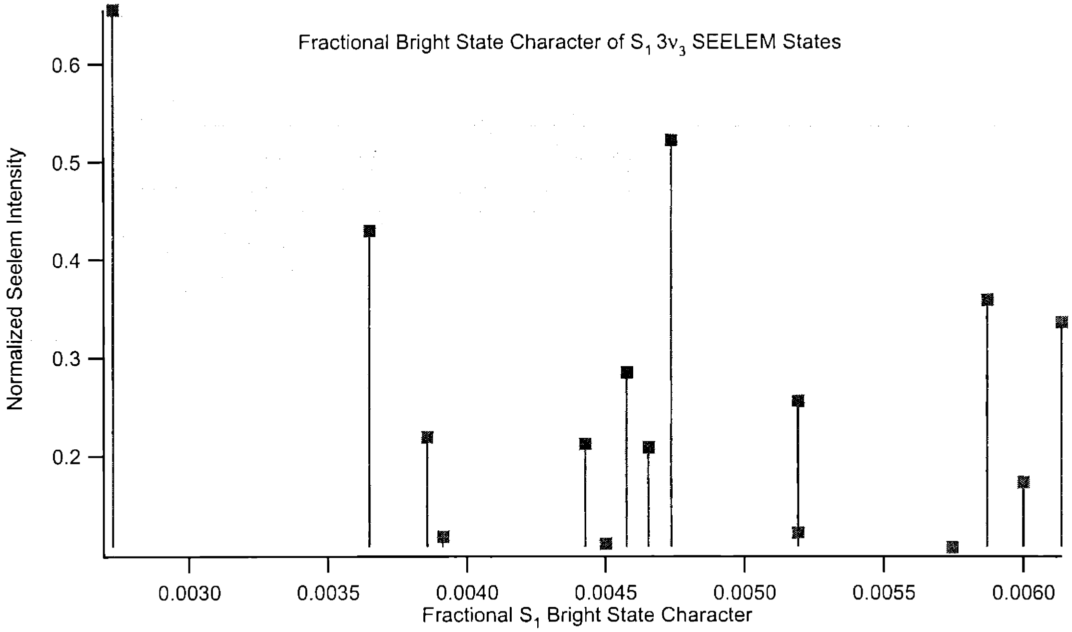

Figure 3-7: The distribution of fractional characters of the S_1 $3\nu_3$ SEELEM states measured in the second-generation apparatus.

a lifetime on the order of a few hundred microseconds for the T_2 state. Therefore, the assumption about the relative lifetimes of singlet vs. triplet states which led to the simplification above is in fact reasonable.

The distribution of the fractional S_1 bright state characters as a function of SEELEM intensity is displayed in Fig. 3-7. According to these results, we can detect eigenstates with fractional S_1 bright state character less than 0.003 with our SEELEM detector with Au as the SEELEM surface. Comparing this to the lower limit on the fractional bright state that can be observed in a UV-LIF spectrum which was reported as 0.01 by Drabbels *et al.* [35], one can see that the SEELEM detector is indeed a detector of the "dark" eigenstates. The two schemes, UV-LIF and SEELEM, exclusively detect different eigenstates.

Although the lifetimes obtained in the measurements in the second-generation apparatus were in agreement with the theoretical prediction of where the SEELEM intensity maximum should occur as a function of fractional bright state character, another set of simulations was performed to test the reasonableness of these results.

A 213x213 matrix was constructed where the bright basis state S_1 was coupled to a background manifold of dark states T_i through the intermediary of a doorway state T_3. The details of this matrix are described in Chapter 5. Some of the parameters that were used in the construction of this matrix, such as the density of states, were chosen based on either experimental data or *ab initio* calculations. Other parameters for which there was no available information, were judiciously chosen. This matrix was diagonalized and the SEELEM signal from each eigenstate was computed as a function of time using the SEELEM expression introduced in Chapter 2. The SEELEM curves for several eigenstates are illustrated in Fig. 3-8.

The SEELEM signal for each eigenstate was integrated over a time window which was representative of the time window that we use in our experiments to collect the SEELEM signal (20 - 30 μs). The fractional S_1 character of each eigenstate was then plotted against its integrated SEELEM signal. The result is illustrated in Fig. 3-9.

The computed fractional bright state characters are in agreement within a factor of 2 with the fractional bright state characters calculated from lifetime measurements. This was a very encouraging result, especially considering the fact the Hamiltonian used in the calculation was not a spectroscopically determined "effective" Hamiltonian, but a reasonable construction based on what we know about our system so far.

The agreement between our measured lifetimes and a calculation which made use of the information we have pieced together about our molecular system so far, was very satisfying since it pointed to the fact that the different approaches we adopt towards understanding the distribution of bright state character in our system, give rise to an internally consistent picture.

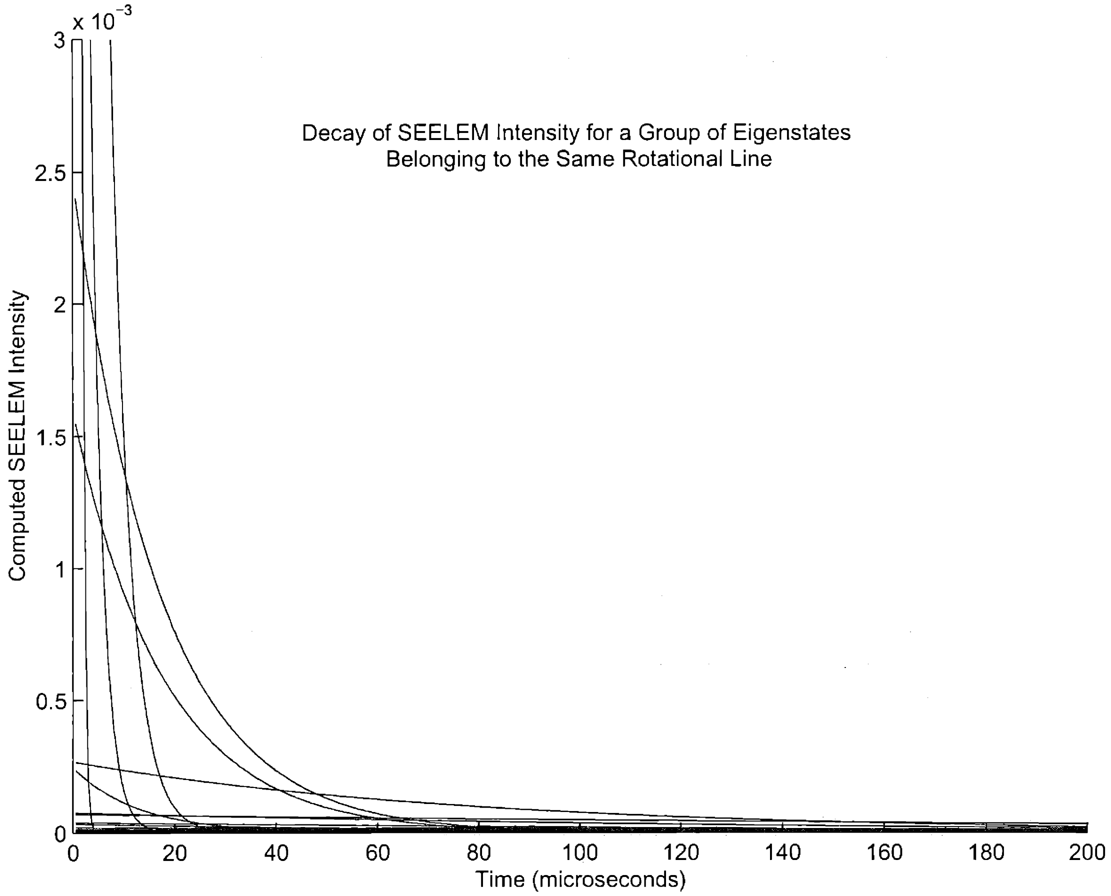

Figure 3-8: Hypothetical SEELEM decay curves computed for several eigentates that result from the diagonalization of a Hamiltonian that is based on a doorway-mediated coupling between the bright state and the background dark states. All of these eigenstates are fractionated components of the same $J' \leftarrow J''$ transition.

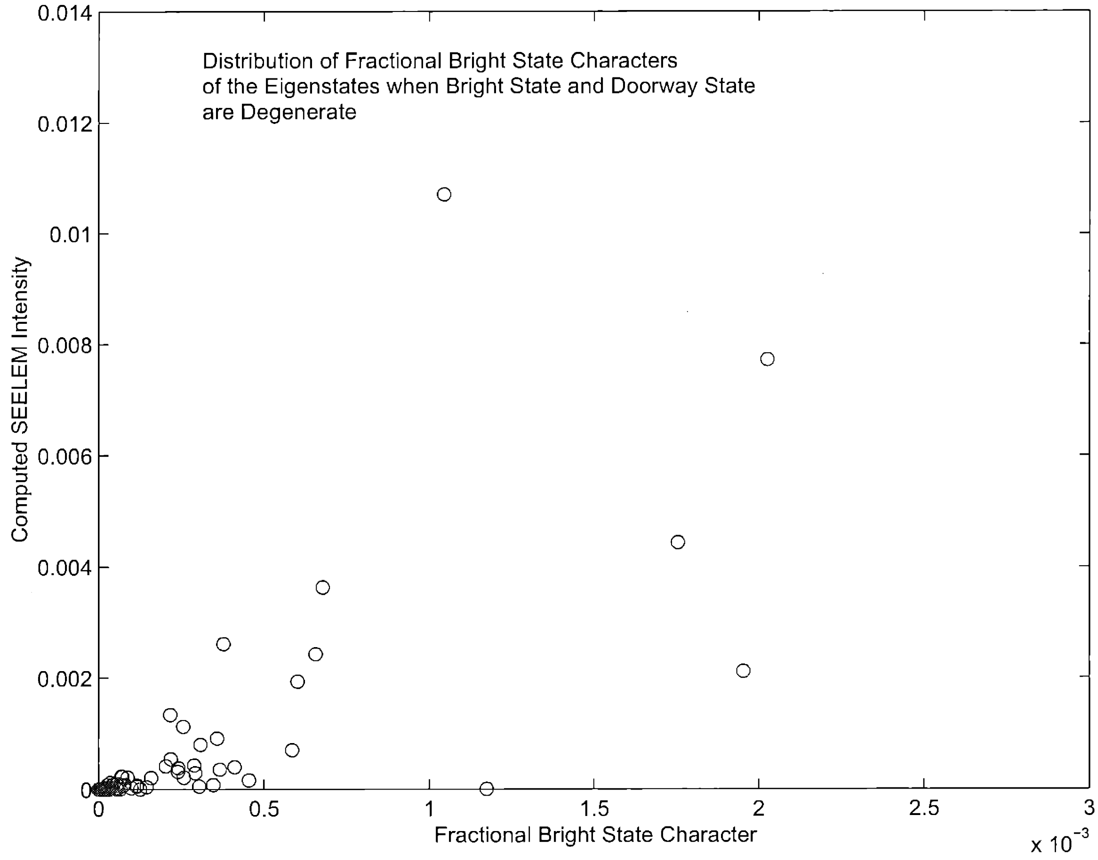

Figure 3-9: Hypothetical fractional bright state character of eigenstates as a function of their SEELEM signal, integrated over an experimentally relevant time window (20 - 30 μs). The fractional bright state character of the eigenstates cluster around values which are in satisfactory agreement with the fractional bright state characters determined from experimental lifetime measurements.

Chapter 4

The Mechanism of Surface Electron Ejection by Laser Excited Metastable Molecules

Surface Electron Ejection by Laser Excited Metastables (SEELEM) is a useful, but poorly understood form of laser excitation spectroscopy, whereby nominally forbidden transitions that result in the excitation of molecules into long-lived, electronically excited states are selectively (and sensitively) detected. When a molecule in a metastable (lifetime $> 100\mu$s) electronically excited state impacts a metal surface, an electron is ejected and detected, provided that the vertical electronic excitation energy exceeds the work function of the metal. The interaction between the excited molecule and metal surface is sensitively dependent on extrinsic and intrinsic factors, such as respectively metal surface contamination and whether the electronic deexcitation is electron spin-allowed or forbidden. SEELEM spectra of acetylene in the region of the $\tilde{A}\ {}^1A_u \leftarrow \tilde{X}\ {}^1\Sigma_g^+$ ($S_1 \leftarrow S_o$) $V_0^3K_0^1$ [1] band illustrate the effects of detector surface contamination on the relative detectivities of S_1, T_3, and T_1 electronic states on Au ($\Phi = 5.1$ eV), Y ($\Phi = 3.1$ eV), and Cs ($\Phi = 2.1$ eV) surfaces. Deexcitation via a spin-allowed transition is shown to be much more robust with respect to sur-

---

[1] Here "V" stands for the *trans*-bending mode, and "K" stands for the projection of **J**, the total angular momentum, along the *a*-axis.

face contamination than a spin-forbidden deexcitation. When the metal surface is contaminated by adsorbed acetylene, the efficiency of SEELEM detection is significantly reduced, and the surviving detectivity derives from the minuscule fractional S_1 character in predominantly T_1 eigenstates. When the SEELEM surface is less contaminated, the relative detectivities and spectral profiles on Au, Y, and Cs surfaces reflect the $\sim$**1000** times larger density of T_1, T_2 than S_1, T_3 vibrational states.

4.1 Introduction

Triplet states play an important role in the intramolecular energy redistribution of isolated molecules and in photochemical reactions. The chemical and structural properties of triplet states are profoundly different from those of the electronic ground state, the singlet S_0 state. Their metastability (radiative lifetime $\tau > 100\mu$s), electronic energy content ($\geq$ 2 eV or 50 kCal/mol), open-shell electronic structure, and capability of existing in multiple isomeric forms combine to make triplet states potentially important in many chemical reaction processes, especially those initiated by ultraviolet radiation, electron-molecule and ion-molecule collisions, or hypersonic collisions with unexcited molecules and solid surfaces. However, despite the practical and fundamental importance of triplet states, the investigation of their structural, dynamical, and chemical kinetic properties has been limited due to the low oscillator strength of $T \leftarrow S_o$ transitions and the low spontaneous fluorescence decay rates of the triplet states.

The study of triplet states has picked up new momentum following the introduction of supersonic beam techniques, which enable the interrogation of the intramolecular dynamics of cold isolated molecules excited to well defined quantum states. The pioneering work on the dynamics of triplet states in beams was conducted by Smalley and his co-workers [39, 33, 32]. They generated triplet states, either by direct $T \leftarrow S_o$ optical excitation via the singlet character "borrowed" from energetically remote perturbers or indirectly via an Intersystem Crossing (ISC) process subsequent to direct optical excitation of a singlet state. They monitored the rate of decay of triplet population into high vibrational levels of the ground singlet state with an ionization laser pulse delayed with respect to the excitation laser pulse. The ionization pulse had sufficient energy to ionize any population in triplet states, but not sufficient energy to cause ionization from the high vibrational levels of the ground state. By changing the delay between the ionization and the excitation pulse, they were able to measure rates of ISC between triplet states and the high vibrational levels of the ground singlet state. The method of delayed ionization has since been used to determine rates of ISC in a wide range of molecules [39, 33, 32, 114, 107, 132, 80].

Other experimental schemes for the detection of triplet states in molecular beams include Suzuki *et al.*'s and Ito and co-workers' method of sensitized phosphorescence [133, 112, 2, 75, 76, 106], Villa *et al.*'s method of multiphoton ionization [144], Pratt and co-workers [125, 126, 127, 138], Penner *et al.* [108], and Villa *et al.*'s [143] use of laser induced phosphorescence to monitor the direct excitation of large molecules to their triplet states. More recently, Sneh and Cheshnovsky introduced a new technique for the investigation of "dark" metastable molecules produced via radiationless processes following excitation by laser light [116, 121, 117, 119, 118, 120, 123, 11, 21, 122]. Their technique is based on the phenomenon of electron ejection from low work-function surfaces induced by excited molecules. Sneh and Cheshnovsky report that the new technique, which they have named as Surface Electron Ejection by Laser Excited Metastables (SEELEM), yields results in good agreement with those obtained from Delayed Ionization experiments in the determination of the decay rates of triplet states of large molecules [116]. They have also shown SEELEM detection sensitivity is independent of excess vibrational energy in the triplet state [116]. The basic idea behind SEELEM had actually been developed by Klemperer, Freund and coworkers [49, 57] for the detection of metastables generated by electron impact in effusive beams. Sneh and Cheshnovsky enhanced the power of this method by replacing electron bombardment by laser excitation and by generation of triplet states via radiationless processes in a supersonic beam.

Sneh and Cheshnovsky applied SEELEM mostly to the study of triplet decay rates and the quantum efficiencies of nonradiative processes in large molecules (*e.g.*

aniline, pyrazine). We use SEELEM to interrogate the triplet states of small polyatomic molecules (*e.g* acetylene) with the goal of understanding the details of the radiationless process that transforms population into triplet states. Uncovering the mechanistic details of how triplet states are populated could lead to the development of schemes to selectively excite these states and open up possibilities of using triplet states as platforms for new kinds of spectroscopic, dynamical, external control, photochemical, and chemical kinetics experiments.

SEELEM is our primary experimental tool to investigate triplet states and, hence, it is important to characterize this detection scheme. Although there is a rich literature describing the process of de-excitation of excited atoms on impact with metal surfaces, the theory has not been fully extended to the case of $S_1 \sim T_i$ mixed molecular eigenstates (*e.g.* $|\Psi_{mixed}>= \alpha|\Psi_{S_1}> +(1-\alpha^2)^{\frac{1}{2}}|\Psi_T>$) interacting with surfaces. The seminal review of the mechanism of interaction of excited atoms with metal surfaces is by Hagstrum [53]. Silbey *et al.* have described the fate of an oscillating dipole in close proximity (a few Å) to a surface from a semiclassical point of view [17]. More recently Hotop has reviewed the mechanisms of the detection of metastables on surfaces [61]. Hotop demonstrates that the detection mechanism and efficiency are intimately linked to the condition of the detector surface.

A comparison of the data we have acquired in two molecular beam machines with different base pressures has led us to conclude that the quantum efficiency of SEELEM detection of a metastable state that has predominantly dark state (T) character, derives from its minuscule bright state (S_1) character if the SEELEM surface is contaminated by adsorbates. This is due to the fact that deexcitation via a spin-allowed transition takes place through a long-range interaction and, hence, is more robust with respect to surface contamination. However, if the SEELEM surface conditions are improved, the short-range tunneling interaction channel, which allows spin-forbidden deexcitation, is opened and the dark character of the metastables can be detected as well.

In this chapter we report our findings that demonstrate the critical dependence of the efficiency of the SEELEM process for triplet and singlet fractional characters of mixed molecular eigenstates on extrinsic factors such as the background pressure during detection. We propose that at sufficiently low background pressures, where the short-range interaction pathway is not suppressed, SEELEM on low-work function metals such as Cs ($\Phi_{Cs} = 2.1$ eV) can be exploited as a sensitive method to detect the triplet fractional characters of mixed molecular eigenstates. Being sensitive to the triplet fractional character of an eigenstate as opposed to being limited to detecting exclusively its fractional bright state character, opens up the possibility of being able to observe nominally "dark" eigenstates excited in direct triplet - singlet transitions and determine the fractional S_1, excited triplet, and lowest triplet characters in each eigenstate. This distribution of eigenstate characters will provide a fundamental understanding of the mechanisms of excitation, ISC, and detection.

4.2 SEELEM Spectra

SEELEM spectra are recorded in a second-generation version of an apparatus described previously [68, 5]. The first-generation molecular beam machine, in which the SEELEM spectra displayed in Fig. 4-3 were acquired, consisted of a single vacuum chamber which contained two detectors: a photomultiplier tube (PMT) and a SEELEM detector. The operating pressure in this chamber was $2 * 10^{-5}$ Torr. The current apparatus is a doubly-differentially pumped vacuum chamber (see Chapter 2 for details), where the operating pressure in the "detector" compartment that houses the SEELEM detector is $4 * 10^{-7}$ Torr. This chapter will compare SEELEM spectra that were acquired separately in the two chambers.

4.3 Results and Discussion

An expression for the intensities in the SEELEM spectrum has been proposed previously [68, 5] and will be re-introduced in more detail in Chapter 5,

$$I_i^{SEELEM} = C_{S_1}^2 \times \left[e^{-\Delta t \times \gamma}\right] \times (C_{S_1} + \alpha\ C_{T_i})^2, \tag{4.1}$$

where γ is the decay rate via spontaneous emission given by $\gamma = (\frac{1}{0.27\mu s}) \times C_{S_1}^2$. The flight time, $\triangle t$, may be changed between $94 - 156$ μs for a 20% mixture of C_2H_2 seeded in He, by varying the distance from the excitation region to the SEELEM surface. 0.27 μs is the intrinsic lifetime of a pure singlet eigenstate [68]. C_{S_1} and C_{T_i} denote the singlet (bright) and triplet (dark) amplitudes of the mixed molecular eigenstates created upon laser excitation. The SEELEM detectivity expression is a product of three factors:

1) the excitation probability (the fractional bright state character of each mixed molecular eigenstate), $C_{S_1}^2$;

2) the probability of surviving the flight time, $\triangle t$, from excitation until impact on the detector while *preserving the electronic excitation*, which is also determined by the fractional S_1 character, $C_{S_1}^2$;

3) the SEELEM detectivity, which is related to the square of the weighted sum of the amplitudes of the basis states that lie at vertical electronic excitation energies larger than the work function of the SEELEM metal. For example, in the case of Au ($\Phi = 5.1$ eV), only the S_1 and T_3 basis state characters are detectable. However, when Cs ($\Phi = 2.1$ eV) is used as the SEELEM detector surface, all electronically excited states of acetylene, including T_1, contribute to the detectivity, at least in principle. Whether one achieves the expected increase in SEELEM signal strength due to turning on the detectivity of a higher density of excited triplet vibrational states, is shown here to depend crucially on the background pressure at which the SEELEM measurement is made. Figure 4-1 compares the energies of the electronic states of acetylene to the work functions of some of the metals used as SEELEM surfaces.

Because S_1 and T_i represent electronic surfaces with different total electron spin, their intrinsic SEELEM detectivities are not expected to be identical. Therefore, a phenomenological scaling factor, 'α', was inserted into the detectivity factor of the SEELEM expression (Eq. 5.6). Most experimental studies of the interaction mechanisms of electronically excited gaseous species with metal surfaces have involved

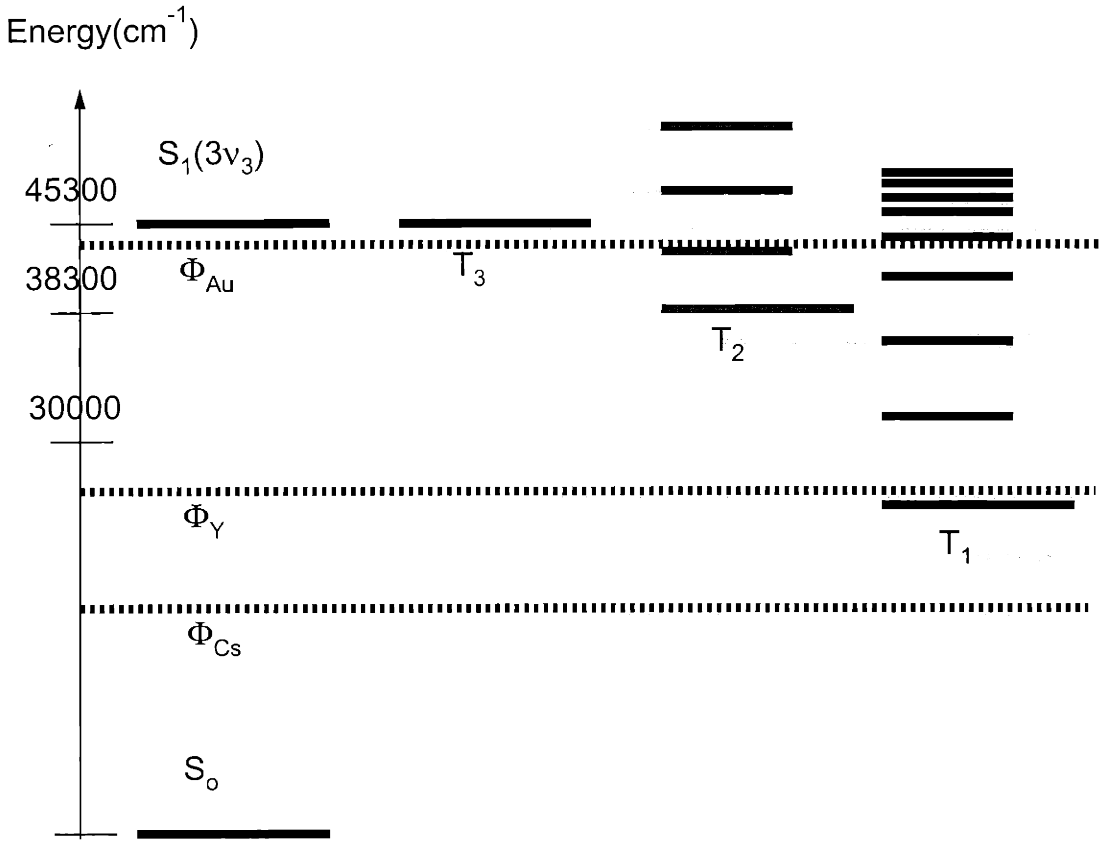

Figure 4-1: A schematic of the energy levels of acetylene and the work functions of the SEELEM metals used to probe the populations in these levels.

atoms. It is known that an atom in an electronically excited singlet state can give rise to electron ejection on impact with a metal surface through two pathways [53]. In the first pathway, the excited electron of the atom relaxes to fill the vacancy in the lowest unfilled atomic orbital, whereupon the energy released by this deexcitation causes an electron to be ejected from the conduction band of the metal (Fig. 4-2). In the second pathway, an electron from the conduction band of the metal tunnels through a barrier into the vacancy in the lowest energy unfilled atomic orbital, thereby causing the excited electron on the atom to be ejected. For an electronically excited atom in a triplet state, the first of these two signal pathways is not viable since it would require a spin flip of the excited electron as it relaxes into the singlet ground state. Extending this picture to the case of S$\sim$T mixed eigenstates, it is reasonable to expect that for a mixed state with comparable fractional SEELEM-detectable singlet and triplet characters, the SEELEM detectivity arising from the fractional singlet character would be larger than that arising from the triplet character. Hence, it is appropriate to incorporate a phenomenological scaling factor into the SEELEM signal expression to account for this expected difference in the S_1 vs. T_i detectivities.

For the SEELEM processes described by Fig. 4-2, pathway I can be considered as a "long-range interaction" pathway. The singlet character of S$\sim$T mixed eigenstates can de-excite through this singlet-only pathway, resulting in the emission of an electron. Pathway II, which is the only viable pathway for the de-excitation of the triplet character, is a "short-range interaction" or "tunneling" pathway since it requires overlap between the orbitals of the mixed molecular state and the orbitals of the metal conduction band. The short-range interaction pathway should be more sensitive to the cleanliness of the SEELEM surface and, hence, the background pressure. In fact, the short-range interaction pathway can shut down under high background pressures [61]. This would result in a further reduction of the detectivity for the triplet character of a mixed molecular eigenstate relative to that for the singlet character. The efficiency of the SEELEM process for the triplet character relative to the singlet character is likely to depend sensitively on the background pressure, and this dependence is additional motivation for the introduction of the empirical parameter, $\alpha(\text{P})$, into the SEELEM

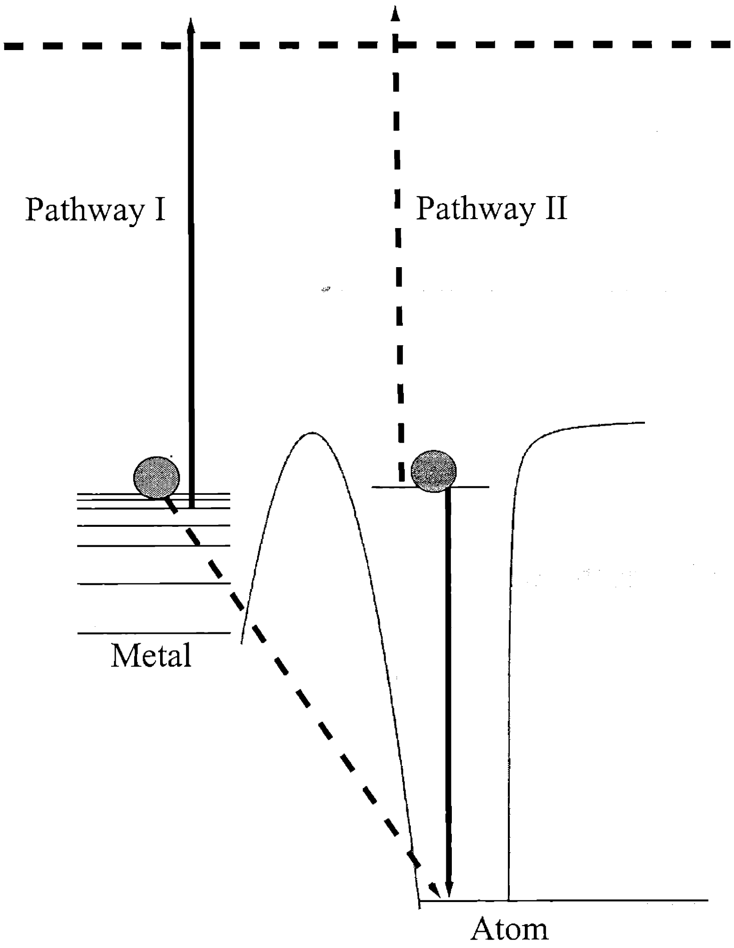

Figure 4-2: The two mechanisms of the de-excitation of an electronically excited atom on impact with a metal surface. The upper horizontal dashed line represents the energy of a free electron. The excited atom starts interacting with the metal at a distance of a few $\mathring{A}$ from the surface. Pathway I, represented by the solid lines, involves ejection of an electron from the conduction band of the metal by the energy released when the excited electron in the atom relaxes to the ground state. In pathway II, represented by the dashed lines, an electron from the conduction band of the metal falls into the half filled orbital of the atom causing the excited electron on the atom to be ejected. This figure was inspired by Figure I in [53].

intensity expression.

The form of the detectivity factor (Eq. 5.6) suggests that quantum interference effects between the contributions of different classes of basis states will be a characteristic (and perhaps diagnostically useful) feature of SEELEM spectra, especially when the eigenstate density exceeds the spectral resolution. Collision with the SEELEM surface could induce inelastic transitions among eigenstates, which would reduce or eliminate the expected interference structures in SEELEM spectra. However, in the limit where the density of SEELEM nondetectable basis states is vastly in excess of the SEELEM detectable ones, inelastic collisions with the SEELEM surface are not expected to alter the spectrally averaged SEELEM detectivity, but should smooth out the sharp structures associated with constructive/destructive interference.

Figure 4-3 shows two overlaid SEELEM spectra corresponding to a section of the R-branch region of the $\tilde{A} \leftarrow \tilde{X}\ \ V_0^3 K_0^1$ band of acetylene. These spectra were recorded in the first-generation apparatus where the background pressure was $2 * 10^{-5}$ Torr during detection. The SEELEM spectrum displayed as a darker line was recorded on Au ($\Phi = 5.1$ eV); and the SEELEM spectrum shown as a light line was recorded on Cs ($\Phi = 2.1$ eV). The Au and Cs detection surfaces were both located 10 cm from the excitation region. The Au surface was heated to 300°C while the spectrum was recorded in an attempt to minimize the buildup of physisorbed acetylene on the metal surface. Cs was continuously coated onto a rotating copper wheel while the spectrum was recorded. Coating was done at the upper half of the copper wheel while the metastables impacted the lower half. The wheel was rotating at 2 rpm and the time required for the freshly coated Cs to rotate 180° into the path of the incoming metastables was 15 seconds.

It is useful at this point to estimate the flux of background molecules onto the SEELEM surface at the prevailing background pressures in our first and second generation chambers. Using the kinetic theory of gases, one can calculate the number of collisions per unit area per unit time under pressure p for a gas with molar mass M. For air, at room temperature, at a pressure of $2 * 10^{-5}$ Torr, the flux of molecules is $8 * 10^{15}/\mathrm{s}/\mathrm{cm}^2$. Since 1 cm^2 of metal surface consists of about 10^{15} atoms, each atom

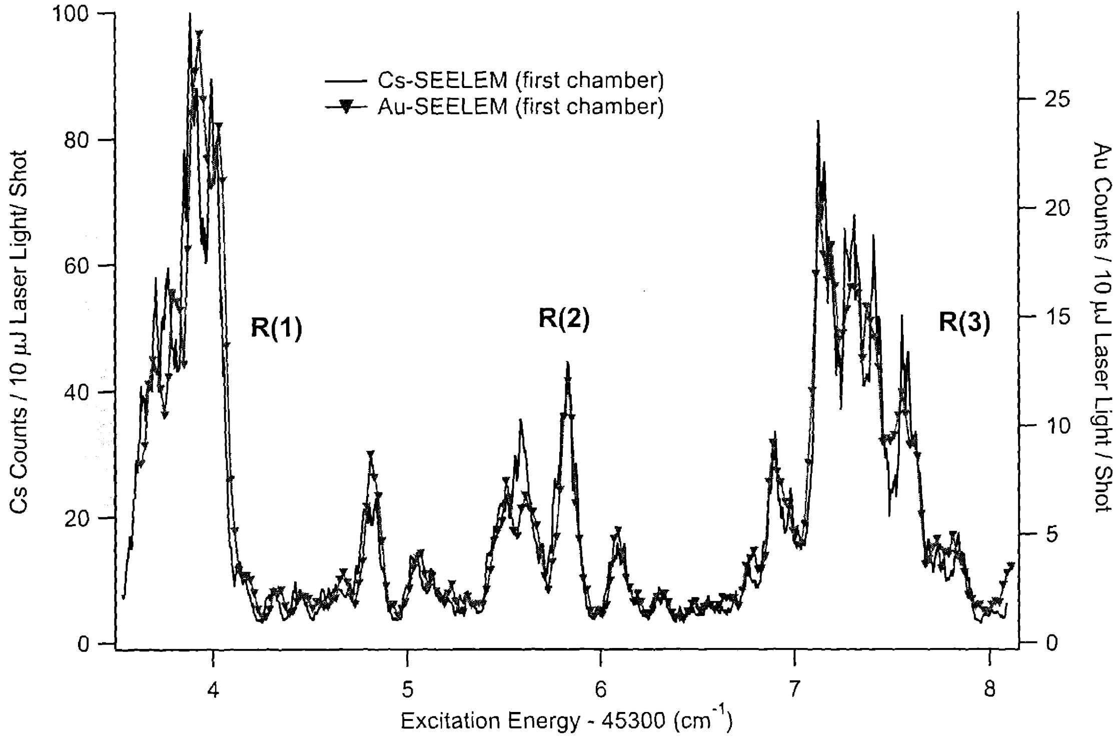

Figure 4-3: The SEELEM spectra of a section of the $\tilde{A} \leftarrow \tilde{X}$ $V_0^3K_0^1$ band of acetylene centered near 220.74 nm. The SEELEM traces were acquired on either Cs (Φ = 2.1 eV) or Au (Φ = 5.1 eV). These spectra were acquired in the first generation chamber where the operating base pressure was $2 * 10^{-5}$ Torr.

is struck about 8 times/s at this pressure. Since it takes 15 seconds for a fresh Cs surface to be exposed to the incoming metastables, each surface Cs atom is struck $\sim$120 times by background molecules before the arrival of the first signal molecules. It is difficult to estimate the fraction of collisions that gives rise to adsorption, however, if one assumes a sticking coefficient of 0.1, one finds that the time required to deposit one monolayer is 1.25 s.

If the background pressure is reduced to $4 * 10^{-7}$ Torr, as in the second-generation apparatus, the fresh Cs atoms on the SEELEM surface suffer only 2.4 collisions during the 15 second period prior to exposure to the incoming metastables. This reduction by a factor of about 50 in the number of collisions suffered by the surface atoms is likely to significantly improve the surface cleanliness and, therefore, keep the short-range interaction channel open, as required for the efficient detection of the triplet character of the metastable eigenstates .

The SEELEM spectra recorded in the first generation apparatus are surprisingly similar in their relative intensities, both feature-by-feature and overall. Au and Cs surfaces are expected to give rise to profoundly different SEELEM spectra, since these metals are capable of detecting different groups of triplet states: only the T_3 and S_1 characters of the eigenstates are detectable on Au, but T_1 *and* T_2 characters, in addition to the T_3 and S_1 characters detectable on Au, should be detectable on Cs (Fig. 1). It should be noted here that the density of $T_{1,2}$ states is expected to be $\sim 10^3$ times larger than the density of S_1, T_3 states. Failure to observe the expected significant differences in the lineshapes and relative intensities of the Au and Cs SEELEM spectra led us to conclude that the triplet character is much less detectable than the singlet character. This implies that the empirical parameter α in the SEELEM intensity expression (Eq. 5.6) is much smaller than 1. The Cs surface does exhibit an overall increase in the signal level by a factor of 3 relative to the Au surface, however, this is much smaller than the expected $\sim 10^3$ increase if T_1 and T_2 basis state characters had also been detectable.

Figure 4-4 is a comparison of two SEELEM spectra featuring a slightly different region of the R-branch of the acetylene $\tilde{A} \leftarrow \tilde{X}$ $V_0^3 K_0^1$ band, recorded this time in the

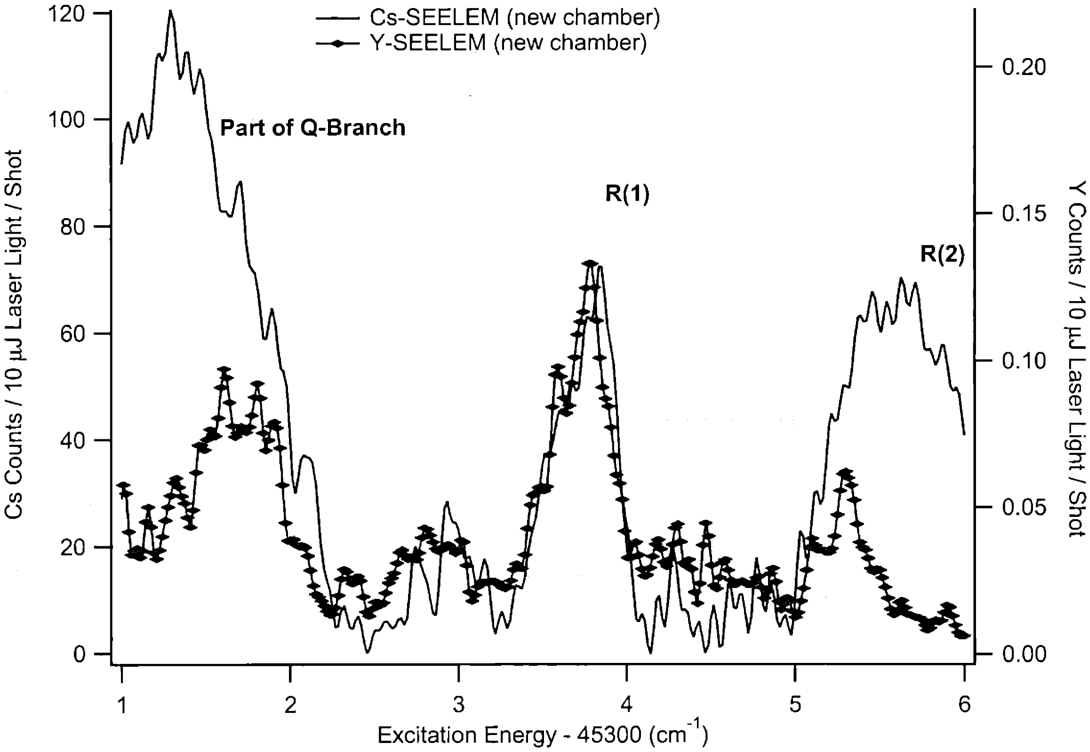

Figure 4-4: The SEELEM spectra of a section of the $\tilde{A} \leftarrow \tilde{X}$ $V_0^3 K_0^1$ band of acetylene centered near 220.74 nm. The SEELEM traces were acquired on either Cs ($\Phi = 2.1$ eV) or Y ($\Phi = 3.1$ eV). These spectra were acquired in the second generation chamber where the operating base pressure was $4 * 10^{-7}$ Torr.

second-generation chamber at a background pressure of $4{*}10^{-7}$ Torr during detection. The first trace (light line) was acquired with Y ($\Phi = 3.1$ eV) as the SEELEM surface and the second trace (dark line) was acquired with Cs ($\Phi = 2.1$ eV). The Y and Cs surfaces were both located 15 cm from the excitation region. Although these spectra are survey spectra, they clearly show that under the improved background pressure condition, the Cs signal is at least 500 times stronger (as determined by the R(1) feature) than the Y signal (which, in turn, is a factor of 3 stronger than Au) and the detailed feature shapes and relative intensities in the two spectra are significantly different. This is a profound contrast with the situation in Fig. 4-3.

The spectra obtained in the new chamber were acquired under quite different conditions than those in the old chamber (different background pressure, different

SEELEM surface to excitation distance, presence of a skimmer, different backing pressure hence a different rotational temperature of the molecular beam, a different electron multiplier [2], and slightly different nozzle-excitation region distance). Therefore, the two sets of SEELEM traces cannot be compared directly to each other, but are internally comparable.

The performance of the second-generation apparatus was tested by recording two SEELEM spectra on Au at different laser-nozzle delays. The laser-nozzle delay parameter is an important parameter which ensures that the laser beam passes through the excitation region precisely at the time the molecules released from the nozzle arrive there. Adjusting the laser-nozzle delay permits excitation of the molecular beam at spatially different points as it traverses the laser excitation region. Each pulse of molecules can be thought of as a "rod of molecules" travelling with a Gaussian distribution of translational velocities which is centered around $1.6 * 10^5$ cm/s. If the laser beam intercepts this rod of molecules at the front edge, then the leading edge of the molecular beam will be composed of excited molecules, and these molecules will collide with the clean SEELEM surface first, giving rise to SEELEM signal. However, if the laser intercepts the rod of molecules at the tail end, then the leading edge of the molecular beam will be composed of unexcited molecules, and if not pumped away sufficiently fast, this leading edge of unexcited molecules could become adsorbed onto the SEELEM surface rendering it less efficient at the detection of the later-arriving, tail-end, excited molecules. Alternatively, the leading edge of unexcited molecules could form a "high" pressure cloud in front of the SEELEM surface which would cause the incoming metastable molecules to be scattered out of the beam.

A decline of SEELEM efficiency as a function of laser-nozzle delay was observed in the first-generation apparatus and is diagnostic of background pressure impacting the SEELEM detectivity. However, in the second-generation apparatus, changing the laser-nozzle delay by as much as 12 μs, which corresponds to a time window dur-

---

[2] Over time, the electron multiplier dynodes rapidly become contaminated and the gain coefficient for the ejected SEELEM electrons is reduced. Therefore, the electron multipliers are replaced approximately every six months.

ing which the molecular beam travels 1.9 cm, did not detectably alter the intensity profile of the SEELEM spectra [3] (Fig. 4-5). This shows that the pumping in the second-generation apparatus minimizes the build-up of potential adsorbates or "scatterers" in front of the SEELEM surface, thus keeping the SEELEM surface clean for the incoming flux of excited molecules. The laser-nozzle delay test proves that the superiority of the second-generation chamber at detecting the $T_{1,2}$ character of the molecular eigenstates is indeed a direct consequence of the improved background pressure and the cleaner SEELEM surface.

The survey spectra of Fig. 4-4 clearly show that the relative intensities of the SEELEM spectra acquired on Au and Cs are profoundly different. This demonstrates conclusively that, under improved vacuum conditions, the short-range detection pathway approaches its expected efficiency, making possible direct detection of the $T_{1,2}$ character in the molecular eigenstates. The signal level on the Cs surface is also a factor of 500 greater as compared to that acquired on the Y surface (or a factor of 1500 as compared to that acquired on Au). According to Drabbels *et al.*, the vibrational density of states of the T_1 surface at the energy of the transition being recorded in these experiments is about $10/\text{cm}^{-1}$ [35], which is a factor of about 1000 larger than the density of T_3 states (0.01 / cm^{-1}) in this energy region. Therefore, the expected enhancement in SEELEM signal should be about 1000-fold upon switching to a metal sensitive to the $T_{1,2}$ character of the molecular eigenstates. This is in agreement with observations.

4.4 Future Experiments

The enormous change in the efficiency of the short-range channel achieved by reducing the background pressure confirms our model for SEELEM detectivity and opens

---

[3] There is an upper limit to how much the laser-nozzle delay can be increased without changing the total number of excited molecules significantly. The laser induced fluorescence was monitored in each case in this experiment to ensure that the same number of molecules were being excited. The data shown in Fig. 5 were acquired with a brand new electron multiplier and, hence, are characterized by larger number of counts / laser shot than the survey spectra.

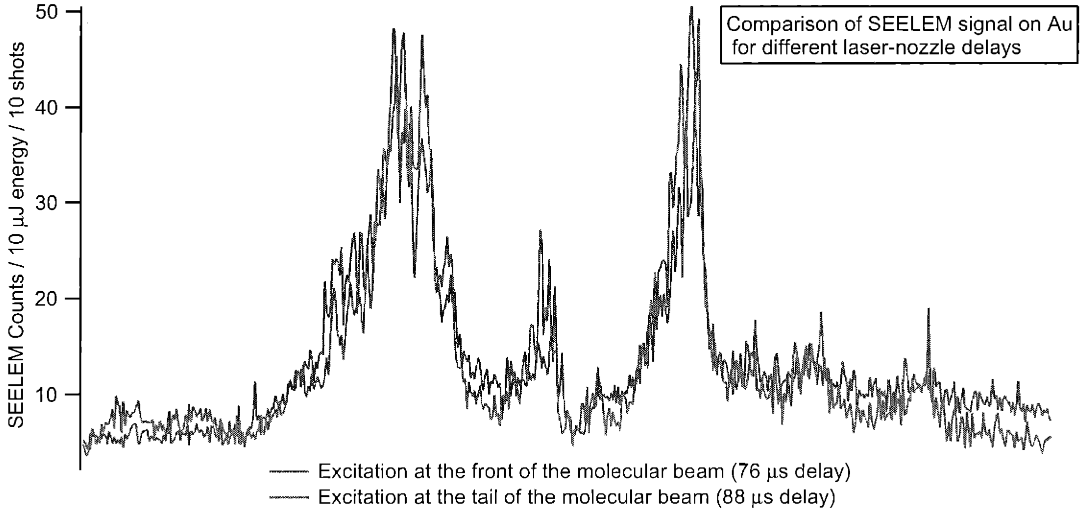

Figure 4-5: SEELEM spectra of a section of the $\tilde{A} \leftarrow \tilde{X}$ $V_0^3 K_0^1$ band of acetylene centered near 220.74 acquired on Au in the second-generation chamber where the operating base pressure was $4 * 10^{-7}$ Torr with two different laser-nozzle delays: 76 μs and 88μs. The lack of detectable differences between the two spectra indicates that there is no significant build-up of acetylene molecules on or in front of the SEELEM surface during the detection process. The shorter laser-nozzle delay corresponds to exciting the molecular pulse at the front end such that the excited molecules impact the SEELEM surface first. The longer laser-nozzle delay corresponds to exciting the tail-end of the molecular pulse so that the excited molecules impact the SEELEM surface after the unexcited molecules in the front part of the pulse. If the unexcited molecules in the leading edge are not pumped away fast enough, they may adsorb to the SEELEM surface or form a scattering cloud and reduce the detectivity of the excited molecules arriving in the tail-end of the molecular pulse.

up the possibility of recording direct triplet excitation spectra as well as directly measuring the S_1, T_3 and $T_{1,2}$ characters in metastable eigenstates.

Zwier and co-workers have determined a peak absorption cross section of $2.7 * 10^{-5}$ atm^{-1} cm^{-1} for the direct triplet - singlet ($^3\Delta_u \leftarrow ^1 \Sigma_g^+$) transition in C_4H_2 using cavity ringdown spectroscopy [52]. They report that this transition is $3 * 10^6$ times weaker than the strongest transition of C_4H_2, which is the $^1\Delta_u \leftarrow ^1 \Sigma_u^+$ transition. Although this suggests that the corresponding triplet - singlet transition in acetylene should also be exceedingly difficult to observe directly, we believe that the demonstrated sensitivity of SEELEM with Cs as the detection surface could make it possible to detect direct excitations to T_1, T_2, and T_3 states at energies far from resonance with S_1 vibrational levels.

We estimate the expected SEELEM signal level on Cs that would result from exciting a direct $T_1 \leftarrow S_o$ transition in C_2H_2. As shown in Eq. (5.6), the SEELEM signal arises from the contributions of three multiplicative factors: the excitation probability, the survival probability, and the detectivity. One can calculate the magnitudes of each of these factors for the case of the $S_1 \leftarrow S_o$ transition of acetylene detected on Au and compare the result to the expected magnitudes of the same factors for the case of the $T_1 \leftarrow S_o$ transition detected on Cs. Since we know the signal levels achieved when Au is used as the SEELEM surface, we can predict how difficult it would be to observe the forbidden transition in acetylene using Cs as the detector surface.

We have measured the lifetimes of the SEELEM states we observe on Au that arise from the excitation of the $S_1 \leftarrow S_o$ transition of acetylene. Based on these data, the S_1 fractional bright state character of the SEELEM states observed on Au is ~ 0.005. The T_3 character of these SEELEM states, which is the only other electronic state character that can give rise to signal on Au, is more difficult to calculate. However, one can estimate the T_3 character by making use of the known density of states that belong to different electronic states in the energy region of the $S_1 \leftarrow S_o$ transition and the couplings between these levels:

$$\begin{aligned} S_1 &= 0.01/\mathrm{cm}^{-1} \\ T_3 &= 0.01/\mathrm{cm}^{-1} \\ T_{1,2} &= 10/\mathrm{cm}^{-1} \\ S_o &= 1000/\mathrm{cm}^{-1} \end{aligned} \tag{4.2}$$

The interactions between acetylene electronic states may be ordered according to their strengths: $S_o \sim S_1 \ll S_o \sim T \ll S_1 \sim T \ll T_i \sim T_i$ [42]. Therefore, the T_3 character will *not* be distributed democratically over all the states in this energy region. In fact, we have some results which suggest that the eigenstates observed in our experiments possess very little, if any, S_0 character: the SEELEM spectrum in the region of the $4\nu_3$ level of S_1, where ν_3 is the *trans*-bending mode, shows no sign of predissociation even though the S_0 surface is unbound at this energy. Therefore, it can be concluded that T_3 character fractionates predominantly into $T_{1,2}$ states. In this case, one would expect the average T_3 character of an eigenstate to be $\frac{0.01}{10}$ or 10^{-3}. Using these numbers, one can determine that the SEELEM signal on Au for eigenstate transitions near resonant with the $S_1 \leftarrow S_o\ V_0^3 K_0^1$ band will be proportional to:

$$I_{Au}^{SEELEM} = 0.005 \times \left[e^{-\frac{\triangle t}{0.27\mu s} \times 0.005}\right] \times (\sqrt{0.005} + \sqrt{10^{-3}})^2 = 5 \times 10^{-5} \times e^{-\frac{\triangle t}{0.27\mu s}} \tag{4.3}$$

For the purposes of this calculation, 'α' (Eq. 5.6) is assumed to be unity.

A similar analysis can be carried out for the case of direct $T_1 \leftarrow S_o$ excitation detected on Cs. The first factor, which is the excitation probability, will be proportional to the minuscule S_1 fractional bright state character acquired through spin-orbit mixing with the energetically remote S_1 state. The nature of the spin-orbit interaction that couples states of different multiplicity is discussed by El-Sayed [44]. The magnitude of the $S_1 \sim T_1$ spin-orbit coupling in C_2H_2 has been calculated as 1.6 cm^{-1} by Cui *et al.* [27]. This is to be contrasted with the 13.7 cm^{-1} calculated coupling between S_1 and T_3 [27]. The transition probability for a nominally triplet state, ν_t, can be calculated as follows:

$$
\begin{aligned}
| < \nu_x|\mu|\nu_t > |^2 &= | < \nu_x|\mu|(|\nu_t^o > + H_{el} \sum_{\nu_s^o} \frac{< \nu_s^o|\nu_t^o >}{E_{\nu_t^o} - E_{\nu_s^o}} |\nu_s^o >)|^2 \\
&\cong | < \nu_x|\mu|(\frac{H_{el}}{E_T - E_S} \sum_{\nu_s^o} < \nu_s^o|\nu_t^o > |\nu_s^o >)|^2 \\
&= \frac{H_{el}^2 \mu_{sx}^2}{(E_T - E_S)^2} (\sum_{\nu_s^o} < \nu_x|\nu_s^o >< \nu_s^o|\nu_t^o >)^2 \\
&= \frac{H_{el}^2}{(E_T - E_S)^2} \mu_{sx}^2 q_{\nu_t^o \nu_x} \qquad (4.7)
\end{aligned}
$$

In the above equation "H_{el}" denotes the electronic part of the spin-orbit coupling matrix element between S_1 and T_1, which is the quantity calculated by Cui *et al.* [27]. ν_x is the initial vibrational state of S_0. The vibrationally excited S_0 states were not included in the expansion of the nominally triplet eigenstate, ν_t, since the coupling between S_0 and T is predicted to be much weaker than that between S_1 and T [42]. The dependence of the denominator of the perturbation theoretic expansion of $|\nu_t >$ on the vibrational levels of S_1 was also ignored for simplicity. The energy denominator was factored out of the summation expression and completeness was used to collapse the sum over ν_s^o to yield a (ν_t^o, ν_x) vibrational overlap factor. The S_1 *trans* minimum lies at 45301 cm^{-1} [35] and the T_1 *trans* minimum lies at 39360 cm^{-1} [134]. The fractional S_1 bright state character of the eigenstate ν_t is then given by:

$$
\begin{aligned}
| < \nu_x|\mu|\nu_t > |^2 &= C_{S_1}^2 \times \mu_{sx}^2 \times q_{\nu_t^o \nu_x} \\
C_{S_1}^2 &\cong \frac{H_{el}^2}{(E_T - E_S)^2} \\
C_{S_1}^2 &\cong \frac{1.6^2}{5941^2} \qquad (4.10)
\end{aligned}
$$

The fractional S_1 character in ν_t is $7.3 * 10^{-8}$. However, there is one more parameter to consider in order to properly evaluate the strength of the $T_1 \leftarrow S_0(\nu = 0)$ transition with respect to that of the $S_1(\nu_3 = 3) \leftarrow S_0(\nu = 0)$ transition: Watson's calculations of the vibrational intensities in the $\tilde{A} - \tilde{X}$ electronic transition of acetylene show that the vibrational overlap factor for the $\nu_3^{'} - 0$ progression increases rapidly with increasing number of quanta of excitation in the upper state up to a maximum increase of a factor of 300 relative to the $1\nu_3' - 0$ band [145]. This trend can be expected to occur in the T_1 electronic state as well since, according to *ab initio* calculations, the shapes of the S_1 and T_i potential surfaces resemble each other [105].

Therefore, the vibrational overlap factor in the intensity expression for the $T_1 \leftarrow S_0(\nu = 0)$ transition can be increased by at least a factor of 10 relative to the vibrational overlap factor for the $S_1(\nu_3 = 3) \leftarrow S_0(\nu = 0)$ transition by targeting high vibrational levels ($\nu \geq 5$) of the T_1 surface.

The detectivity term in the SEELEM expression in the case of direct T - S excitation will be estimated as 1 since this is approximately the average fractional triplet state character acquired by an eigenstate in the energy region of the direct T - S transition. Fractionation of the triplet character over S_0 states is again assumed to be negligible [42].

Evaluating the SEELEM expression for the direct T - S excitation case, one finds that the SEELEM signal on Cs will be proportional to:

$$I_{Cs}^{SEELEM} = (\frac{1.6cm^{-1}}{5941cm^{-1}})^2 \times \left[e^{-\frac{\triangle t}{0.27\mu s} \times 7.3\times 10^{-8}}\right] \times 1 \times 10 = 7.3 \times 10^{-7} \times e^{-\frac{\triangle t}{0.27\mu s}}, \quad (4.11)$$

where the last factor of 10 is the vibrational overlap enhancement factor for the Franck-Condon strong $T_1 \leftarrow S_0(\nu = 0)$ transition relative to the $S_1(\nu_3 = 3) \leftarrow S_0(\nu = 0)$ transition.

The important parameters which determine the strength of the signal from the $T_n \leftarrow S_0(\nu = 0)$ transition detected on Cs as compared to the signal from the $S_1(\nu_3 = 3) \leftarrow S_0(\nu = 0)$ transition detected on Au, are summarized below:

SEELEM metal	*Au*	*Cs*
Fractional S$_1$ character	0.005	$7.3 * 10^{-8}$
Detectivity	$(\sqrt{0.005} + \sqrt{10^{-3}})^2$	1
Franck-Condon enhancement	1	10
Signal level	$5 * 10^{-5}$	$7.3 * 10^{-7}$
Signal level normalized with respect to Cs	70	1

The intensity of the $T_1 \leftarrow S_0(\nu = 0)$ transition is estimated to be a factor of 70 weaker than that of the $S_1(\nu_3 = 3) \leftarrow S_0(\nu = 0)$ transition. The *optimized* signal from S_1 $3\nu_3$ acquired on Au is typically 10 counts/shot/100 μJ of laser light. We have detected weaker signals on Au. These were axis-switching transitions and their intensity was about 0.2 counts/shot/100 μJ of laser light. Although it is possible to observe signal on Au which is a factor of 50 smaller than the "reference" S_1 $3\nu_3$ signal, the S/N ratio associated with the Cs surface is much poorer than the one associated with Au and, therefore, it could be difficult to detect on Cs signal which is a factor of 70 weaker than the reference S_1 $3\nu_3$ signal. However, it is possible to improve the S/N ratio on Cs by increasing data collection time, decreasing the background pressure in the chamber, and by suppressing ejection of "thermionic" electrons from the Cs surface. The background pressure in the chamber could be improved by subjecting the chamber to an extensive pumping cycle. The ejection of thermal electrons from the Cs surface could be suppressed by cooling the Cs surface. Alternatively, one could choose to improve the S/N ratio by increasing the signal level. This could be achieved by increasing the laser intensity or the concentration of acetylene in the molecular beam.

Another challenge associated with recording direct T - S excitation spectra is distinguishing these forbidden transitions from others such as hot band transitions. One signature of T - S transitions will be absence of detectable fluorescence signal. However, there is another way to determine whether a certain signal arises from a T - S transition or a hot band $S_1 \leftarrow S_0$ transition: We have shown that Ar as a

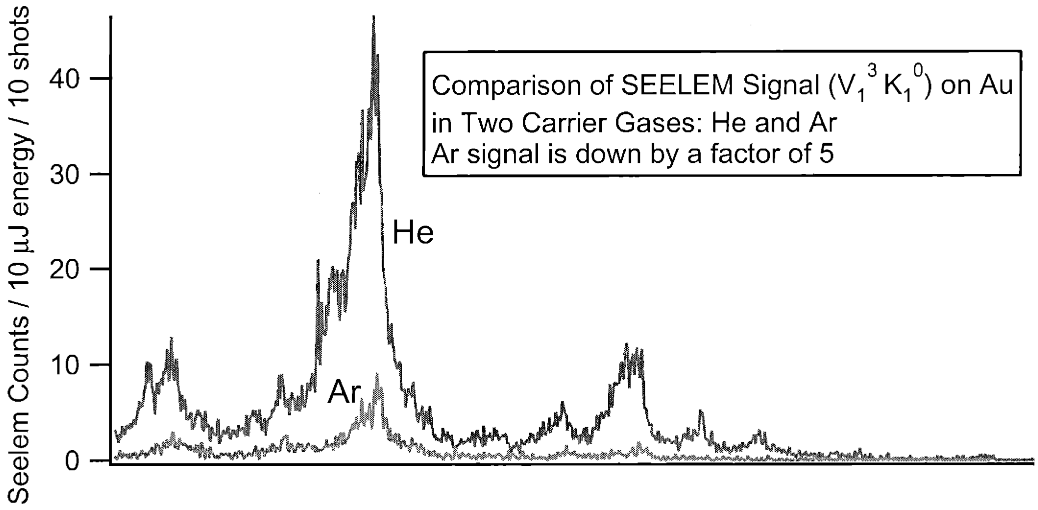

Figure 4-6: SEELEM spectra of a hot band transition ($V_1^3K_1^0$) of C_2H_2 acquired on Au in the second-generation apparatus: The molecules were seeded in Ar and He. Ar is much more efficient at vibrational cooling, hence the reduction in signal due to the reduction of population in the ground state in the case of Ar as the carrier gas. The efficiency of Ar at vibrational cooling could be exploited to distinguish hot band transitions from other weak, cold band transitions, such as direct $T \leftarrow S_0$ excitations.

carrier gas is very efficient at vibrational cooling. He, on the other hand, was shown to be efficient only at rotational cooling. We have recorded two spectra of the $V_1^3K_1^0$ transition of acetylene ($S_1 \leftarrow S_{0(hot)}$) using He and Ar as the carrier gases (Fig. 4-6). As the spectra show, the signal level goes down by a factor of 5 due to vibrational cooling when Ar is used as the carrier gas. Therefore, in order to distinguish hot band transitions from transitions originating from $\nu = 0$, one would compare spectra recorded with Ar and He carrier gas.

There are some results from electron-energy loss studies which predict the energies of the strongest vibrational bands for the $T \leftarrow S_0$ transitions of C_2H_2 [134, 146, 148, 55]. Guided by these predictions, we expect to be able to record $T \leftarrow S_0$ SEELEM excitation spectra of acetylene. This experiment is in fact ongoing as this thesis is being written.

4.5 Conclusion

We have demonstrated the profoundly different effects of detector surface contamination on S_1 vs. T detectivity in Surface Electron Ejection by Laser Excited Metastables (SEELEM) spectroscopy. SEELEM is a powerful technique that has been used to study the triplet states of molecules. It involves emission of electrons from metal surfaces upon impact by excited metastable species. The efficiency of the SEELEM process depends critically on the background pressure. The de-excitation of a mixed molecular eigenstate upon impact with a SEELEM surface can proceed through two pathways, known as the short-range and long-range interaction pathways. The triplet character of the eigenstates de-excites exclusively through the short-range interaction pathway. This pathway is very sensitive to the cleanliness of the SEELEM surface. At high background pressures, the short-range interaction pathway is shut down, leading to very inefficient detection of the triplet character relative to the singlet character of the eigenstates. We have shown that, by improving the vacuum conditions, one drastically alters the efficiency of the SEELEM process and enhances the triplet-detection channel.

This is the first step in constructing a mechanistic picture of the SEELEM detection process. The dependence of detectivity both on extrinsic (background pressure) and intrinsic (electronic state composition of the metastable eigenstates) parameters needs to be explicitly considered in the interpretion of the SEELEM spectra to draw accurate conclusions about the fundamental intramolecular energy re-distribution processes that give rise to the metastable states being detected.

The next barrier that must be overcome before dynamically meaningful spectra can be obtained is spectral resolution. We hope to achieve a factor of 20 higher resolution than the present 0.08 cm^{-1} in our next phase experiments. Higher resolution spectra will allow us to effectively use the analytical tools we have developed [5, 6] to uncover the mechanism governing the redistribution of energy in our model system.

Chapter 5

Retrieving Electronic Coupling Mechanisms Underlying Complex Spectra I - A Statistical Approach

Chapters 5 and 6 will outline two approaches that were developed to obtain qualitative and quantitative insights into the mechanism of singlet-triplet coupling in small polyatomic molecules. The first approach is based on a statistical analysis technique which makes use of both SEELEM and LIF spectra. In this approach the trends in spectral signatures, such as fractionation patterns and intensity-weighted average energies, as a function of the rotational quantum number J are correlated with specific electronic coupling schemes. The second approach is an "unintended" application of the Lawrance-Knight deconvolution procedure and makes use of LIF spectra only. The nature of a particular singlet-triplet electronic coupling and certain quantitative parameters governing this singlet-triplet interaction can be deduced using this approach.

5.1 Introduction

Intersystem Crossing (ISC) is conventionally described by a standard, statistical bright-state → dark-state Fermi's Golden Rule decay process [14, 9] by which the singlet (S_1) character of the initially prepared non-eigenstate decays at a rate proportional to the product of i) the average square modulus of the spin-orbit (SO) matrix element between the S_1 state and the isoenergetic dark states, and ii) the density of the dark states at the energy of the S_1 state [85](Eq. 5.1).

$$k_{ISC} = \frac{2\pi}{\hbar^2} | < f|\hat{H_{SO}}|i > \rho(E) \tag{5.1}$$

However, the possibility exists that the mechanism underlying this nonradiative decay process could exhibit greater mode specificity or "causality" than the standard statistical picture. In particular, the process could be "mediated" by a specifiable "doorway" state which uniquely facilitates the coupling of the bright state to the background of dark states.

This chapter addresses the question of whether it is possible to assess from experimental spectra whether ISC in a certain molecular system exhibits a mechanistic pattern which goes beyond a Fermi's Golden Rule statistical model. It will describe and explain the physical basis for the effectiveness of several diagnostic tools, which are extensively tested on synthetic spectra simulated based on what is already known about the acetylene S_1 $3\nu_3$ level and its interaction with the $T_3, T_{2,1}$ and S_o vibrational levels. Acetylene is a good model system for this study because its spectra are, in principle, resolvable owing to the relatively low density of $T_{1,2}$ vibrational states in the energy region of the S_1 $3\nu_3$ level ($\sim 10/\,\mathrm{cm}^{-1}$)[35]. The analytical tools discussed here are capable of (i) revealing whether a system follows the standard, statistical bright-state → dark-state *direct* decay mechanism or, instead, follows a deterministic *doorway-mediated* mechanism; (ii) and determining critical properties of the doorway vibrational state, such as its effective rotational constant, and its coupling matrix element to S_1.

5.2 A Statistical Approach for the Singlet-Triplet Interactions in Small Polyatomic Molecules

Development of effective analytical tools by which LIF and SEELEM spectra can be analyzed is a first step towards understanding the details of ISC in small molecules and obtaining information about the mechanism and strength of the coupling between the S_1 bright state and the background triplet states. The LIF and SEELEM spectra sample complementary sets of molecular eigenstates. The usual, but prohibitively difficult, way that a spectroscopist would approach these LIF and SEELEM spectra, is to put vibrational and electronic quantum labels on the individual eigenstates. The point of this section is that it will be sufficient to describe the spectra as a statistical ensemble of eigenstates which obey specific rules. The properties of this statistical ensemble, such as its energy and intensity distribution, are dependent on the specific coupling scheme that mixes the bright state with the dark states. The statistical measures discussed here are shown to be potentially capable of recovering qualitative and quantitative details of this coupling without resorting to the prohibitive difficulty of a fit of eigenstates to an H^{eff} matrix model.

Two opposite limit coupling schemes are *direct* and *doorway-mediated* coupling. To reveal the unique spectral signatures of these two coupling schemes and to extract information about the triplet perturbers, such as their density of vibrational states and their average coupling matrix element to the S_1 bright state, a series of LIF and SEELEM spectra were simulated. Several statistical measures were found to differentiate decisively between spectra that resulted from a *direct* coupling model and spectra that resulted from a *doorway-mediated* model. The details of these simulations will be described next. We will also explain, using Perturbation Theory, the physical basis for the diagnostically valuable features of each statistical measure.

5.2.1 Computational Details

The two coupling models that are compared and contrasted in this section differ in two points: i)the strength of the coupling between the bright state S_1 and one of the dark states, labelled as T_3 (*i.e.* the magnitude of the off-diagonal matrix element between S_1 and T_3); ii)whether S_1 is allowed to couple directly to all the background states rather than exclusively to the single T_3 state (the background states other than T_3 will be referred to as T_i). The T_3 state is allowed to couple to all of the background states in both models. In the *direct* model, the coupling between S_1 and T_3 is chosen to have the same strength as that between S_1 and T_i. In the *doorway-mediated* model, S_1 is only allowed to couple to T_3, the doorway state, which in turn couples to the other background states, T_i. The T_3 density of states is assumed to be very low in the energy region of S_1 $3\nu_3$, therefore only one T_3 state is included in the manifold of triplet states which consists of about 200 states and spans an energy region of approximately 20 cm^{-1}(this density of triplet states was chosen to be in agreement with Drabbels' experimental results, which indicate a density of dark states on the order of $10/\text{cm}^{-1}$[35]). In the *doorway-mediated* case, the coupling between S_1 and T_3 is about an order of magnitude stronger than the coupling between T_3 and T_i (*i.e.* the off-diagonal matrix element between S_1 and T_3 is ten times bigger than the mean of the absolute values of the off-diagonal matrix elements between T_3 and each of the T_i states).

The parameters that define each model are the various coupling strengths and the densities of states involved. In the *direct* model, one needs to specify the distribution of coupling strengths between S_1 and the background states, among which the arbitrarily labelled T_3 state is included. One also needs to specify the coupling strength distribution between the T_3 state and the other background states, *i.e.* the $T_3 \sim T_i$ coupling. In the *doorway-mediated* model, one needs to specify one $S_1 \sim T_3$ coupling strength *and* the $T_3 \sim T_i$ coupling strength distribution. The $T_3 \sim T_i$ coupling strength distribution is chosen to be identical in both models[1].

---

[1] The rationale behind allowing only T_3 to interact with the rest of the background states (vibrational levels of the T_1 surface) while not allowing any interaction among the background states

5.2.2 Constructing the Hamiltonian Matrices

All of the simulations are performed using **Matlab**, a matrix-based mathematics package. Two sets of synthetic LIF and SEELEM spectra are produced based on the two coupling schemes: *direct* and *doorway-mediated.* In the formulation of the *direct* model, S_1 is coupled directly to a manifold of 212 triplet states placed at random intervals over an energy region of 21 cm^{-1}, centered at the energy of the S_1 $3\nu_3$ state. Of the 212 vibrational states in the triplet manifold, one state is arbitrarily labelled as a T_3 electronic state. This state is allowed to couple to each of the other dark states in the manifold. The number of background states is fixed at 212 because this number has been found to be not so large as to be computationally cumbersome and not so small as to lead to artificial "edge effects" in the simulations. The edge effects are avoided by making sure that there is always a sufficient number of T_i states at both lower and higher energies relative to the energy of the T_3 state. (What constitutes a "sufficient" number is determined by the fractionation envelope of T_3, and anything more than 5 eigenstates within the fractionation envelope is considered sufficient).

The coupling matrix elements between S_1 and each of the triplet states in the manifold are randomly selected from a normal distribution with mean 0.0 and variance 0.05 cm^{-1}. The *mean of the absolute values* of these matrix elements is 0.04 cm^{-1} (from this point on, the term "average strength" will signify the mean of the absolute values of the matrix elements). The choice of 0.04 cm^{-1} as the average bright ↔ dark matrix element is based on the experimental results of Drabbels *et al.*[35]. In applying the standard Lawrance-Knight deconvolution procedure [12, 83, 88, 82] to an ultrahigh resolution (18 MHz) LIF spectrum, Drabbels *et al.* deduced an average coupling strength of 0.04 cm^{-1}. The density of the dark states chosen for the present calculation is that observed in the high resolution spectra of Drabbels (~10 states / cm^{-1}).

The average strength of the coupling between T_3 and the other dark states is set at 0.2 cm^{-1} in *both models.* This choice is not based on any theoretical finding. Al-

---

themselves is that one could always choose initially to pre-diagonalize the background states.

though there have been a few experimental [137, 148, 146] and a number of theoretical publications [24, 27, 147, 90, 77, 31, 149, 151] reporting the geometries, harmonic vibrational frequencies, and dipole moments of the first two low-lying triplet electronic states (*i.e.* T_1, T_2) of acetylene, little is known about the properties of the T_3 state [24, 27]. This is in contrast to the wealth of literature that exists concerning the *trans* $\tilde{A}\,{}^1A_u$ first excited singlet state [16, 51, 142, 66, 54, 65] and the ${}^1\Sigma_g^+$ ground electronic state [69, 87, 18, 60, 100, 59, 150, 81, 50, 98, 109, 67, 115] of acetylene.

In their paper describing results from ZQB experiments, Dupré *et al.* order the interactions between acetylene electronic states according to their strengths [43]. In their list, background triplet $\sim$ background triplet interactions are stronger than singlet $\sim$ background triplet interactions. In the absence of other definitive data, the coupling strength parameters have been defined in accordance with Dupré's list for the simulations described in this paper. The particular value of 0.2 cm^{-1} as the $T_3 \sim T_i$ coupling strength is a reasonable choice because the widths of the peaks in the SEELEM spectra are expected to be governed largely by the $T_3 \sim T_i$ coupling strength, since this is the final tier of coupling that eventually mixes S_1 with the background triplet states. The widths of the clusters of peaks in our preliminary SEELEM spectra are around 1 cm^{-1}. This number is very close to what Fermi's Golden Rule predicts (*i.e.* 1.25 cm^{-1}) for a statistical coupling case where the density of dark states is $10/\,\text{cm}^{-1}$ and the coupling strength between the single bright state and the dark manifold is 0.2 cm^{-1}. Choosing 0.2 cm^{-1} as the $T_3 \sim T_i$ coupling strength also results in an approximately Lorentzian fractionation profile of the T_3 character following matrix diagonalization.

In the *doorway model* it is assumed that there is no direct coupling between S_1 and the dark background manifold and that T_3 is a special state that mediates the interaction between the bright state, S_1, and the manifold of dark states. The key in redefining the parameters of the *direct model* so as to transform it into a *doorway-mediated model* is to preserve the "effective" strength of the $S_1 \sim$ background coupling, while slightly modifying its nature (by "effective", we mean the average strength of the indirect coupling of S_1 to the background states). It is thus necessary to choose appropriate coupling strengths for the $S_1 \sim T_3$ and the $T_3 \sim T_i$ interactions. Setting the magnitude of the $S_1 \sim T_3$ coupling to 0.3 cm^{-1} and that of the $T_3 \sim T_i$ coupling to 0.2 cm^{-1} yields an effective coupling strength of 0.05 cm^{-1} between S_1 and the background states^4. This number is sufficiently close to the target number of 0.04 cm^{-1} for the purposes of these simulations. The calculation of the effective $S_1 \sim$ background triplet coupling is described below.

A sub-matrix, consisting only of the triplet basis states is constructed where the average coupling strength between the single T_3 state and the 211 background triplet states is 0.2 cm^{-1}. The effective coupling strength between S_1 and one specific pre-diagonalized triplet state is calculated as follows. K_i below denotes a prediagonalized triplet state and c_j^i denotes the mixing coefficient in front of the j^{th} triplet basis state in the expansion of the i^{th} pre-diagonalized state:

$$< S_1|\hat{H}|K_i > = < S_1|\hat{H}|c_3^i T_3 + c_1^i T_1 + c_2^i T_2 + c_4^i T_4 + \ldots > \tag{5.2}$$

which reduces to a single non-zero term,

$$c_3^i < S_1|\hat{H}|T_3 > \tag{5.3}$$

because the direct $S_1 \sim T_{1,2,4...}$ coupling matrix elements are assumed to be zero in the *doorway* model.

As described above, when the $S_1 \sim T_3$ spin-orbit matrix element represented by $< S_1|\hat{H}|T_3 >$ is chosen to be 0.3 cm^{-1}, the average effective coupling strength has the desired value of 0.05 cm^{-1}. Thus,

$$\overline{|c_3|} < S_1|\hat{H}|T_3 > = \; 0.05\,\mathrm{cm}^{-1} \tag{5.4}$$

where $\overline{|c_3|} \; = \; 0.17$.

Once the Hamiltonian matrices for the two models are constructed, they are diagonalized to yield the eigenstates and eigenenergies used to generate the synthetic LIF and SEELEM spectra.

5.2.3 Intensities In the Synthetic Spectra

The parameters used in this subsection in the computation of spectral intensities reflect the experimental conditions of the first-generation apparatus which was in operation at the time the statistical measures discussed here were developed. The intensities in the simulated LIF spectra are computed from the S_1 character in each eigenstate using Eq. (5.5) below [68]. As reflected in Eq. (5.5), the LIF intensity in a typical experiment is directly proportional to the fractional bright state character of the eigenstate (the excitation probability) and an explicit function of the finite time window, $t_1 \leq t \leq t_2$, over which fluorescence is collected.

$$I_i^{LIF} = C_{S_1}^2 \times \left[e^{-R_1 \times C_{S_1}^2} - e^{-R_2 \times C_{S_1}^2} \right] \tag{5.5}$$

where $R_1 = \frac{100ns}{270ns}$ and $R_2 = \frac{5100ns}{270ns}$. In our experiments in the first-generation apparatus, the detection gate opened 100 ns after the UV laser pulse and closed 5100 ns after. The closing of the detection gate is determined by the transit time of the excited molecules through the field of view. 270 ns is the intrinsic lifetime of a pure singlet state [68]. The eigenstates excited in our experiment decay at the decay rate of a pure singlet state reduced by the fractional S_1 character, $C_{S_1}^2$ of the particular eigenstate.

A corresponding expression, Eq. (5.6), for the intensities in the SEELEM spectrum is more complicated [68].

$$I_i^{SEELEM} = C_{S_1}^2 \times \left[e^{-R_m \times C_{S_1}^2} \right] \times (C_{S_1} + \alpha\, C_{T_3})^2 \tag{5.6}$$

where $R_m = \frac{140\mu s}{0.27\mu s}$. The relevant factors are the excitation probability (the fractional bright state character of each eigenstate); the probability of surviving the $\sim 140\mu s$ flight time from excitation to impact on the detector, which is also determined by the fractional S_1 character; and the detectivity, which is related to the amplitudes of those basis states that lie above the 5.1 eV work function of gold, in this case, exclusively the S_1 and T_3 basis states.

Because S_1 and T_3 belong to different electronic surfaces, their SEELEM detectivities are not expected to be identical. Therefore, a scaling factor 'α' was inserted into the detectivity factor of the SEELEM expression. A more detailed discussion about the origin of α is presented in Chapter 4. The value of this scaling factor is set to 0.01, implying that the singlet amplitude of an eigenstate is 100 times more detectable than its triplet amplitude. The crude vacuum conditions in the first-generation apparatus significantly hindered the SEELEM detection process for the triplet character of the eigenstates as discussed in Chapter 4, and therefore, caused a large difference between the SEELEM detectivities of fractional S_1 and T_3 characters of an eigenstate.

Since at the time the statistical measures were developed, we had not yet conducted the lifetime studies discussed in Chapter 3 on the S_1 $3\nu_3$ states of acetylene, we estimated the lifetimes of the mixed states by the available information at the time. In the time-of-flight spectra acquired in the first-generation apparatus, we had observed a broad (80-160 μs) pulse of metastable acetylene molecules arriving at the SEELEM detector centered around 140 μs after the laser shot. This implies that the lifetime of a typical mixed state detected in our first experiments could not have been significantly shorter than 140 μs. Wodtke *et al.* report, from experiments also directed at the metastable states of acetylene, the average radiative lifetime of the metastable states excited via the S_1 $3\nu_3$ level, as 110±40 μs [68]. According to another experiment by Suzuki *et al.* which involves detection of a sensitized phosphorescence signal from metastable species, the lifetimes of triplet acetylene states produced by ISC from V^3K^1 are around 100±50 μs [133]. Therefore, we selected the lifetime of a typical metastable mixed state detected in our SEELEM experiment to be 140 μs in the SEELEM intensity expression.

The detectivity term in the above SEELEM expression, $(C_{S_1} + \alpha\ C_{T_3})^2$, leads to interference effects which explain some of the features observed in preliminary SEELEM spectra [68]. Interference effects are evident when the zeroth order S_1 and T_3 term value plots cross (even if $\alpha = 0$). At such a crossing, the quantity $E_{S_1} - E_{T_3}$ passes through zero (with concomitant sign change). In the case of *doorway-mediated* coupling, this quantity, in turn, determines the S_1 and T_3 basis state amplitudes acquired by an eigenstate (see Appendix I for a derivation of the expressions that give the S_1 and T_3 basis state amplitudes acquired by an eigenstate in the case of *doorway-mediated* coupling). Therefore, incorporating a term in the SEELEM expression which is dependent on both the S_1 and T_3 amplitudes of an eigenstate, both of which are signed quantities, allows interference effects to modulate the SEELEM signal in the case of *doorway-mediated* coupling. Such effects, depending on whether they are constructive or destructive, lead respectively to enhancement or reduction in the SEELEM intensities and to characteristic qualitative changes in intensity pattern as T_3 tunes through S_1.

A three dimensional plot of the SEELEM signal as a function of S_1 and T_3 basis state amplitudes is presented in Fig. 5-1a. The most important feature of the plot is the relative insensitivity of the SEELEM signal to the T_3 character, owing to our choice of the T_3/S_1 intensity scaling factor, $\alpha \cong 0.01$. It is the S_1 character that determines the strength of the SEELEM signal. The range of S_1 basis state amplitudes that leads to a detectable SEELEM signal is -0.12 to 0.12. A SEELEM signal is considered "detectable" if it is at least 0.05 of the maximum SEELEM signal. The amplitudes -0.12 and 0.12 correspond to a maximum S_1 fractional character of 0.014. Any eigenstate with S_1 character greater than this number is too short-lived to have a probability greater than 0.05 of surviving to hit the detector. It should be noted here that the plot in Fig. 5-1a was obtained with a particular choice of the α parameter ($\alpha = 0.01$). As α is increased towards 1, a quadratic dependence on the T_3 character emerges along the "ridges" of the surface of the SEELEM signal intensity. "Ridges" refer to the surface structures defined by the local maxima. When α is set to 1, the plot in Fig. 5-1b results. In that case, as expected, the SEELEM signal increases quadratically with increasing T_3 fractional character.

Another important feature of the plots in Fig. 5-1a and Fig. 5-1b is how the slope along the ridges indicates that the SEELEM signal intensity is different in each quadrant of the S_1, T_3 plane. This is a manifestation of the "interference" effects implicit in the SEELEM signal expression, as discussed previously. When the S_1 and T_3 basis state amplitudes have opposite signs (as in the first and third quadrants), the intensity of the SEELEM signal is diminished as a consequence of destructive

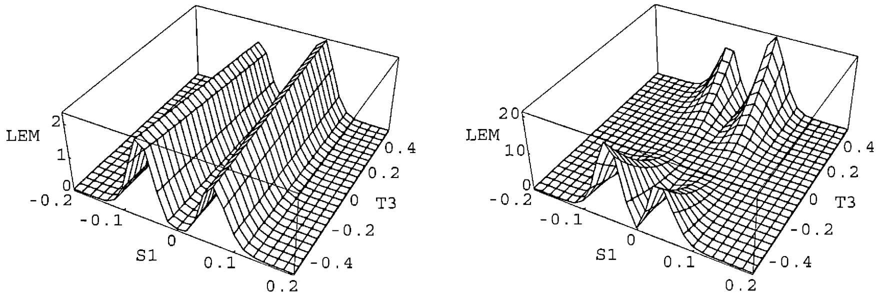

A ($\alpha = 0.01$) B ($\alpha = 1$)

Figure 5-1: The SEELEM signal as a function of the S_1 and T_3 mixing coefficients when the relative detectivities of the S_1 and T_3 characters of the eigenstates are, respectively, (i)1 : 0.01 (*i.e.* $\alpha = 0.01$, panel I) and (ii)1 : 1 (*i.e.* $\alpha = 1$, panel II).

interference, and when the S_1 and T_3 basis state amplitudes have the same sign (as in the second and fourth quadrants), the SEELEM signal is enhanced owing to constructive interference. Note that the interference effects remain even when $\alpha = 0.01$.

5.3 Results and Discussion

One useful way to analyze the synthetic spectra obtained from the calculations described in the previous subsection is to reduce them to statistical measures that are diagnostic of the underlying coupling scheme. Four statistical measures have useful diagnostic capabilities: 1) the intensity-weighted average energy (mean energy) of each spectrum; 2) the intensity-weighted skewness with respect to the mean energy; 3) the cross-correlation between the SEELEM and LIF spectra; 4) the fractionation parameter, which reflects the number and energy spread of eigenstates which have appreciable intensity in the LIF and SEELEM spectra. The definitions of these parameters are:

$$\textit{Mean Energy:} \quad E_{ave} = \sum_i I_i \times E_i \tag{5.7}$$

$$\textit{Intentisy Weighted Skewness:} \quad S = \sum_i I_i^2 \times [E_i - E_{ave}] \tag{5.8}$$

$$\textit{Correlation:} \quad C = \frac{\sum_i (LIF_i \times SEELEM_i)}{\sum_i LIF_i^2} \tag{5.9}$$

$$\textit{Fractionation:} \quad F = \sum_i I_i^2 \tag{5.10}$$

In Equations (5.7 - 5.10), I_i represents the normalized intensity of the transition into the i^{th} eigenstate; LIF_i and $SEELEM_i$ represent the artificially broadened lineshapes of transitions into the i^{th} eigenstate in the LIF and SEELEM spectra, respectively. In particular before calculating the correlation factor, it was necessary to degrade the resolution of the spectra from that sufficient to resolve all the eigenstates, because, in the eigenstate-resolved limit, the LIF and SEELEM spectra are almost "orthogonal", *i.e.* they sample nearly disjoint sets of eigenstates. Details about this resolution degradation procedure will be presented in Section 5.4.

The trends in these statistical measures are examined as a function of the energy of the single T_3 basis state relative to that of the S_1 basis state. Varying the T_3 energy relative to the S_1 energy in this simulation corresponds to sampling transitions associated with different values of J as one scans the laser excitation frequency through a vibronic band. Spin-orbit coupling, responsible for the $S_1 \sim T_3$ interaction, conserves J and has $J-$independent off-diagonal matrix elements. Since the members of the near degenerate pair of S_1 and T_3 vibrational levels probably have slightly different rotational constants (B), scanning the relative energies of the T_3 and S_1 basis states simulates the tuning of the J levels of the two states through the level-crossing at J_c where, by the definition of J_c, the energies of the basis states are equal. The T_3 position is varied freely without making any changes in the numerical formulation of

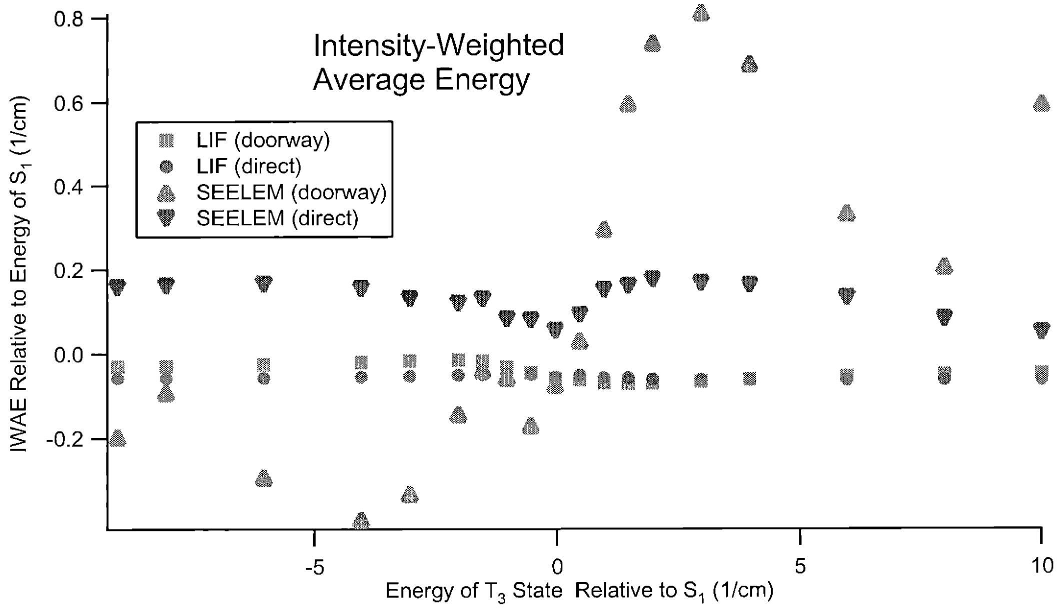

Figure 5-2: Intensity-weighted average energy (IWAE) of the simulated LIF and SEELEM spectra of acetylene for the *direct* and *doorway-mediated* coupling models.

the problem because, for spin-orbit coupling, the average interaction coupling matrix elements should not depend on J. Each time T_3 is moved to a new position with respect to S_1, a different randomly selected background state is moved an equal distance in the opposite direction so as to preserve the symmetry of the problem.

Figure 5-2 shows the variation in the intensity-weighted average energy of the SEELEM and LIF spectra that results from the two different coupling schemes, as a function of the T_3 energy. The mean energy in the LIF spectrum remains constant for *both models* as the energy of the T_3 basis state is varied and approximately tracks the energy of the S_1 basis state, which is defined to be at 0 cm^{-1}. On the other hand, the intensity-weighted mean energy in the SEELEM spectrum exhibits quite distinct behaviors as a function of the energy of the T_3 basis state for the *direct* vs. *doorway* coupling models. The characteristic shape of the intensity-weighted average energy curve for the *doorway* model SEELEM spectrum can be explained by using Perturbation Theory to examine the interactions between S_1, T_3, and the background states.

As pointed out previously, it is the S_1 character of the eigenstates that makes them SEELEM detectable. In the *doorway-mediated* coupling mechanism, eigenstates of dominant background state T_i character acquire their S_1 character through two pathways: by interacting with each of the two mixed states, M_1 and M_2, that arise from S_1 and T_3 basis states. Using general results from Perturbation Theory, an expression for the coefficient of S_1 character acquired by each background state, T_i, can be derived (the details of this derivation are shown in Appendix I). The final result of this derivation is presented below:

The S_1 amplitude acquired by a specific background state T_b is:

$$C_{S_1}^{b} = -\frac{sin(2\theta)}{2}\frac{< T_b|\hat{H}_{so}|T_3 >}{E_{T_b} - E_{M_1}} + \frac{sin(2\theta)}{2}\frac{< T_b|\hat{H}_{so}|T_3 >}{E_{T_b} - E_{M_2}} \tag{5.11}$$

where θ is the mixing angle between S_1 and T_3 and E_{M_1} and E_{M_2} are the energies of the mixed states that are of nominal S_1 and T_3 character respectively. E_{M_1} lies closer to E_{S_1} and E_{M_2} lies closer to E_{T_3}. $\hat{H}_{so}$ denotes the spin-orbit operator which gives rise to an off-diagonal matrix element between T_3 and the specific background state T_b. It should be recalled that T_3 couples directly to all of the background T_i states in both the *direct* and *doorway-mediated* models and the average strength of this coupling is 0.2 cm^{-1}.

The key point is that the two mixing coefficients in Eq.(5.11) have opposite signs, therefore, depending on the energy of T_b relative to M_1 (*i.e.* S_1) and M_2 (*i.e.* T_3), the terms multiplied by these coefficients would either add constructively or destructively. For a given energy of T_3, if the energy of the T_b state lies between those of S_1 and T_3, then constructive interference is expected. If the energy of the T_b state lies above that of S_1 or below that of T_3, then destructive interference results. These cases are depicted in Fig. 5-3.

The energy of S_1 is defined here as the midpoint of the T_i state energy range. When T_3 is degenerate with S_1, the S_1 character fractionates symmetrically over the T_i states, and hence, the resulting SEELEM spectrum has an intensity-weighted average energy that is the same as the energy of the S_1 basis state. If the T_3 state

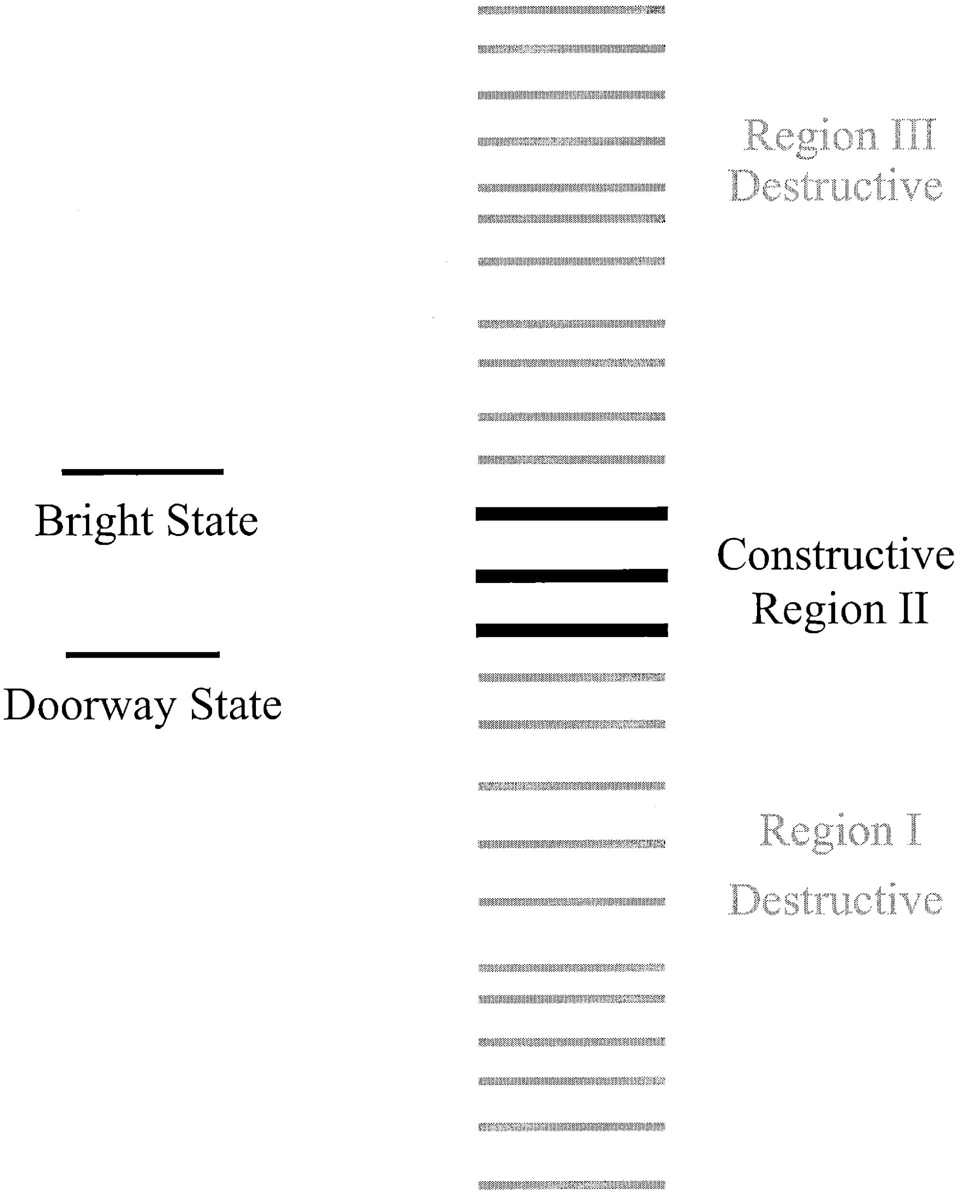

Figure 5-3: Regions of constructive and destructive interference in the dark manifold when the energy of the doorway state T_3 is to the red of that of the bright state S_1 in the *doorway-mediated* coupling model.

is shifted to the red of the S_1 state, then the T_i states that are in the "constructive interference" region acquire the most S_1 character and, hence, appear strongly in the SEELEM spectrum. Since the constructive interference region, where the most strongly SEELEM detectable T_i states reside, is necessarily to the red of S_1 when the energy of T_3 is below that of S_1 (Fig. 5-3), the intensity-weighted average energy of the SEELEM is shifted slightly to the red of the S_1 basis state energy. However, this asymmetry toward the red of S_1 cannot persist indefinitely as T_3 is moved farther and farther to the red. When the energy of T_3 is 5 cm^{-1} to the red of S_1, the intensity-weighted average energy starts to move back toward the energy of the S_1 basis state. This occurs because, when T_3 has moved sufficiently far to the red of S_1, the T_i states in region III can no longer acquire appreciable S_1 character through *both* pathways. One of the pathways, *i.e.* the one that involves interaction with the mixed state of predominant T_3 character, essentially shuts down because of the large energy gap between the T_i states in region III and the T_3 basis state. In the absence of two comparably important pathways that would have given rise to destructive interference, the T_i states in region III acquire sufficient S_1 character to be SEELEM detectable and, hence, shift the intensity-weighted average energy of the SEELEM spectrum back toward the blue. However, when the T_3 state lies 8 cm^{-1} to the red of the S_1 basis state, we see yet another change in the trend of the intensity-weighted average energy. In this case, the T_i states in region I begin to acquire their S_1 character mainly through one channel, interaction with the mixed state of predominant T_3 character, because of their proximity to this state. As before, in the absence of two comparably efficient pathways for acquiring S_1 character, destructive interference effects are minimized, and the T_i states in region I become SEELEM detectable, thereby shifting the intensity-weighted average energy of the SEELEM spectrum toward the red of S_1 basis state energy.

Identical arguments can be given to explain the situation when the T_3 state tunes to the blue of the S_1 state. The trends repeat themselves in a symmetric fashion as can be seen from the *doorway* SEELEM trace (points $\triangle$) in Fig. 5-2.

The distinct shapes of the two traces corresponding to *direct* vs *doorway-model*

SEELEM spectra in Fig. 5-2 suggest that the intensity-weighted average energy of the SEELEM spectrum can be used as a diagnostic to distinguish between *direct* and *doorway-mediated* coupling schemes. However, additional information can be extracted from the SEELEM intensity-weighted average energy plot. Suppose the system being studied reveals itself to exhibit *doorway-mediated* coupling. It is then possible to obtain a rough estimate of the rotational constant, B, of the special doorway state, by following the steps outlined below.

The intensity-weighted average energy plot for the synthetic *doorway-mediated* SEELEM spectrum of acetylene in Fig. 5-2 exhibits peaks and troughs at special energies of the T_3 state, which can be correlated with specific mixing angles between the S_1 bright state and the T_3 doorway state. The mixing angle between S_1 and T_3 is simply the ratio of their coupling matrix element to the difference in their zero order energies. Therefore, the first step is to associate specific mixing angles with the peaks and troughs of the intensity-weighted average energy plot of the synthetic SEELEM spectrum. The second step is to compare the intensity-weighted average energy plot of an experimental SEELEM spectrum with that of the synthetic spectra and identify the matching peaks and troughs (note that each rotational line of an experimental SEELEM spectrum corresponds to a synthetic SEELEM spectrum simulated for a specific energy of the doorway state). Once specific mixing angles are assigned to the various features of the intensity-weighted average energy plot of the experimental SEELEM spectrum, one can proceed to the next step.

The final step in this analysis involves the computation of the zero-order energies of the different rotational levels of the doorway state. This can be achieved *if* one knows the value of the coupling matrix element between the bright state and the doorway state. Let us initially assume that this coupling matrix element between the bright state and the doorway state of our system is known. Then the energies of several rotational levels of the doorway state can be computed from the known mixing angles defined by each peak and trough in the intensity-weighted average energy plot of the experimental SEELEM spectrum. At this point, a reasonable estimate of the rotational constant B of the doorway state is obtained by a simple linear fit to these rotational level energies. However, this analysis depends on knowing the coupling matrix element between the bright state and the doorway state. This important piece of information *can* be independently obtained when the skewness measure is applied to the spectrum!

The second statistical measure, *intensity weighted skewness*, can also be used to distinguish between *doorway-mediated* and *direct* models (Fig. 5-4). The *doorway-mediated* SEELEM spectrum is skewed to the blue of its intensity-weighted average energy when the energy of the T_3 basis state is to the red of S_1. The *doorway-mediated* SEELEM spectrum becomes non-skewed when T_3 is degenerate with S_1. Once T_3 moves to the blue of S_1, the *doorway-mediated* spectrum becomes skewed to the red of its intensity-weighted average energy. In other words, the SEELEM spectrum is always skewed toward the energy of the S_1 basis state (and away from the energy of the T_3 basis state) if the coupling is *doorway-mediated.* As mentioned above in the discussion of the intensity-weighted average energy, there will always be a group of eigenstates localized around the energy of S_1 that contribute to the SEELEM signal in the *doorway-mediated* coupling case. This detectable cluster near S_1 is more important than a similar cluster near T_3 since S_1 character is a more important factor in SEELEM detectivity. Therefore, the eigenstates in the vicinity of S_1 with just the right amount of S_1 character will appear in the SEELEM spectrum, thereby skewing it toward the energy of the S_1 basis state.

The *direct* model SEELEM spectrum is non-skewed because, as S_1 is coupled directly to each of the background states T_i, the fractionation of S_1 is symmetric.

Thus the intensity weighted skewness parameter can be used to distinguish between *direct* and *doorway-mediated* coupling models. In the case of *direct* coupling, the SEELEM spectrum will be non-skewed whereas, in the case of *doorway-mediated* coupling, the SEELEM spectrum will be skewed. Furthermore, in the case of *doorway-mediated* coupling, the evolution of the intensity weighted skewness of the SEELEM spectrum will be correlated with the direction of the tuning of the doorway state relative to S_1. For instance, if the intensity weighted skewness starts out positive at low J, goes through zero, and becomes negative after the doorway state crosses the bright

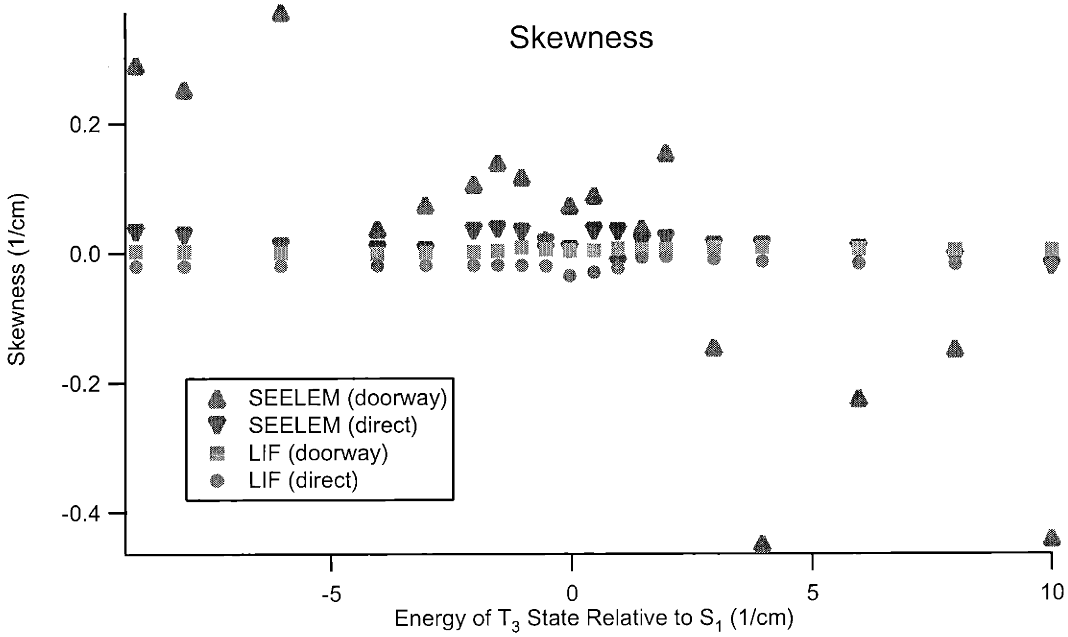

Figure 5-4: Intensity weighted skewness of the simulated LIF and SEELEM spectra of acetylene for the *direct* and doorway-mediated coupling models.

state, this would correspond to the doorway state overtaking the bright state from below. This implies that the doorway state has a larger rotational constant (B-value) than the bright state. The intensity weighted skewness parameter can also locate the bright state / doorway state crossing point in the case of *doorway-mediated* coupling because the skewness of the SEELEM spectrum becomes zero at the crossing point. Once the crossing-point is located, the bright state $\sim$ doorway state coupling strength can be estimated because, at the point where these two states are degenerate, the LIF spectrum collapses into two features of comparable intensity separated by about twice the bright state $\sim$ doorway state coupling matrix element. If the bright state $\sim$ doorway state coupling strength can thus be deduced, one can proceed with the analysis outlined in the discussion of the intensity-weighted average energy to obtain an estimate of the doorway state rotational constant.

The third statistical measure, cross-correlation, also exhibits diagnostically distinct shapes for the *doorway-mediated* vs. the *direct* model (Fig. 5-5). Cross-correlation is a measure of the overlap between the synthetic SEELEM and LIF

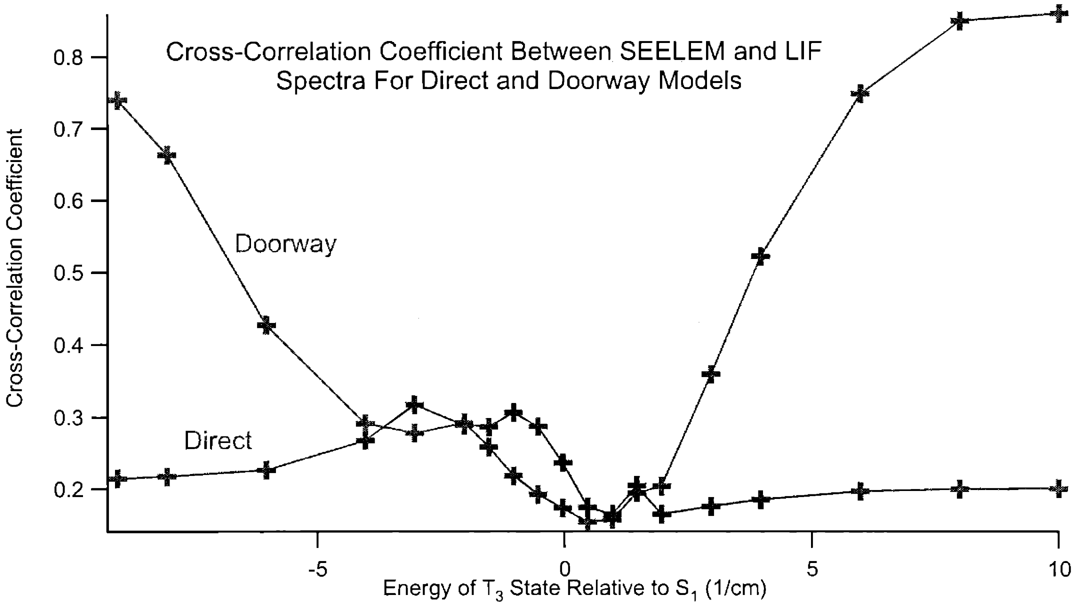

Figure 5-5: Cross-correlation coefficient of the simulated LIF and SEELEM spectra of acetylene for the *direct* and *doorway-mediated* coupling models.

spectra as their resolution is degraded (Eq. 5.9). The plot in Fig. 5-5 reflects the case where the resolution is that of a typical grating scan for our laser (0.4 cm^{-1}, Lambda Physik FL 3002E). On the vertical scale, 1 and 0 represent respectively perfect correlation and anti-correlation. The resolution of the LIF and SEELEM spectra is degraded by replacing the stick that represents each eigenstate in the synthetic spectrum by a Gaussian lineshape centered at the energy of the eigenstate and with an area proportional to the intensity of that eigenstate. The width of each Gaussian curve is determined by the resolution.

At infinite resolution, or when one reaches the limit of a stick spectrum, the cross-correlation coefficients approach 0. This occurs because eigenstates with large LIF intensity are short-lived and decay before reaching the SEELEM detector. Consequently, those eigenstates do not appear in the SEELEM spectrum. In this sense, the LIF and SEELEM spectra are almost complementary.

The feature in the cross-correlation plot that distinguishes the *doorway-mediated* from the *direct* model is the behavior at the extreme T_3 energies, *i.e.* when T_3 is far to the red or blue of the S_1 basis state. In those regions, the cross-correlation between LIF and SEELEM spectra for the *doorway-mediated* model is quite large. This is consistent with the features of the intensity-weighted average energy plot of the *doorway-mediated* SEELEM spectra discussed previously. When the doorway state lies about 8 cm^{-1} either to the red or blue of the S_1 state, the intensity-weighted average energy of the *doorway-mediated* SEELEM spectrum almost coincides with the energy of the S_1 basis state (Fig. 5-2). Since the vicinity of the S_1 basis state energy is precisely where the eigenstates that make the strongest contribution to the LIF spectrum are located, one expects that the LIF and SEELEM spectra will overlap substantially when the doorway state is distant from the bright state, once the spectral resolution has been degraded. As the doorway state energy approaches that of the bright state, the intensity-weighted average energy of the *doorway-mediated* SEELEM spectrum shifts away from the S_1 basis state energy. Hence the cross-correlation coefficient between the *doorway-mediated* SEELEM and LIF spectra starts to decrease. As the doorway state tunes through the S_1 state, the intensity-weighted average energy of the SEELEM spectrum again coincides with the S_1 basis state energy. This situation translates into a slight enhancement in the cross-correlation coefficient at the S_1 / T_3 crossing point and gives rise to the small secondary maximum in the *doorway-mediated* model cross-correlation plot at the S_1 basis state energy (Fig. 5-5). Note that for an eigenstate to be both LIF and SEELEM detectable, its S_1 fractional character must be around 0.014. This is the maximum S_1 fractional character tolerated before an eigenstate ceases to be SEELEM detectable as determined from the plots of the SEELEM signal presented in Fig. 5-1a and Fig. 5-1b. This number is also the minimum S_1 fractional character that gives rise to resolvable LIF peaks based on what Drabbels *et al.* observed in their 18 MHz resolution spectrum [35]. There is only a very small overlap between the ranges of fractional S_1 characters that are detectable by both LIF and SEELEM.

It is also interesting to note that at the S_1 / T_3 crossing point, the cross-correlation factors for both models behave similarly. When the *doorway* state is degenerate with S_1, the *doorway-mediated* model reduces to a special case of *direct* coupling.

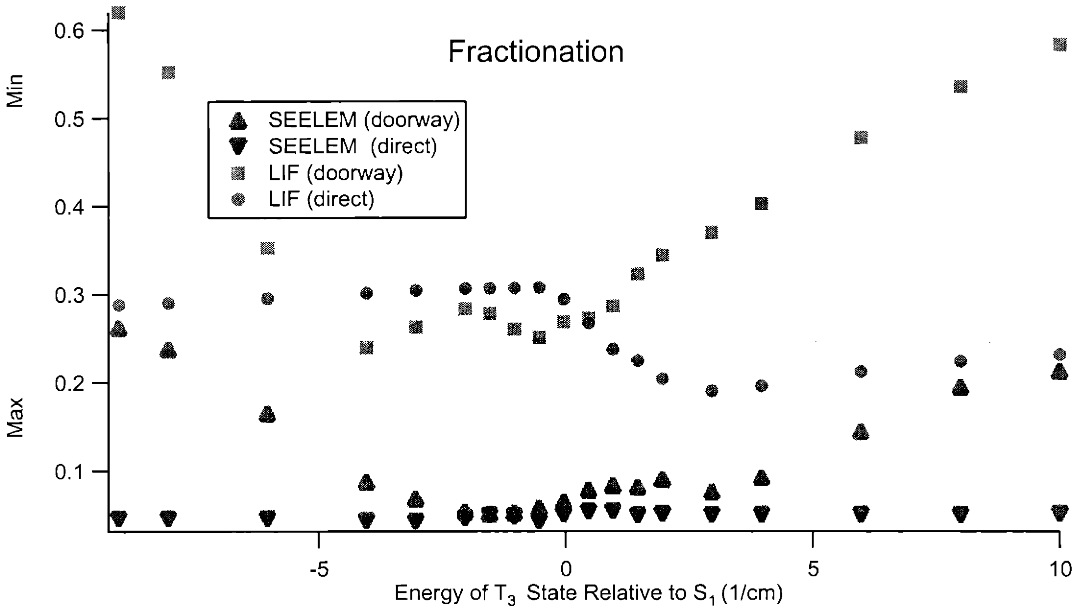

Figure 5-6: Fractionation coefficient of the simulated LIF and SEELEM spectra of acetylene for the *direct* and doorway-mediated coupling models.

Therefore, all of the statistical measures introduced in this paper behave identically at the S_1 / T_3 crossing point for both the *doorway-mediated* and *direct* models.

The final statistical measure discussed here, fractionation, also behaves differently for *doorway-mediated* and *direct* models as a function of T_3 basis state energy (Fig. 5-6). The fractionation index goes from 1 (no fractionation) to 1/N (maximum fractionation), where N is the number of eigenstates (Eq. (5.10)). N = 212 in this particular case since the initial Hamiltonian matrix was constructed with 212 basis states. The overall trend in fractionation is that the *doorway-mediated* SEELEM and LIF spectra are less fractionated than their *direct* model counterparts when the energy of T_3 is far away from that of S_1, and become progressively more fractionated as the T_3 state approaches the S_1 state. At the point of degeneracy, both coupling models give rise to the same degree of fractionation in the SEELEM and LIF spectra. Therefore, the diagnostic region in the LIF and SEELEM fractionation profiles is the energy region where T_3 is distant from the energy of S_1.

The fractionation profiles obtained for the *doorway* model SEELEM and LIF spectra are a consequence of the fact that, in the *doorway-mediated* model, eigenstates acquire their S_1 character through T_3. Hence, when the doorway state lies far from the bright state, the S_1 character cannot be distributed extensively over the background states. Since it is the bright state character of the eigenstates that gives rise to their SEELEM and LIF signals, the fractionation profile of the bright state dictates the fractionation profiles of both LIF and SEELEM detectable states.

We were not able to apply all of the statistical measures presented in this paper to real spectra obtained from our first-generation molecular beam machine. The effectiveness of the statistical analysis method that is described here depends critically on the accuracy of the J-assignments of each feature in the experimental spectrum. This, in turn, requires high-quality raw data. Although our first-generation apparatus failed to generate what could be described as high-quality data, we were still able to look at the qualitative trends in the intensity weighted skewness of our SEELEM spectra. Figure 5-7 shows a section of the acetylene S_1 $3\nu_3$ SEELEM spectrum featuring the R(1), R(2) and the R(3) lines. The intensity weighted skewness starts out as positive at R(1), goes through zero at R(2), and becomes negative at R(3) implying that the S_1/T_3 cross-over happens very close to J'=3 and that the T_3 doorway state overtakes S_1 from below. These conclusions have been confirmed by an independent analytical method which will be described next in the second part of this chapter.

5.4 Conclusion

We have identified four statistical measures that, when applied to experimental SEELEM and LIF spectra, will identify the *doorway* vs. *direct* mechanism by which the bright state of the molecular system under investigation couples to a background manifold of dark states. The specific results presented in this chapter were based on acetylene as a model system, however the conclusions can be generalized to any system. The parameters used in the simulations, such as the bright-state $\sim$ doorway-state coupling strength, the doorway state $\sim$ dark manifold coupling strength, and the density of dark states are the only system-specific variables and can easily be modified to derive

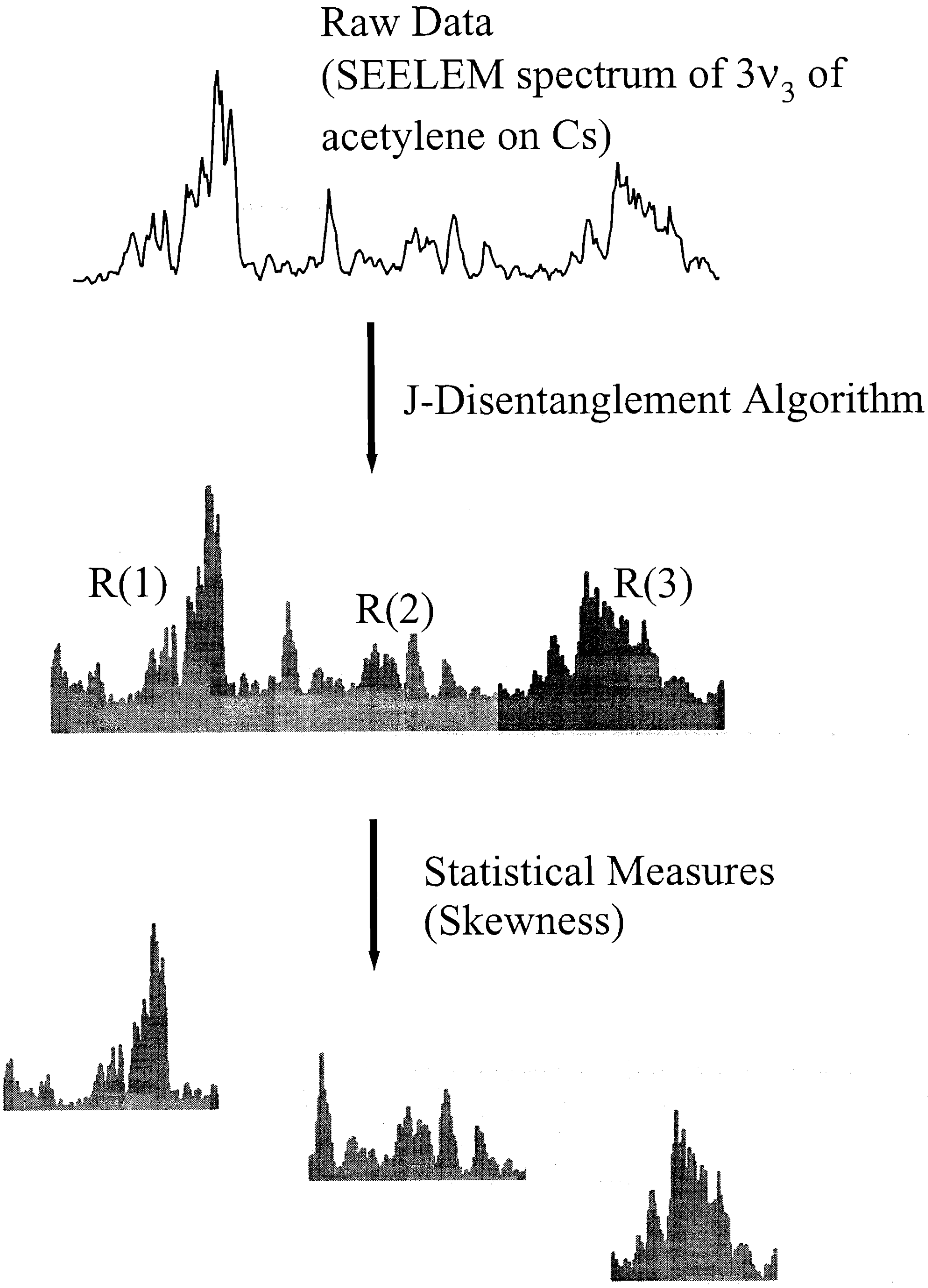

Figure 5-7: The intensity weighted skewness of a section of the SEELEM spectrum in the region of S_1 $3\nu_3$ of acetylene acquired on Cs in the first-generation apparatus.

new results for other systems.

The trends observed in each of the statistical measures introduced here, as the doorway state T_3 tunes relative to the bright state S_1 with J, can be summarized as follows:

The *intensity-weighted average energy* of the SEELEM spectrum for the *doorway-mediated* model oscillates about the bright state S_1 energy as a function of J following what could be described as a fifth-order polynomial (Fig. 5-2). In contrast, the intensity-weighted average energy of the peaks in the SEELEM spectrum for the *direct* coupling model remains very close to the S_1 energy as a function of J.

The *intenisty weighted skewness* parameter is the most effective statistical discriminant between *doorway-mediated* and *direct* models (Fig. 5-4). In the case of *direct coupling*, the SEELEM spectrum will be non-skewed. However, in the case of *doorway-mediated* coupling, the SEELEM spectrum *will* be skewed and the degree and sense of this skewness will vary with J in a diagnostically useful way. The intensity weighted skewness parameter identifies the S_1 / T_3 crossing point in the case of *doorway-mediated* coupling. When the doorway and bright basis states are degenerate, the SEELEM spectrum becomes non-skewed. At J levels where the T_3 state lies below S_1, the SEELEM spectrum will be positively skewed (*i.e.* each rotational line of the SEELEM spectrum contains prominent peaks which lie to the blue of the intensity-weighted average energy of this rotational line). For J levels where T_3 lies above S_1, the skewness of the SEELEM will reverse sense (*i.e.* peaks will lie to the red of the intensity-weighted average energy).

The *cross-correlation* parameter is also capable of distinguishing between the two coupling models (Fig. 5-5). If the coupling is *doorway-mediated*, the SEELEM and LIF spectra are expected to be highly correlated at J levels far to the red and blue of the S_1/T_3 crossing point. The cross-correlation is expected to diminish as the crossing point is approached. On the other hand, the cross-correlation parameter for the *direct* model will not be strongly J-dependent.

The trends observed for the *fractionation* parameter (Fig. 5-6) imply that the widths of the active regions in the LIF and SEELEM spectra will monotonically increase to a maximum at the S_1/T_3 crossing-point if the coupling is *doorway-mediated.* For the *direct* coupling case, neither the LIF nor the SEELEM spectrum will exhibit any significant variation of the fractionation parameter as a function of J.

The statistical measures described in this paper are shown to distinguish between two coupling schemes that are proposed for the interaction of a bright state with a background manifold of dark states in a molecular system such as acetylene. In addition to such qualitative information, these measures can also yield quantitative information about this bright state $\sim$ dark manifold interaction. For instance, in the case of the *doorway-mediated* coupling, an analysis outlined in Section 5.3, which uses both the *intensity-weighted average energy* and the *skewness* parameter, can yield estimates of the coupling strength between the doorway state and the bright state and the rotational constant of the doorway state.

Our first attempt at qualitatively applying the statistical measures described in this paper to real data yielded a result which can be considered as the first step towards the development of a mechanistic understanding of the Intersystem Crossing process in small polyatomic molecules. The strength of the current analytical approach comes from the fact that it is based directly on the statistical properties of a J-sorted raw data set and eliminates the need to fit the eigenvalues of a Hamiltonian matrix model to an extensively pre-processed data set. It is a different way of looking at a different kind of spectra, *i.e.* SEELEM spectra.

5.5 Appendix

This section outlines the derivation of an expression which gives the amount of S_1 bright state character acquired by a specific background state, T_b, in the case of *doorway-mediated* coupling. Such an expression gives insight into the various trends observed in the statistical measures discussed in this paper because one can see the explicit dependence of the S_1 bright state character of the eigenstate, B_b, of nominal T_b character on parameters such as the energy of the doorway state T_3 and the energy of the basis state T_b.

M_1 and M_2 are mixed states of nominal S_1 and T_3 character respectively:

$$|M_1>= cos(\theta)|S_1> -sin(\theta)|T_3>$$
$$|M_2>= sin(\theta)|S_1> +cos(\theta)|T_3>$$

After the T_b basis state mixes with M_1 and M_2 for a given energy of the T_3 state, the nominal T_b eigenstate, B_b, can be expressed as follows:

$$|B_b>= \gamma|T_b> + \frac{<T_b|\hat{H}_{so}|M_1>}{E_{T_b}-E_{M_1}}|M_1> + \frac{<T_b|\hat{H}_{so}|M_2>}{E_{T_b}-E_{M_2}}|M_2>$$

which can be further expanded as:

$$|B_b>= \gamma|T_b> - \frac{cos(\theta)sin(\theta) <T_b|\hat{H}_{so}|T_3>}{E_{T_b}-E_{M_1}}|S_1> + \frac{sin(\theta)cos(\theta) <T_b|\hat{H}_{so}|T_3>}{E_{T_b}-E_{M_2}}|S_1> + \frac{sin^2(\theta) <T_b|\hat{H}_{so}|T_3>}{E_{T_b}-E_{M_1}}|T_3> + \frac{cos^2(\theta) <T_b|\hat{H}_{so}|T_3>}{E_{T_b}-E_{M_2}}|T_3>$$

because:

$$|M_1>= cos(\theta)|S_1> -sin(\theta)|T_3>$$
$$|M_2>= sin(\theta)|S_1> +cos(\theta)|T_3>$$

and the T_b basis state has non-zero off-diagonal matrix elements only with the T_3 basis state since this is the *doorway-mediated* coupling mechanism. Note that $|M_1>$ is of predominant $|S_1>$ character when the energy of the $|T_3>$ basis state is far away from that of $|S_1>$ (*i.e.* when the mixing angle $\theta \cong 0$).

Therefore, the mixing coefficient of the $|S_1>$ basis state in the nominal $|T_b>$ eigenstate is:

$$C_{S_1}^{B_b} = -[\frac{sin(2\theta)}{2}\frac{<T_b|\hat{H}_{so}|T_3>}{E_{T_b}-E_{M_1}} + \frac{sin(2\theta)}{2}\frac{<T_b|\hat{H}_{so}|T_3>}{E_{T_b}-E_{M_2}}]|S_1>$$

and that of the $|T_3>$ basis state is:

$$C_{T_3}^{B_b} = [\frac{sin^2(\theta) <T_b|\hat{H}_{so}|T_3>}{E_{T_b}-E_{M_1}} + \frac{cos^2(\theta) <T_b|\hat{H}_{so}|T_3>}{E_{T_b}-E_{M_2}}]|T_3>$$

Chapter 6

Retrieving Electronic Coupling Mechanisms Underlying Complex Spectra II - An Assumption-Violating Application of the Lawrance-Knight Deconvolution Procedure

The Lawrance - Knight (L-K) deconvolution method is a spectral inversion scheme which allows one to relate an absorption or a fluorescence spectrum to the energies and couplings of the zero-order states via analytical expressions. In order to obtain accurate results, the L-K method can only be applied to spectra that arise from one precisely defined zero-order picture. Namely, a single bright state must be coupled directly to a background of non-interacting dark states, the "direct coupling model". In most situations, the zero-order picture that gives rise to a particular absorption or a fluorescence spectrum is not known a priori. Nonetheless, it is typically assumed that the zero-order circumstances governing the spectral intensities are as described above, and the L-K method has been applied indiscriminantly to the spectra of a variety of systems such as pyrazine, acetylene, and naphthalene to extract zero-order parameters. We show here that if the L-K algorithm is applied to spectra where the underlying zero-order picture departs from the direct coupling limit, the resulting output has characteristic qualitative and quantitative features that reflect this situation. By applying the L-K method to a series of simulated spectra, we recover from a pattern of patterns new information about the couplings among the dark states. We have specifically considered the alternative picture of a single bright state coupled to a background of non-interacting states by a doorway-mediated mechanism. We demonstrate here that the L-K algorithm can be employed to distinguish between the contrasting doorway-mediated and direct coupling schemes, and also to obtain coupling matrix elements.

6.1 Lawrance-Knight Deconvolution Procedure

The first step in extracting a description of intramolecular dynamics from a complex, experimental, frequency-domain spectrum is to define the zero-order basis set that best describes the molecular system under study. Once the interacting zero-order states are known, an effective Hamiltonian can be formulated. Then the matrix elements that mix the zero-order states can be accurately determined, usually by a least squares adjustment of the parameters that define the effective Hamiltonian model. Once this is accomplished, the time evolution of any coherent superposition state constructed from zero-order states can be easily calculated. Therefore, retrieval of the zero-order parameters constitutes the essential step in spectral data analysis.

The conventional approach to analysis of spectra in terms of zero-order states and their interactions is a complicated, iterative, trial-and-error procedure. There are two serious obstacles to a successful, physically meaningful fit: (i) one must know in advance the qualitative nature of the interaction mechanism, (ii) one must prevent the highly nonlinear fit procedure from becoming trapped in a local minimum (typically associated with forcing an avoided crossing to occur at an incorrect value of a rotational quantum number) of the variance-covariance hypersurface. The L-K deconvolution, on the other hand, yields a unique solution because it relates the zero-order parameters directly to the experimental spectrum through algebraic relationships [12, 83]. It is limited only by the quality of the spectrum. The principle on which the L-K deconvolution method is based, was first proposed by Berg, and again independently by Ziv and Rhodes [12, 154]. The basic idea behind the L-K deconvolution algorithm is that the Green function for the zero-order state that carries the oscillator strength defines the absorption spectrum (or the laser induced fluorescence spectrum in cases where the fluorescence intensities are directly proportional to absorption intensities). The absorption cross section for dipole-induced transitions from the ground state $|g>$ to an energy E is given by

$$\sigma(E) = \zeta\ E\ \mathrm{Im}(< g|\mu G(E)\mu|g > \tag{6.1}$$

where ζ is a constant, μ denotes the dipole moment operator, and G(E) is the Green function, defined by

$$G(E) = lim_{\gamma\rightarrow 0}[H - (E + i\gamma)I]^{-1} \tag{6.2}$$

Here **H** denotes the molecular Hamiltonian and **I** is the identity matrix. By making use of the closure relationship

$$\sum_{k} |k >< k| = I \tag{6.3}$$

Eq. (6.1) can be re-written

$$\sigma(E) = \zeta\ E\ \mathrm{Im}[\sum_{k,l} < g|\mu|k >< k|G(E)|l >< l|\mu|g >]$$

$$\sigma(E) = \zeta E \sum_{k,l} < g|\mu|k >< l|\mu|g > \mathrm{Im}G_{kl}(E) \tag{6.5}$$

where $< k|G(E)|l >$ is abbreviated as $G_{kl}(E)$. For the case where the states used in the closure relationship are the eigenstates of **H**, we have

$$\sigma(E) = \zeta\ E \sum_{l} \mid < l|\mu|g > \mid^2 \mathrm{Im} G_{ll}(E) \tag{6.6}$$

since

$$< k|H|l >= \delta_{kl}\epsilon_l$$

From Eq. (6.2) it follows that

$$G_{ll}(E) = lim_{\gamma\to 0}\frac{l}{\epsilon_l - E - i\gamma} \tag{6.8}$$

Substitution of the imaginary part of $G_{ll}(E)$ from Eq. (6.8) into Eq. (6.6) yields

$$\sigma(E) = \zeta\ E \sum \mid < l|\mu|g > \mid^2 \delta(\epsilon_l - E) \tag{6.9}$$

As can be seen, Eq. (6.9) has the basic features of an absorption spectrum. Peaks appear only at energies corresponding to the eigenenergies of the system with intensities proportional to the square of the dipole matrix element connecting the initial ground state $|g>$ to the final molecular state $|l>$.

Lawrance and Knight elegantly describe the mathematical details of this deconvolution procedure [83]. The L-K method allows one to derive the zero-order matrix elements, *i.e.* the zero-order energies and the coupling strengths, directly from the spectra. The L-K method is designed to apply exclusively to cases where only one of the zero-order states carries oscillator strength. It is important to note that all of the "dark" states in the L-K spectral inversion procedure are required to be diagonal (or "pre-diagonalized") with respect to the chosen zero-order Hamiltonian *except* for their off-diagonal matrix element with a single bright state. In other words, no couplings among the dark states themselves can be recovered through the L-K method. This point was specifically addressed by Lehmann in his comment on the Lawrance - Knight paper [88, 84].

The input for the L-K deconvolution algorithm is a set of measured relative intensities (*i.e.* intensities of the components of a single fractionated rotational line such as P(3), all of which belong to a $J' = 2 \leftarrow J'' = 3$ transition), which can be directly correlated with bright state character, and eigenenergies derived from a *well-resolved* experimental spectrum (the method can also be applied to incompletely resolved spectra, however, the calculations are then slightly more complicated).

The output from the L-K algorithm is a function which is a sum of Lorentzian curves, where each Lorentzian is centered at the zero-order energy of a dark state and has a peak height which is directly related to the coupling strength of that dark state to the single bright state. It should be noted that the output function contains information only about the zero-order dark states and their coupling to a unique bright state. The zero-order energy of the bright state is obtained from the intensity-weighted average energy of the experimental spectrum.

The uniqueness of the L-K de-diagonalization procedure can be illustrated as follows. Suppose the molecular system under study has N dark states. Then the zero-order Hamiltonian matrix describing this system would have 2N + 1 independent elements: the eigenenergies of the N dark states plus one bright state, and the N coupling strengths of the N dark states to the bright state. For a solution to be unique there must be 2N + 1 independent pieces of input data to determine 2N + 1 unknowns. As it turns out, the experimental absorption (or fluorescence) spectrum yields exactly 2N + 1 pieces of independent data: N + 1 eigenenergies, and N relative intensities [83]. Therefore, the quantitative details of any more complicated zero-order picture that is expressed in terms of more than 2N + 1 independent parameters, such as would be required when there is coupling between the dark states themselves, cannot be recovered through the L-K algorithm. This restricts the applicability of the L-K algorithm, in its present formulation, to cases where a single bright state fractionates statistically into a manifold of dark states.

Typically one knows *a priori* that a particular spectrum is illuminated by a single bright state. However, it is much more difficult to know whether the prediagonalized dark state picture is more mechanistically apt than one where a small number of dark states play a dominant role in facilitating the interaction between the unique bright state and the manifold of dark states. Although it is always possible to assume a prediagonalized dark state basis set, doing so could corrupt mechanistically important information. We will now show that certain features of the L-K output can provide both qualitative and quantitative information about the coupling mechanism and matrix elements, even in an assumption-violating, "doorway-mediated", non-prediagonalized basis.

6.2 L-K Algorithm as a Tool to Retrieve Electronic Coupling Mechanisms

The first part of this chapter presents statistical measures for distinguishing two limiting mechanisms for spin-orbit coupling in molecules such as acetylene: *direct* and *doorway-mediated* coupling. In the *doorway* mechanism, the bright state couples to the manifold of dark states via a specific dark state, the *doorway* state. It is important to be able to distinguish between *direct* and *doorway* coupling schemes in order to obtain a mechanistic as opposed to a phenomenological picture of non-radiative relaxation in molecules. Even though the specific formulation of the L-K procedure appears to exclude its application to *doorway* model couplings, it turns out that the L-K algorithm *does* provide information about the coupling mechanisms in experimental spectra. The capability of the L-K algorithm to yield insight into the coupling mechanisms was unexpected.

A question that would be interesting to explore is what would happen if the L-K algorithm were applied to a spectrum that did not represent a zero-order situation where the bright state couples directly to a background of non-interacting dark states. Does the output of the L-K deconvolution procedure exhibit characteristics that are diagnostic of indirect coupling?

In order to address this question, the L-K algorithm was applied to synthetic absorption spectra that resulted from doorway-mediated model Hamiltonians. The parameters used in the construction of the doorway-mediated model Hamiltonian were the energies of the zero-order states, the bright state $\sim$ doorway state coupling strength, and the individual coupling strengths between the doorway state and each of the dark states. The bright state $\sim$ doorway state coupling strength was selected to be about ten times larger than the "average" coupling strength between the doorway state and the background manifold. "Average" in this context signifies the square root of the variance of doorway state $\sim$ background coupling strengths that were chosen from a normal distribution with mean zero. It was observed that the L-K algorithm failed to yield accurately the *a priori* specified coupling matrix elements between the zero-order dark states and the bright state in the case of spectra derived from the *doorway-mediated* model Hamiltonian (Fig. 6-1). This was not surprising. Furthermore, the distribution of the Lorentzian curves in the L-K output function representing the basis state energies and coupling strengths was greatly skewed with respect to the midpoint of the energy axis [1].

In contrast, the L-K algorithm worked perfectly when it was applied to synthetic spectra that were generated from a *direct* coupling Hamiltonian model (Fig. 6-2). There was no skewness observed in the distribution of the Lorentzians in the L-K output function. This lack of skewness was expected because the coupling matrix elements between the bright state and the dark states in the direct model Hamiltonian were chosen from a normal distribution with mean zero.

A skewness parameter, S, was computed for the distribution of Lorentzians in the L-K output function:

$$S = \sum_i I_i^2 \times (E_i - E_0) \tag{6.10}$$

In Eq. (6.10), I_i represents the intensity of the i^{th} Lorentzian in the L-K output, E_i represents its energy, and E_0 represents the midpoint of the energy axis of the L-K output. E_0 approximately coincides with the energy of the bright state since an

---

[1] The midpoint of the energy axis of the L-K output approximately coincided with the energy of the bright state, since in the zero-order matrix, the bright state was centered on a window of 200 dark states, *i.e.* there were 100 dark states to the red of the bright state and 100 dark states to the blue of the bright state. The energies of the dark states were distributed randomly over an energy interval of about 20 cm^{-1}. Therefore, although the overall density of states was 10/cm^{-1}, there were local density fluctuations.

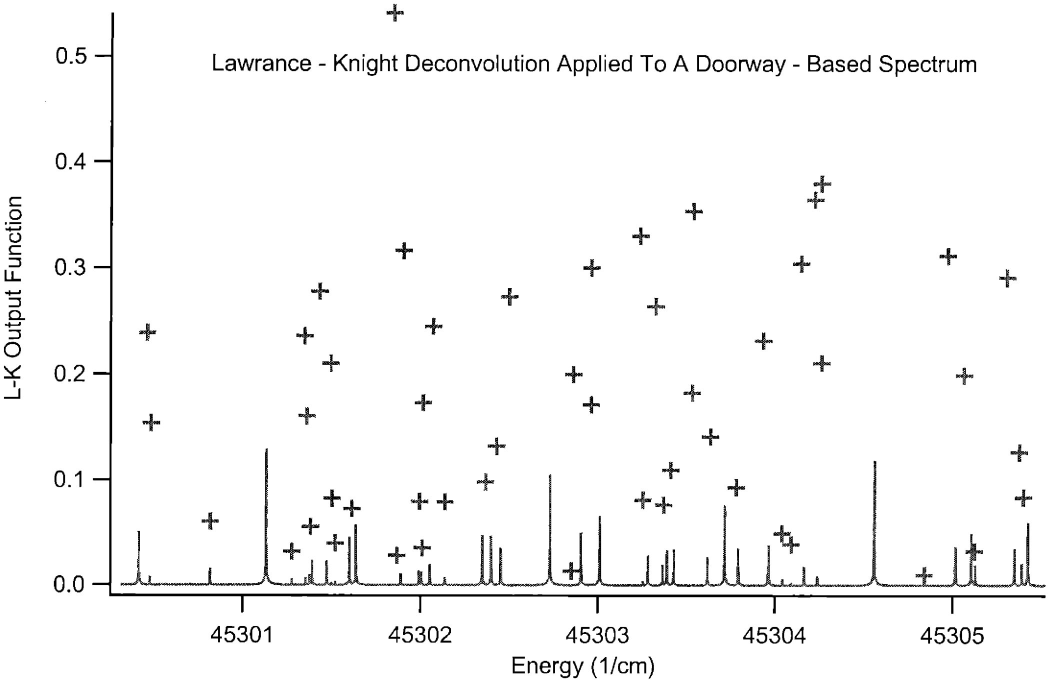

Figure 6-1: Application of the L-K algorithm to a spectrum derived from a doorway-coupling Hamiltonian. Each cross represents the zero-order coupling strength of a background state T_i to the doorway state T_3. Each cross appears at the zero-order energy of the basis state T_i. The L-K algorithm fails to predict the zero-order coupling strengths and energies in this case. The L-K output in this figure has a minimum skewness since the bright state S_1 and the doorway state T_3 were degenerate in the particular formulation of the Hamiltonian that gave rise to this spectrum. As T_3 tunes away from S_1 in the doorway-coupling scheme, the L-K output exhibits skewness in the distribution of its maxima, which is a diagnostically useful feature.

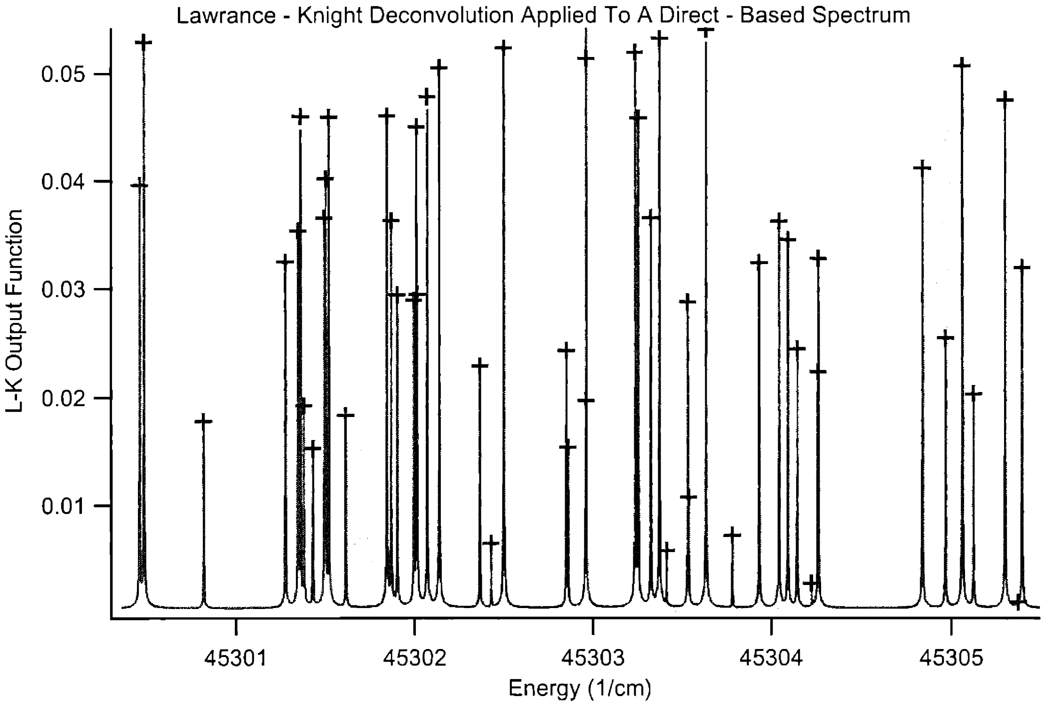

Figure 6-2: Application of the L-K algorithm to a spectrum derived from a direct coupling Hamiltonian. Each cross represents the zero-order coupling strength of a background basis state T_i to the bright state S_1 in a direct coupling scheme. Each cross appears at the zero-order energy of the basis state T_i. The L-K algorithm recovers the correct coupling strengths and zero-order energies from the spectrum derived from a direct-coupling model Hamiltonian.

equal number of dark states were present on either side of where the bright state was located.

The magnitude of the skewness in the case of doorway-mediated coupling was observed to change as a function of the difference between the zero-order energy of the doorway state and that of the bright state. Since the bright and doorway states typically have different rotational constants, the energy separations between these states will vary monotonically with J, the rotational quantum number. This provides *a pattern in a sequence of L-K outputs* that contains information unobtainable from a single application of the L-K algorithm. By applying the L-K algorithm to a series of simulated spectra, each representing a different doorway zero-order energy relative to the bright state energy, we recover from *a pattern of patterns* new information about the couplings among the dark states. The skewness of each L-K output function obtained from each simulated spectrum was plotted as a function of the doorway state energy relative to the bright state energy. A linear dependence of skewness on the zero-order doorway state energy was revealed (Fig. 6-3). Furthermore, the slope of this line was found to be approximately equal to the square of the bright state $\sim$ doorway state coupling matrix element specified in the doorway Hamiltonian. The L-K output function became non-skewed at the precise point where the doorway state was tuned into degeneracy with the bright state.

The empirical finding, that the slope of the line of skewness vs. doorway state energy was approximately equal to the square of the bright state $\sim$ doorway state off-diagonal matrix element, was shown analytically to be a general result by applying perturbation theory to a 3x3 matrix which contained three basis states, a bright state, a doorway state, and a background state (Section 6.4). These results indicate that an "incorrect" application of the L-K procedure to spectra that encode a doorway-coupling scheme, gives rise to well-defined qualitative diagnostics capable of identifying the underlying zero-order coupling scheme. Furthermore, these same characteristics can yield quantitative measures, such as skewness, that can be related to zero-order parameters such as the bright state $\sim$ doorway state coupling strength. However, these results were obtained from simulated spectra.

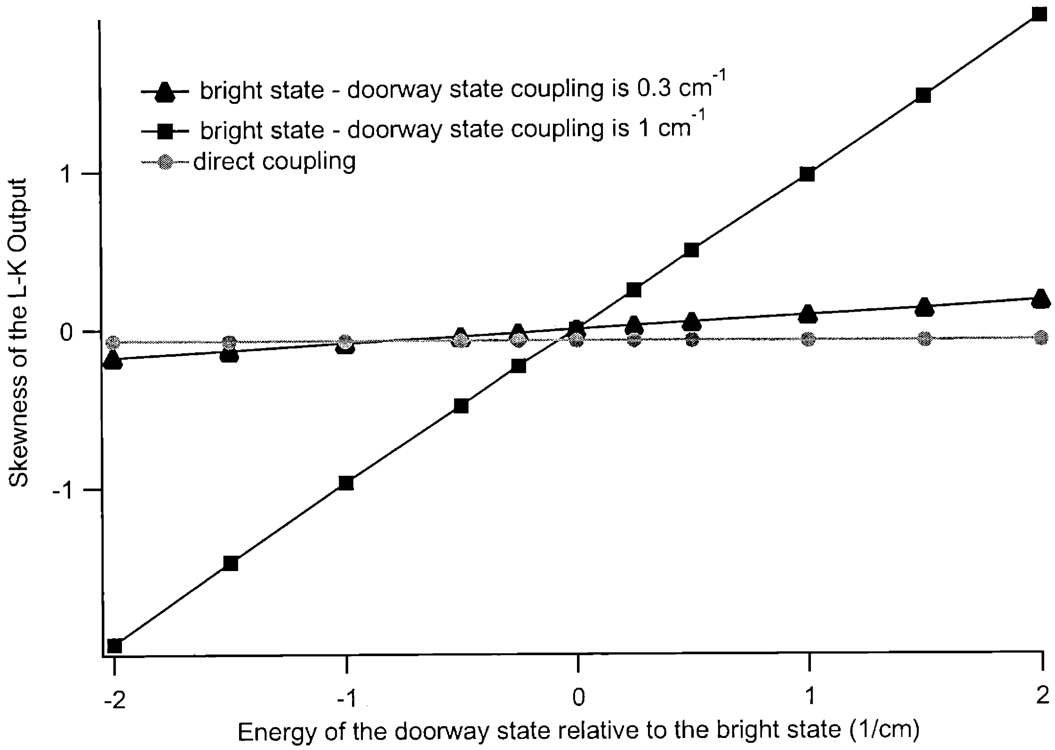

Figure 6-3: The skewness of the distribution of the Lorentzian curves in the output of the L-K function applied to a series of simulated spectra. The gray line denoted by solid circles arises from spectra derived from a direct model Hamiltonian, the other two lines represent the doorway model. Each line represents a series of simulated spectra, each of which was characterized by a specific zero-order energy of the doorway state relative to the bright state. It should be noted here that in the case of direct coupling, the state labelled as the "doorway state" has no special properties, it is just one state in the dark manifold. The difference between the two doorway model lines is the doorway state $\sim$ bright state coupling matrix element specified in the Hamiltonian. The flatness of the line representing spectra derived from a direct model Hamiltonian shows that there is no skewness in the L-K output in direct coupling situations. Doorway mediated coupling, on the other hand, gives rise to systematic skewness in the L-K output and the slope of the lines are proportional to the square of the doorway state $\sim$ bright state coupling matrix element.

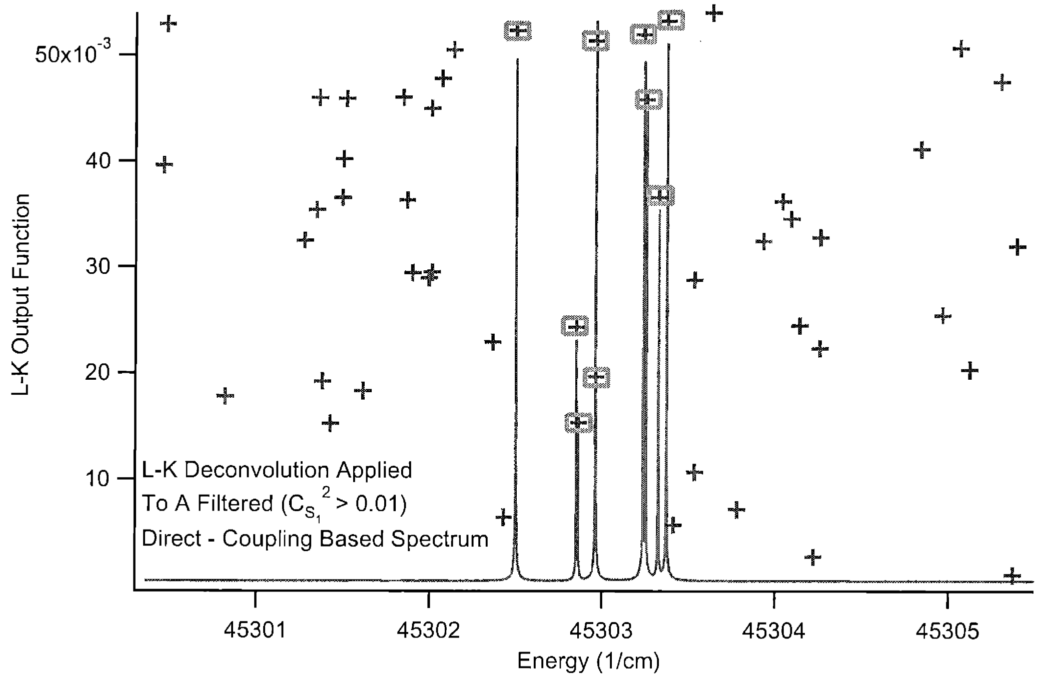

Figure 6-4: Application of the L-K algorithm to a spectrum derived from a filtered subset of the eigenstates of a direct-coupling Hamiltonian. Only eigenstates with bright-state character greater than 0.01 were used to compute the synthetic absorption spectrum to simulate the effects of experimental sensitivity limitations. Even in the case of a limited number of eigenstates, the L-K algorithm works well as long as the underlying coupling mechanism is direct.

It is also important to investigate how robust the L-K outputs are when the analysis is applied to experimental spectra where all the eigenstates are neither resolved nor above the noise floor. In order to simulate an experimental situation, a "filter" was applied to the set of eigenstates that resulted from diagonalization of the zero-order Hamiltonian. The eigenstates whose fractional bright state character was less than 0.01 were excluded from the computed synthetic absorption spectrum (Fig. 6-4).

This intensity filter radically altered the profile of the curve shown in Fig. 6-3. The skewness parameter was no longer a linear function of the difference between bright and doorway state energies. However, the magnitude and the sign of the skewness parameter were still correlated with the location of the doorway-state relative to the bright state (Fig. 6-5). The skewness parameter was negative when the energy of the doorway state was to the red of the bright state, went through zero when the doorway state was degenerate with the bright state, and became positive when the doorway state was tuned to the blue of the bright state. This was qualitatively distinct from the behavior observed when the skewness parameter was plotted for the case of direct coupling: the L-K output was essentially non-skewed for all direct model examples tested.

Although the power of the L-K analysis is compromised when it is applied to real spectra with limited resolution and dynamic range, the L-K algorithm remains a valuable tool for distinguishing between *doorway-mediated* vs. *direct* coupling schemes and for locating the J-value of the bright state / doorway state level crossing.

6.3 Application of the L-K Algorithm to Experimental Data

S_1 $3\nu_3$ level of acetylene is characterized by strong coupling to a background of dark states. "ν_3" denotes the trans-bending mode of acetylene in the first excited singlet state S_1. Drabbels, Heinze, and Meerts [35] have observed that the S_1 $3\nu_3$ level of acetylene is fractionated into a manifold of T_i states ($\sim$ 10 states/cm^{-1}) and Dupr'e *et al.*[43], in considering higher resolution Zeeman anticrossing (ZAC) and Zeeman quantum beat (ZQB) experiments, have observed a considerably more extensive fractionation into a denser manifold of S_o levels, presumably facilitated by $S_1 - T_i - S_o$ spin-orbit interactions. Since $S_o - T$ coupling is much weaker than $S_1 - T$ coupling, the effect on the fractionation patterns of the ground state S_o was only discernable at the higher resolution of ZAC and ZQB experiments [43]. In addition *ab initio* calculations [27] have shown that the energy minimum of the seam of intersection between the T_3 and S_1 surfaces occurs in the energy region of the S_1 $3\nu_3$ level. These findings suggest that a single ro-vibrational level of the T_3 state plays a unique doorway role in the spin-orbit interaction of S_1 $3\nu_3$ with the background manifold of $T_{1,2}$ states.

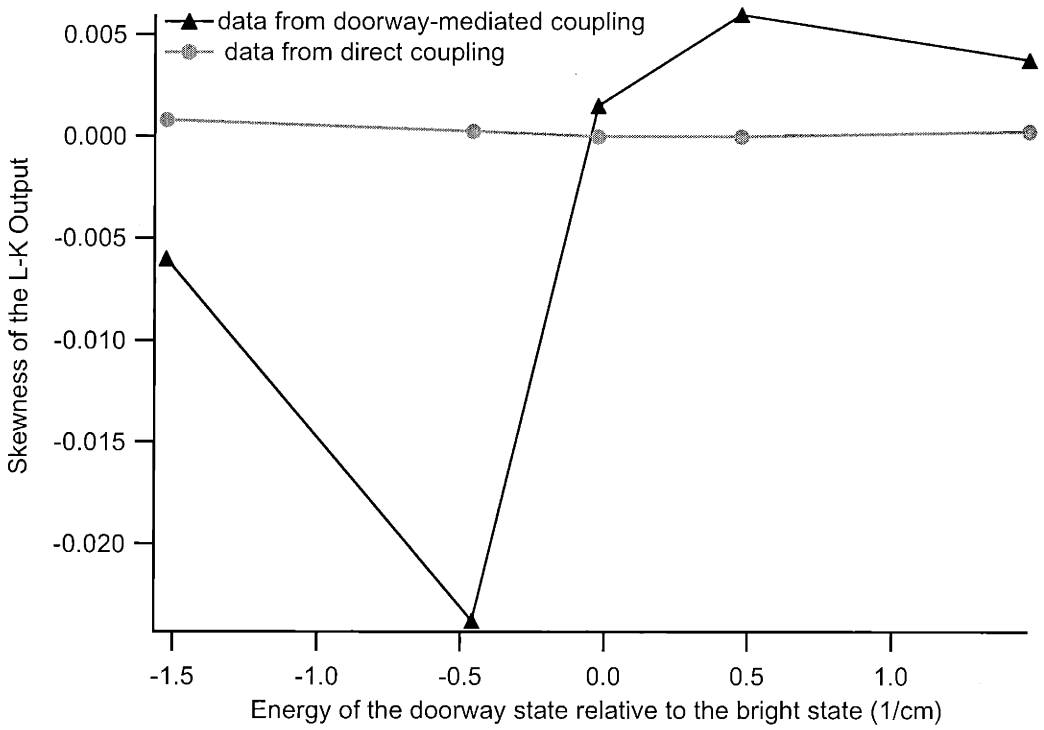

Figure 6-5: The skewness of the L-K output when the L-K algorithm is applied to simulated spectra subjected to an "intensity filter" which eliminates all eigenstates with fractional bright state character less than 0.01. This was done to demonstrate the utility of the L-K diagnostic in the case of spectra that do not possess eigenstate resolution. The doorway model still exhibits a clear trend in skewness as a function of the doorway state zero-order energy relative to the bright state energy, however the linearity of the line is compromised making it difficult to associate a slope with it which can be related to coupling matrix elements. However, there is a distinct difference in the skewness profile of the L-K output in the case of *doorway* vs. the *direct* model.

Table 6.1: The skewness of the L-K output for each group of eigenstates resolved in 18 MHz LIF spectrum

Assignment	Skewness
R(0) (J'=1)	-0.0062
R(1) (J'=2)	-0.0011
R(2) (J'=3)	0.00033571
R(3) (J'=4)	0.002

Therefore, acetylene S_1 $3\nu_3$ spectra were used to test how well the L-K algorithm would perform in uncovering a "non-standard" case of coupling when the input is real experimental data.

An L-K analysis was applied to an 18 MHz resolution laser-induced-fluorescence spectrum of the S_1 $3\nu_3$ band of acetylene recorded by Drabbels and coworkers who report that they resolve and detect all eigenstates with fractional bright state character greater than 0.01 in their spectrum [35]. The results are tabulated in Table 6.1.

There is a clear, monotonic trend in the evolution of the values of skewness vs. J. The fluctuations from zero are 10 times larger than those observed for the direct coupling case simulations. This result demonstrates that the coupling mechanism underlying this particular experimental spectrum is *doorway-mediated.* This conclusion has been confirmed by recent experiments as well [68]. This result also shows that as J increases the doorway state tunes from below and crosses the bright state in the vicinity of $J = 3$. This last conclusion is in agreement with recent data obtained from dispersed fluorescence experiments performed on the perturbed lines of the same band [29].

Obtaining Quantitative Parameters Using the L-K Approach

This section will demonstrate how a crude estimate for the rotational constant of the acetylene doorway state T_3 can be calculated by using the skewness data obtained

Table 6.2: The energy gap between rotational levels of the bright and doorway state as a function of $|\triangle B|$.

Rotational Level	S_1/T_3 Energy Gap
J'=1	$\|D\| + 2\|\triangle B\|$
J'=2	$\|D\| + 6\|\triangle B\|$
J'=3	$\|D\| + 12\|\triangle B\|$
J'=4	$\|D\| + 20\|\triangle B\|$

from the L-K analysis of Drabbels' high resolution UV-LIF data [35]. All units used in the following calculation are in cm^{-1}.

Suppose the difference in energy between the lowest rotational level of S_1 $3\nu_3$ and that of the doorway state T_3 is given by $|D|$. Since J is conserved in intersystem crossing, the energy gap between any rotational level J of the bright state S_1 and the corresponding rotational level of the doorway state T_3 will be given by

$$|E_{S_1} - E_{T_3}| = |D + J(J+1)\triangle B| \tag{6.11}$$

where $|\triangle B|$ is the difference between the rotational constants of S_1 $3\nu_3$ and the doorway state on T_3. Then, the energy gap between the rotational levels of the bright and doorway states can be tabulated as shown in Table 6.2.

The L-K skewness data obtained from Drabbels' high resolution UV-LIF spectrum [35] and presented in Table 6.1 suggests that the doorway state tunes through the bright state at $J' = 3$ since this is where the skewness becomes almost 0. Therefore, it can be assumed that $|D| - 12|\triangle B| = 0$. From the data presented in Table 6.1 we also know that the doorway state tunes from below the bright state since the sign of the skewness parameter starts out as negative, goes through zero, becomes positive. As was shown in the previous section, the evolution of the sign of the skewness parameter *can* be correlated with the direction of tuning of the doorway state. Therefore, the doorway state starts below the bright state, catches up with it because of its larger B constant, and tunes above it.

Table 6.3: Constructing a L-K skewness plot using a 18 MHz resolution UV-LIF data set.

Rotational Level	S_1/T_3 Energy Gap	Skewness
J'=1	-10 $\triangle B$	-0.0062
J'=2	-6 $\triangle B$	-0.0011
J'=3	0	0.00033571
J'=4	8 $\triangle B$	0.002

It is possible to associate a slope with the skewness data displayed in Table 6.1 plotted as a function of the energy difference between the bright state and the doorway state for each rotational level J. If we set $E_T - E_S = D$, which is a negative number, and $\triangle B = B_T - B_S$, which is positive, then we can tabulate the energies as shown in Table 6.3.

For each value of $\triangle B$, a slope of skewness can be associated with the data presented in Table 6.3. Therefore, a table of $\triangle B$ values vs. the corresponding slopes of skewness can be generated as displayed in Table 6.4.

To identify the correct value for $\triangle B$, we need to know which one is the correct slope to pick. From the L-K analysis, we know that the slope of skewness is approximately equal to the square of the coupling matrix element between the bright state and the doorway state (H_{bd}^2). Therefore, if we knew the magnitude of H_{bd}, we could find the value of $\triangle B$.

We know the doorway state tunes through the bright state at $J' = 3$. If we think of the bright state / doorway state system as a two level system (since the strongest interaction is between these two states), we would expect the UV-LIF spectrum to collapse into two clumps of approximately same intensity separated by $2H_{bd}$ at the energy of the $J' = 3$ rotational level. This is indeed the case as illustrated by a section of the UV-LIF spectrum displayed in Fig. 6-6.

Computing H_{bd} from the spectrum displayed in Fig. 6-6 yields a value of 0.122 cm^{-1}. Then, H_{bd}^2 is 0.015. When one looks up the value of $\triangle B$ which corresponds to

Table 6.4: Fitting the $\triangle B$ value

$\triangle B$ (cm^{-1})	Slope of Skewness
0.005	0.08116
0.01	0.04058
0.015	0.02705
0.02	0.02029
0.025	0.01623
0.026	0.01561
0.027	0.01503
0.03	0.01353
0.04	0.01015
0.06	0.00676
0.1	0.00406
0.14	0.0029
0.18	0.00225
0.22	0.00184

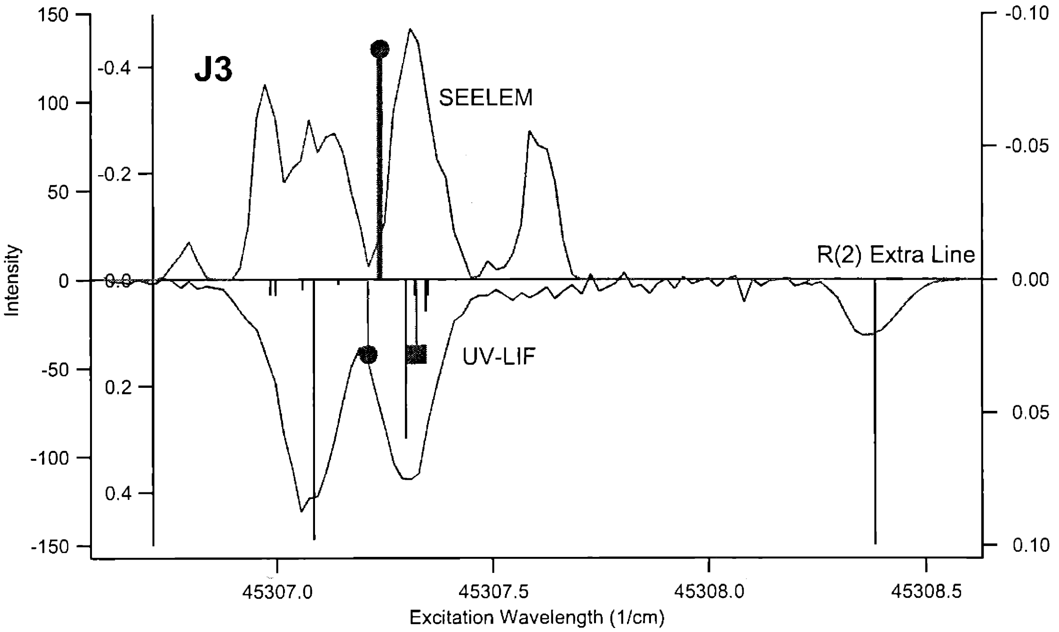

Figure 6-6: The UV-LIF and the corresponding SEELEM spectra showing the $J' = 3$ region of the $V_0^3 K_0^1$ transition of acetylene. The sticks represent the eigenstates resolved in the 18 MHz UV-LIF spectrum of the same transition recorded by Drabbels *et al.* [35]. The fractionation pattern of the $J' = 3$ line in the UV-LIF spectrum is characterized by two "clumps." Since the doorway state tunes through the bright state at $J' = 3$, it is assumed that the separation between the two clumps observed in the UV-LIF spectrum is $2H_{bd}$ where H_{bd} is the coupling matrix element between the bright state and the doorway state. The "extra" line shown in the spectrum arises from the interaction of the bright state with another perturbing state. The solid dot in the lower LIF trace denotes the location of the intensity-weighted average energy of the $J' = 3$ pattern without taking into consideration the extra line. The square denotes the location of the intensity-weighted average energy when the extra line is included.

a slope of skewness of 0.015, one finds the entry 0.027. Therefore, $\triangle B = 0.027$ and $B_T = B_S + 0.027$. In the case of acetylene, $B_S = 1.031$ cm^{-1} [35], and, hence, $B_T = 1.06$ cm^{-1}.

6.4 The Analytical Reason Behind the Empirical Finding of the L-K Approach

The empirical finding, that the slope of the line of skewness vs. doorway state energy in the L-K analysis is approximately equal to the square of the bright state ~ doorway state off-diagonal matrix element, will be shown in this section to be a general result by applying perturbation theory to a 3x3 matrix which contains three basis states: a bright state (S_1), a doorway state (T_3), and a background state (T_i).

$$\begin{array}{c} |S_1> \\ |T_3> \\ |T_i> \end{array} \begin{bmatrix} t_1 & V_1 & 0 \\ V_1 & t_2 & V_2 \\ 0 & V_2 & t_i \end{bmatrix}$$

Note that the bright state can couple to the background state only through the intermediary of the doorway state. Using results from perturbation theory, one can find expressions for the eigenstates and eigenenergies of the above matrix:

$$\begin{aligned}
E_{S_1} &= t_1 + \frac{V_1^2}{t_1 - t_2} \\
\Psi_{S_1} &= \alpha|S_1> + \frac{V_1}{t_1 - t_2}|T_3> + \frac{V_1 V_2}{(t_i - t_1)(t_2 - t_1)}|T_i> \\
E_{T_3} &= t_2 + \frac{V_1^2}{t_2 - t_1} + \frac{V_2^2}{t_2 - t_i} \\
\Psi_{T_3} &= \beta|T_3> + \frac{V_1}{t_2 - t_1}|S_1> + \frac{V_2}{(t_2 - t_i)}|T_i> \\
E_{T_i} &= t_i + \frac{V_2^2}{t_i - t_2} \\
\Psi_{T_i} &= \gamma|T_i> + \frac{V_2}{t_i - t_2}|T_3> + \frac{V_1 V_2}{(t_1 - t_i)(t_2 - t_i)}|S_1>
\end{aligned}$$

The Lawrance-Knight output function, B(E), which is derived in Ref. [83], can be expressed in terms of the real and imaginary parts of the Green's function for the zero-order state that carries the oscillator strength:

$$B(E) = \frac{Im\ G_{\alpha\alpha}(E)}{[Re\ G_{\alpha\alpha}(E)]^2 + [Im\ G_{\alpha\alpha}(E)]^2} \tag{6.13}$$

where,

$$\begin{aligned} Im\ G_{\alpha\alpha}(E) &= \sum_l |c_{\alpha l}|^2 \frac{\Gamma_l}{(\epsilon_l - E)^2 + \Gamma_l^2} \\ Re\ G_{\alpha\alpha}(E) &= \sum_l |c_{\alpha l}|^2 \frac{(\epsilon_l - E)}{(\epsilon_l - E)^2 + \Gamma_l^2} \end{aligned} \tag{6.14}$$

$G_{\alpha\alpha}$ is the Green's function for the bright state $|\alpha >$ in the above equations that is assumed to be coupled directly to a background of non-interacting states $|l >$. ϵ_l denotes the eigenenergy of the eigenstate $|l >$, $|c_{\alpha l}|^2$ denotes the fractional bright state character of the eigenstate $|l >$, and Γ_l corresponds to the lifetime of the state $|l >$.

$G_{\alpha\alpha}$ and, thus, B(E) can also be related to the zero-order parameters:

$$B(E) = \eta + \sum_\beta \frac{f_\beta^2\ \eta}{(\epsilon_\beta - E)^2 + \eta^2} \tag{6.15}$$

where η is a small phenomenological relaxation term, f_β is the coupling strength between a zero order state $|\beta >$ and the bright state, and ϵ_β is the zero-order energy of the state $|\beta >$. According to Eq.(6.15), the maxima of the function B(E) occur at the zero-order energies. Based on Eq.(6.13), the maxima of B(E) should occur when $Re\ G_{\alpha\alpha} = 0$:

$$B(E)_{maxima} = \frac{1}{Im\ G_{\alpha\alpha}} \tag{6.16}$$

Using Eq.(6.16), $B(E)_{maxima}$ for a doorway-coupling based Hamiltonian can be calculated:

$$\begin{aligned} B(E)_{maxima} &= \frac{V_1^4}{\Gamma\alpha^2(T_1-T_2)^2} \\ &+ \sum_i \frac{(t_1-t_i)^2(t_2-t_i)^2(\Gamma^2+\frac{V_i^4}{(t_i-t_2)^2})}{\Gamma V_1^2 V_i^2} \\ &+ \frac{(t_2-t_1)^2(\Gamma^2+(\frac{V_1^2}{t_2-t_1}+\sum_i \frac{V_i^2}{t_2-t_i})^2)}{\Gamma V_1^2} \end{aligned} \tag{6.17}$$

Each term in the summations and the first term in Eq.(6.17) represents a peak in the B(E) function at a zero-order energy T_i. One can expand $B(E)_{maxima}$ in terms of its most significant terms (*i.e.* those terms where the small relaxation parameter Γ is *not* in the denominator):

$$\begin{aligned} B(E)_{maxima} \approx & \frac{V_1^4}{\Gamma\alpha^2(T_1-T_2)^2} + \\ & \sum_i \frac{V_i^2(t_1-t_i)^2}{\Gamma V_1^2} + \\ & \frac{(t_2-t_1)^2(\frac{V_1^2}{t_2-t_1}+\sum_i \frac{V_i^2}{t_2-t_i})^2}{\Gamma V_1^2} \end{aligned} \tag{6.18}$$

In order to understand how the L-K skewness parameter relates to the zero-order coupling strength between the bright state and the doorway state, the L-K skewness parameter needs to be expressed in terms of B(E):

$$\begin{aligned} S &= \sum_i I_i^2 \times (E_i - E_0) \\ S &= \sum_i (\sqrt{\Gamma B(E_i)})^2 (E_i - t_1) \end{aligned} \tag{6.19}$$

since $I_i = \sqrt{\Gamma B(E_i)}$ and E_0, the zero-order energy of the bright state, is t_1. Substituting Eq.(6.18) into Eq.(6.19) and considering only the t_2 dependent terms, one finds,

$$\begin{aligned} S \approx V_1^2(t_2 - t_1) + \\ \frac{V_1^4}{\Gamma\alpha^2(t_1 - t_2)} + \\ 2(t_2 - t_1)^2 \sum_i \frac{V_i^2}{t_2 - t_i} + \\ \frac{(t_2 - t_1)^3}{V_1^2} (\sum_i \frac{V_i^2}{t_2 - t_i})^2 \end{aligned} \tag{6.20}$$

As can be seen, the slope of the L-K skewness as a function of $(t_2 - t_1)$, which is the energy difference between the bright state and the doorway state, is proportional to V_1^2, which is the square of the coupling matrix element between the bright state and the doorway state.

The perturbation theory justifies the behavior of the L-K skewness parameter when the difference between the energies of the doorway state and the bright state is larger than their coupling strength. However, we know that the L-K skewness parameter preserves its linearity even when the doorway state tunes through the bright state. Can we show that outside of the perturbation limit, the slope of the L-K skewness is still proportional to V_1^2?

In order to examine the behavior of the L-K skewness in the near degeneracy region, we need to pre-diagonalize the 2x2 matrix constructed from the bright state $|S_1>$ and the doorway state $|T_3>$:

$$\begin{array}{c} |S_1> \\ |T_3> \end{array} \begin{bmatrix} t_1 & V_1 \\ V_1 & t_2 \end{bmatrix}$$

The eigenenergies of this matrix are:

$$\begin{aligned} \lambda &= \frac{(t_1 + t_2) \mp \sqrt{(t_1 + t_2)^2 - 4(t_1 t_2 - V_1^2)}}{2} \\ E_1 &= \frac{(t_1 + t_2) + \alpha}{2} \\ E_2 &= \frac{(t_1 + t_2) - \alpha}{2} \\ \alpha &= \sqrt{(t_1 - t_2)^2 + 4V_1^2} \end{aligned}$$

And the corresponding eigenvectors are:

$$\begin{aligned}
|\epsilon_1> &= N_1 \begin{bmatrix} t_1 - t_2 + \alpha \\ 2V_1 \end{bmatrix} \\
N_1 &= \frac{1}{\sqrt{(t_1 - t_2 + \alpha)^2 + 4V_1^2}} \\
|\epsilon_2> &= N_2 \begin{bmatrix} t_1 - t_2 - \alpha \\ 2V_1 \end{bmatrix} \\
N_2 &= \frac{1}{\sqrt{(t_1 - t_2 - \alpha)^2 + 4V_1^2}}
\end{aligned}$$

The total Hamiltonian for the doorway-coupled system where the first two basis states are the prediagonalized states, looks like:

$$\begin{array}{c} |\epsilon_1> \\ |\epsilon_2> \\ |T_i> \\ \end{array} \begin{bmatrix} E_1 & 0 & x & \dots \\ 0 & E_2 & V_i & \dots \\ V_i & V_i & t_i & \dots \\ \vdots & \vdots & \vdots & \ddots \end{bmatrix}$$

Note that the only coupling matrix element in the total Hamiltonian which is 0 is between the first two basis states since they were pre-diagonalized. Now we can use perturbation theory to express the eigenenergies and the fractional $|S_1>$ bright state character of the eigenstates of this prediagonalized matrix. The energy of the predominantly bright state, $|\xi_1>$, will be given by:

$$\xi_1 = \frac{t_1 + t_2 + \alpha}{2} + \sum_i \frac{N_1^2 4V_1^2 V_i^2}{\frac{t_1+t_2+\alpha-2t_i}{2}} \tag{6.23}$$

which can be further simplified since:

$$\begin{aligned}
\sum_i \frac{N_1^2 4V_1^2 V_i^2}{\frac{t_1+t_2+\alpha-2t_i}{2}} &= N_1 \, (t_1 - t_2 + \alpha) < S_1| + 2V_1 N_1 < T_3|H_{SO}|T_i> \\
&= 2N_1 V_1 \ < T_3|H_{SO}|T_i> \approx \ 2V_1 V_i N_1
\end{aligned} \tag{6.24}$$

and, hence,

$$\xi_1 = \frac{t_1 + t_2 + \alpha}{2} + 2V_1 V_i N_1 \tag{6.25}$$

The fractional $|S_1>$ bright state character of $|\xi_1>$ will be:

$$C_{S_1} = (t_1 - t_2 + \alpha)N_1 \tag{6.26}$$

The eigenenergy and fractional $|S_1>$ bright state character of the predominanly doorway state, $|\xi_2>$, will be:

$$\begin{aligned} \xi_2 &= \frac{t_1 + t_2 - \alpha}{2} + \sum_i \frac{N_2^2 4 V_1^2 V_i^2}{\frac{t_1+t_2-\alpha\ 2t_i}{2}} \\ C'_{S_1} &= (t_1 - t_2 - \alpha)N_2 \end{aligned} \tag{6.27}$$

And for the state $|\xi_i>$ which has predominantly background $|T_i>$ character:

$$\begin{aligned} \xi_i &= t_i + \frac{N_1^2 4 V_1^2 V_i^2}{\frac{t_1+t_2+\alpha-2t_i}{2}} + \frac{N_2^2 4 V_1^2 V_i^2}{\frac{t_1+t_2-\alpha-2t_i}{2}} \\ C''_{S_1} &= \frac{4N_1^2 V_1 V_i (t_1 - t_2 + \alpha)}{t_1 + t_2 + \alpha - 2t_i} + \frac{4N_2^2 V_1 V_i (t_1 - t_2 - \alpha)}{t_1 + t_2 - \alpha - 2t_i} \end{aligned} \tag{6.28}$$

Using the expressions derived above and Eq.(6.16), we can write the maxima of the L-K output function B(E) in terms of the zero-order parameters.

$$\begin{aligned} B(E)_{maxima} &= \frac{1}{\Gamma} \sum_i \frac{(t_i - t_1)^2 V_i^2}{V_1^2} \\ &\quad + B_1 + B_2 \end{aligned} \tag{6.29}$$

where B_1 and B_2 denote the t_2 dependent terms:

$$\begin{aligned} B_1 &= \frac{\Gamma^2 + (-t_1 + \frac{1}{2}(\alpha + t_1 + t_2) + \sum_i (\frac{N_1^2 4 V_1^2 V_i^2}{t_1+t_2+\alpha-t_i}))^2}{\Gamma N_1^2 (\alpha + t_1 - t_2)^2} \\ B_2 &= \frac{\Gamma^2 + \frac{1}{4}(\alpha - t_1 + t_2 - 2\sum_i (\frac{N_2^2 4 V_1^2 V_i^2}{t_1+t_2-\alpha-t_i}))^2}{\Gamma N_2^2 (\alpha - t_1 + t_2)^2} \end{aligned} \tag{6.30}$$

A heroic attempt at simplifying the L-K skewness expression incorporating the rigorously calculated $B(E)_{maxima}$ equation yields a term which is proportional to V_1^2, where V_1 is the coupling strength between the bright state and the doorway state, and linear in $t_2 - t_1$, which is the energy difference between the bright state and the doorway state:

$$S \sim 4\, V_1^2(t_2 - t_1) \left[\frac{\sum_i \frac{V_i^2}{t_1+t_2+\alpha-t_i}}{\alpha + t_1 - t_2} - \frac{\sum_i \frac{V_i^2}{t_1+t_2-\alpha-t_i}}{\alpha - t_1 + t_2} \right] \tag{6.31}$$

This completes the rigorous analysis of the empirical finding that the slope of the L-K skewness as a function of $\triangle E_{bright-doorway}$ is proportional to $H^2_{bright\sim doorway}$.

6.5 Conclusion

We have demonstrated a new capability of the L-K deconvolution procedure. As presented in this paper, an "assumption-violating" application of the L-K algorithm to experimental spectra can distinguish between *doorway-mediated* vs. *direct* coupling mechanisms. In the case of doorway-mediated coupling, the L-K output exhibits significant skewness. It is possible that higher order moments of the L-K output function could be indicative of more elaborate coupling schemes where there is a hierarchy of doorway states mediating the coupling. This L-K approach, especially when it is applied to a series of J-sorted spectra, is presented as a powerful and easy-to-implement tool for uncovering the dynamics encoded in complex spectra. The quality of the information extracted by the L-K approach is significantly enhanced as the resolution and the dynamic range of the J-sorted spectra are improved. The dynamic range is determined by the noise floor of the experimental spectrum and sets a limit on the weakest detectable peak. It is directly correlated with the number of eigenstates that are resolved from the spectrum and input into the L-K algorithm and, hence, translates into the number of Lorentzian curves that are obtained in the output. The larger the number of Lorentzian curves, the more accurate the L-K skewness parameter will be.

An accurate J-sorting algorithm is also crucial. The unique fractionation pattern that belongs to a single $J' \leftarrow J''$ rotational transition must be identified correctly even in cases where that pattern overlaps with other patterns in the spectra. Failure to identify all components (especially outliers) and to associate each component with the correct $J' \leftarrow J''$ rotational transition will corrupt the L-K skewness parameter, and consequently, result in inaccurate conclusions about the coupling mechanism and strengths.

It is possible to obtain crude estimates of the coupling matrix element between the bright state and the doorway state, H_{bd}, or $\triangle B_{bd}$, which is the difference in the rotational constants of the bright and dark states, from the L-K skewness plot provided that one of these parameters is already known from a separate analysis. This was outlined in Subsection 6.3: If $\triangle B_{bd}$ is known, then the energy gap between the bright state and the dark state is known as a function of J, and the slope of the L-K skewness plot can be directly correlated to H_{bd} (the slope of the L-K skewness plot is proportional to the square of H_{bd}). If H_{bd} is known, then $\triangle B_{bd}$ can be obtained by a fit where the $\triangle B_{bd}$ value that yields a slope equal to the square of H_{bd} for the L-K skewness plot is picked. Therefore, in addition to providing qualitative information about coupling mechanisms, the L-K algorithm can also be used to deduce key molecular parameters.

Chapter 7

Infrared Emission

This chapter includes a description of the mechanism and significance of the near infrared (0.8 - 1.7 μm) component of the laser-induced fluorescence that results from exciting in the neighborhood of the $\tilde{A}^1A_u \leftarrow \tilde{X}^1\Sigma_g^+$ transitions of C_2H_2. The IR signal has a non-linear dependence on laser intensity. The source of the IR fluorescence is an electronically excited photofragment which is produced by photodissociation of the parent molecule in a two-photon process mediated by either singlet or triplet predissociated spin-rovibronic states. The two-photon process is resonance enhanced at the one-photon level. Experimental findings so far suggest that the IR-emitting photofragment is C_2H.

The IR component of the fluorescence was first discovered in cell experiments where rotationally resolved fluorescence excitation spectra of the $\tilde{A}^1A_u \leftarrow \tilde{X}^1\Sigma_g^+$ transition of C_2H_2 were recorded. The IR signal was observed again in our exploratory supersonic-jet experiments on the triplet states of acetylene. The significance of the IR signal stems from the fact that it should be possible to exploit it to probe the triplet perturbers of the $\tilde{A}^1A_u$ state of acetylene. The eigenstates of mixed singlet$\sim$triplet character produced at the one-photon level serve as intermediate steps in a predissociated $RH^{**} \leftarrow h\nu_2 + S_1 \leftarrow h\nu_1 + S_0$ transition. RH^{**} denotes the two-photon excited, predissociated state of the parent molecule RH. Resonance enhancement of the IR fluorescence at both the one- and two-photon levels in a two-color experiment would exploit a selectable state (*i.e.* a Rydberg state) at the two-photon level with *either* singlet or triplet character. The ability to select two-photon excited states with specific multiplicity would permit independent measurements of the triplet and singlet characters of the eigenstates accessed at the one-photon level. Therefore, the two color IR-LIF scheme could be a sensitive, selective, and diagnostically rich scheme that would have general applicability in the study of triplet states in acetylene and other unsaturated molecules.

7.1 First Observation of the IR Signal in Cell Experiments

The near IR component of the fluorescence that results from exciting the $\tilde{A}^1A_u \leftarrow \tilde{X}^1\Sigma_g^+$ transition of C_2H_2 was first observed in cell experiments [37]. In those experiments, UV- and IR- detected fluorescence excitation spectra of the $V_0^2K_0^1$ and $V_0^3K_0^1$ subbands were recorded (V represents the *trans*-bending mode, ν_4'' in the $\tilde{X}$ state and ν_3' in the $\tilde{A}$ state). The non-linear dependence of the IR signal on laser power was the first evidence that suggested the IR signal was a result of a multiphoton event. The intensity ratios of the UV- and IR-detected spectra were also different for the two subbands. Guided by these observations, the following conclusions were drawn regarding the observed IR emission:

1) The source of the IR emission is likely to be C_2H photofragments. A dissociation mechanism that produces C_2H, suggested by the work of Ito *et al.* [135], involves a two-photon excitation scheme which populates Rydberg states of the parent C_2H_2 molecule via an $\tilde{A}$-state $\nu_3 = 3$ resonant intermediate. These Rydberg states are reported to have predissociation lifetimes shorter than 1 ps [62, 92] and they decay to long-lived ($\sim$ 5 - 20 μs) $C_2H^* + H$ species [62]. C_2H^*, in turn, is known to fluoresce in the 1 - 2 μm region. This emission has been assigned to the $\tilde{A} \rightarrow \tilde{X}$ transition [113].

2) Alternatively, the carrier of the IR emission could be intact acetylene molecules. The eigenstates with significant $T_n(cis)$ character prepared initially in the excitation

of the $\tilde{A} \leftarrow \tilde{X}$ transition could give rise to near IR emission via $T_n(cis) \rightarrow T_1(cis)$ electronic transitions, which are expected to occur in the 1 - 2 μm region on the basis of *ab initio* calculations [111, 141, 93] [1]. IR emission originating from intact acetylene would have a linear dependence on laser power. Fits to IR intensity, I, vs. laser power, P, that were of the form $I = a \times P + b \times P^2$, yielded polynomials with both linear and quadratic terms. Since the resulting fit parameters were highly correlated, it was difficult to assess the relative contributions to IR signal of intact vs. photofragment species based on the data from cell experiments.

3) It was observed in the cell experiments that the IR:UV intensity ratio changes as a function of J, the total rotational angular momentum quantum number, in the $\tilde{A} - \tilde{X}$ $V_0^3K_0^1$ subband, but this ratio was found to be independent of J throughout the $V_0^2K_0^1$ subband. These two observations may be interpreted by considering the possible contribution of the triplet eigenstate character to the IR signal. In other words, in the case of the $V_0^3K_0^1$ subband, dissociation from the one-photon excited states by absorption of a second UV photon, could either be a triplet-mediated or a singlet-mediated process since this subband is characterized by numerous strong triplet perturbers. Dissociation via the $V_0^2K_0^1$ subband, in contrast, is exclusively a singlet-mediated process and depends only on the $\tilde{A}$ state singlet character of the initially excited eigenstates. Hence, the feature by feature intensities of the IR signals from the $V_0^2K_0^1$ subband are expected to follow those of the UV signals within a constant proportionality factor. There are no significant triplet perturbations in the $\tilde{A}$ $2\nu_3$ level. This explains why the IR:UV intensity ratio does *not* change as a function

---

[1] In fact, Wendt *et al.* have observed the absorption spectrum in the gas phase of the metastable $^3B_2$ (T_1 *cis* well) state of acetylene [146]. The metastable state in their experiments was generated by Hg-photosensitization. The mechanism for this is believed to be,

$$Hg(^1S) + h\nu \rightarrow Hg(^3P_1)$$
$$Hg(^3P_1) + M \rightarrow Hg(^3P_0)$$
$$Hg(^3P_0) + C_2H_2 \rightarrow Hg(^1S) +^3 C_2H_2^*$$

They found that the absorption spectrum of the 1^3A_2 - 1^3B_2 transition of acetylene has its 0_0^0 origin near 1.35μm.

of J in the $V_0^2K_0^1$ subband.

Although the conclusions from the results of cell experiments were interesting, they had to be re-evaluated based on the new data obtained in the molecular beam experiments (Figs. 7-1 and 7-2). Failure to observe significant J-dependent variations in the IR:UV intensity ratios of the rotational lines resolved in the spectrum of the $V_0^3K_0^1$ subband obtained in a molecular beam experiment, suggested that the gating scheme employed in the cell experiments to collect UV fluorescence could have led to the erroneous conclusion that the IR:UV intensity ratio was J-dependent. In the cell experiments, UV fluorescence was collected over a very short time window (10 ns gate width at the peak of the signal as opposed to the 2 μs gate width used in molecular beam experiments). IR fluorescence, in contrast, was collected by integrating over a wide window ($>$ 10 μs) at the peak of the IR signal. Unlike the UV fluorescence signal, the temporal profile of the IR signal was governed by the response time of the IR detector (τ = 100 - 200 μs). Therefore, regardless of the lifetimes of the emitting states, all IR fluorescence signals observed had the same temporal profile. The photomultiplier tube, which collects the UV fluorescence, has a response time of only a few nanoseconds [1], therefore the temporal profile of the UV fluorescence signal reflects intrinsic intra-molecular relaxation processes.

Since the $V_0^3K_0^1$ eigenstates have longer lifetimes than the $V_0^2K_0^1$ states, due to their relatively smaller singlet character, a short gate window for the UV fluorescence signal could under-sample the total signal from the emitting eigenstates in the case of the $V_0^3K_0^1$ subband. In other words, the gating scheme could introduce a bias toward states with larger S_1 bright state character. The fluctuations of the IR:UV intensity ratio as a function of J could be merely a consequence of the different lifetimes (*i.e.* fractional S_1 characters) of the states belonging to different J's. In the case of the $V_0^2K_0^1$ spectrum, most UV-active eigenstates would be expected to have similar and short lifetimes due to absence of triplet perturbers, and, therefore, an equal and significant fraction of the total UV fluorescence would be collected from the emitting states even with a short gate width.

The fact that eigenstates with short lifetimes tend to appear as stronger peaks

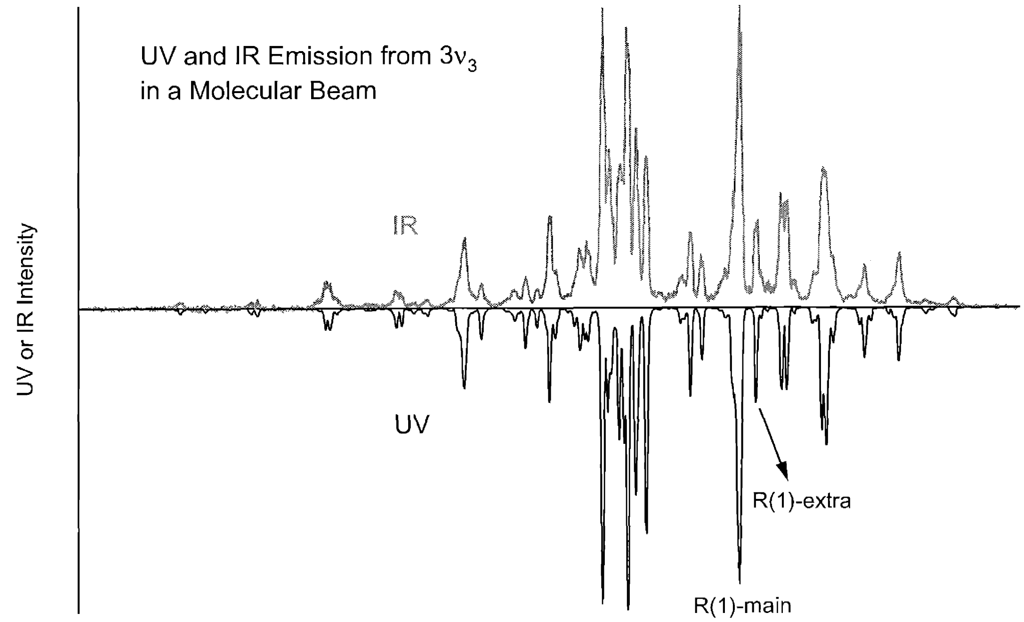

Figure 7-1: UV and IR components of the fluorescence from the excitation of the $\tilde{A} - \tilde{X}$ $V_0^3K_0^1$ subband of acetylene in a molecular beam. The IR:UV peak intensity ratios are *not* J-dependent.

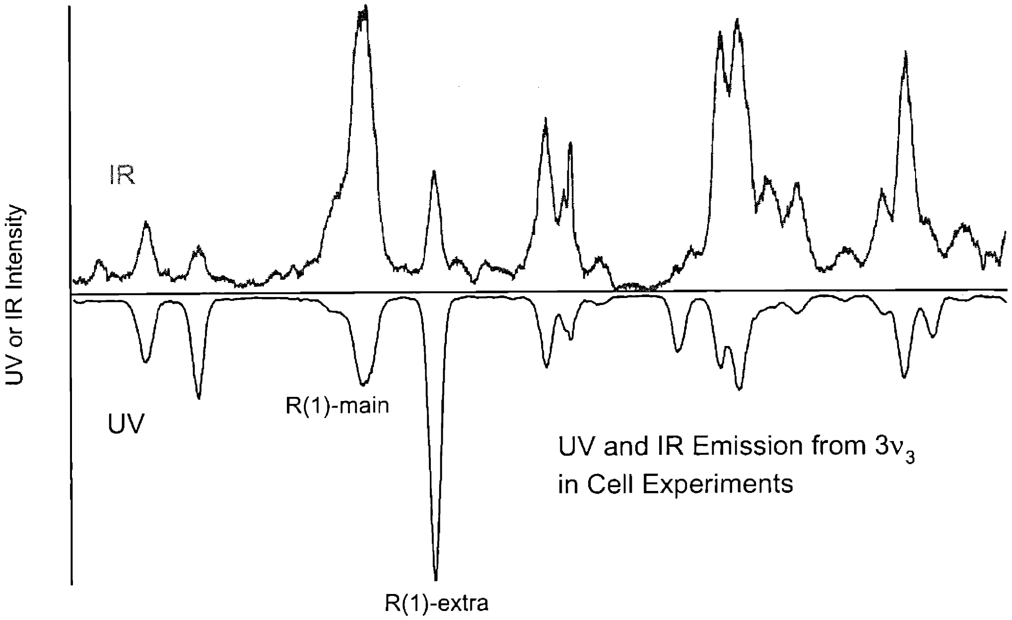

Figure 7-2: UV and IR components of the fluorescence from the excitation of the $\tilde{A} - \tilde{X}$ $V_0^3K_0^1$ subband of acetylene recorded in a cell experiment. The IR:UV peak intensity ratios *are* J-dependent.

in the UV LIF spectra collected in cell experiments is also reflected in the intensity ratios of "main" vs. "extra" lines in the $V_0^3K_0^1$ subband. Extra lines are due to an S_1 anharmonic perturber of $3\nu_3$ which has been identified as $4\nu_b$ [140], where ν_b represents a polyad comprised of ν_4' (torsion) and ν_6' (antisymmetric in-plane bend). Extra lines have characteristically shorter radiative lifetimes than the main lines of $3\nu_3$ which have relatively large triplet character. The extra levels are shown by Ochi and Tsuchiya to be relatively less perturbed by triplet states [105]. Spectra collected in cell experiments exhibit anomalously stronger signals from extra lines relative to the main lines. In a molecular beam, however, the trend is reversed: the extra lines appear weaker. The R(1) main and extra lines are labelled for comparison in the cell and molecular beam spectra to show the striking difference in their intensity ratios (Figs. 7-1 and 7-2).

It should be noted that the cell experiments were performed with 150 mT of acetylene. This pressure corresponds to an average time between collisions of 0.2 μs (estimated using a pressure broadening coefficient of 10 MHz/Torr [13]). The lifetimes of UV-active eigenstates in the $V_0^3K_0^1$ subband have been measured in molecular beam experiments to be in the region of $1-2\mu$s (Chapter 3). Therefore, in the cell experiments, the excited states would undergo a few collisions during the timescale of their radiative decay. This suggests that collision-induced relaxation could also cause under-sampling of the total UV fluorescence from the $3\nu_3$ states. Collision-induced quenching would not affect the IR signal in the same way as it does the UV signal because the IR signal arises from a multiphoton effect and, therefore, any population promoted to the intermediate state in the multiphoton process is immediately excited to the predissociated Rydberg state which couples into the photodissociation manifold. In both jet and cell experiments, the time available for the absorption of the second photon is about 6 ns (pulse width of the laser), which is too short for collisions to have any effect on the singlet vs. triplet contributions to the two-photon part of the IR signal.

As mentioned previously, we believe that the source of the IR signal is electronically excited C_2H photofragments produced via Rydberg state pre-dissociation. The most important pieces of information we have which suggest that C_2H photofragments are the main carriers of the IR signal are:

1) The IR signal has a non-linear dependence on laser power in high intensity (*i.e.* focussed) laser light regimes.

2) The dissociation energy of C_2H_2 is low enough (46074 cm^{-1}) [99] that two photons of all excitation wavelengths at which IR signal has been observed (origin band, $1\nu_3$, $2\nu_3$, $3\nu_3$, and $4\nu_3$ of the *trans* well of the $\tilde{A}$ state of acetylene) would be sufficient to generate electronically excited C_2H photofragments. Production of other photofragment candidates such as $C_2 + 2H$ and $C_2 + H_2$ would be energetically feasible only at higher excitation frequencies (85462 cm^{-1} and 49346 cm^{-1}) [29, 96].

3) In the first-generation apparatus, a *metastable photofragment* peak was observed in the SEELEM time-of-flight spectra when Cs was used as the detector surface [29]. The metastable photofragment signal disappeared when Au was used as the SEELEM surface. Based on *ab initio* calculations performed on C_2H by Cui and Morokuma and by DuFlot *et al.* [25, 38], there is a metastable state of C_2H ($1\ {}^4\Sigma^+$) which lies at $\sim$ 2.7 eV. This state would be detectable on Cs, but not on Au or Cu. Hence, two-photon generation of excited, IR-active C_2H photofragments could also explain the observation of this metastable signal on Cs.

4)Although intact acetylene molecules with a large T_n fractional character undergoing spontaneous fluorescence decay within the triplet manifold ($T_n \rightarrow T_1$) could also give rise to IR emission, it is much more likely that the carriers of the IR signal in both cell and jet experiments are the C_2H photofragments. If the IR signal did arise from intact acetylene molecules with large triplet character, then certainly one would expect a significant variation in the strength of the IR signal as one scanned through the different vibrational bands of the acetylene $\tilde{A}^1A_u \leftarrow \tilde{X}^1\Sigma_g^+$ transition. Different bands associated with this transition are characterized by different degrees of coupling to the background manifold of triplet states. The strongest IR signal would be expected to be observed in the $3\nu_3$ level, which is known to be most strongly coupled to the background manifold of triplet states [43, 40, 41, 42, 68]. However, the $2\nu_3$ and $4\nu_3$ levels are also characterized by strong IR signals.

Another problem associated with the intact acetylene idea is that if metastable states with large fractional T_n character were the sources of the IR emission, then the intensity profile in the IR signal would not follow that of the UV (C_2H_2 $\tilde{A} \rightarrow \tilde{X}$) signal, as it does very faithfully in all the cold-band spectra acquired (see Section 7.3 for an exception).

Finally, $T_{2,3} \rightarrow T_1$ transitions are only electronically allowed for the *cis*-isomer of acetylene. Since the initial excitation is to the *trans*-well of the $\tilde{A}$ state, the intact acetylene idea would also require the presence of some mechanism which leads to the population of the *cis*-well triplets from the *trans*-well S_1 state.

7.2 IR Signal in Molecular Beam Experiments

Since transitions giving rise to the IR fluorescence spectra are excited and detected in the source chamber of the second-generation apparatus, the background pressure conditions for these spectra are identical to those of the first-generation apparatus ($2 * 10^{-5}$ Torr). The only significant difference between the IR spectra collected in the first-generation apparatus and the second-generation apparatus is the type of IR detector used. The IR detector used in the first-generation apparatus had a time constant of 0.1 - 0.2 ms (Edinburgh Instruments, EI-A Germanium detection system) whereas the IR detector used in the second-generation apparatus had a time constant of 8 - 10 μs (Edinburgh Insturments, EI-S Germanium detection system). However, since both time constants are too long to perform reliable lifetime measurements on the IR-emitting states (the lifetime of the low lying excited electronic state of C_2H, from which emissions to the ground electronic state occur in the near-IR, is 5 - 20 μs [37]), no such lifetime measurements were carried out. The difference between the time constants for the two detectors should be of no consequence in recording IR LIF spectra and determining the dependence of the IR signal on laser power. Therefore, IR-LIF data acquired in the two chambers are directly comparable. This is in contrast to the situation for SEELEM spectra, which are tremendously affected by the background pressure and, hence, are not comparable between the first and second-generation chambers (Chapter 4).

One of the most important characteristics of the IR signal is its non-linear dependence on laser power. Whereas the UV signal exhibits a linear dependence on laser power [2], the profile of the IR signal as a function of laser power deviates from linearity (Fig. 7-3). In fact, a fit of the IR signal vs. laser power to a polynomial of the form $I = a \times P^n$ yields an exponent of 1.67(6) [3] [29]. The non-linear dependence has been observed in both the cell experiments and the molecular beam experiments. It was this observation which suggested that the IR signal was arising from a multi-photon event. However, in every case that the non-linear dependence was observed, the laser beam was focussed to a small spot (~0.7 - 1 mm in diameter). Focussing the laser beam was observed to enhance the IR signal significantly. This is expected since focussing the laser beam gives rise to high intensity, and hence, should increase contribution to the signal from multiphoton processes.

An interesting finding from multiphoton spectroscopy of molecules reported by Lin *et al.* [89] is that the yields from multiphoton processes achieved with highly focussed laser beams can be proportional to $I^{3/2}$, where I is the laser intensity, or in some cases to noninteger powers of I that are not relevant to the intrinsic intensity dependence. The noninteger power dependence arises from geometrical effects of focussing on the laser beam in the region of molecule-photon interaction. The $I^{3/2}$ dependence was first observed experimentally and has been theoretically investigated [7, 128, 129]. Since our IR signal is proportional to $I^{1.67}$, it is possible that this

---

[2] Based on the two-photon destruction mechanism, one would in fact expect the UV signal to increase slower than linearly with laser intensity since the two-photon process should be depleting the intermediate level populations, *i.e.* sources of the UV signal, at an increasing rate with increasing laser intensity. However, this subtle effect has not been observed in our signal vs. intensity data for UV signal. This means that this effect is either too small to observe, or that the two-photon process occurs via the "triplet-mediated" pathway. The intermediate states which play a role in the triplet-mediated photodissociation (*i.e.* states of large fractional triplet character) are not expected to contribute to the UV-signal significantly, and, hence, the UV-signal may not be sensitive to the fluctuations in the populations of these states.

[3] When the fit was attempted with a polynomial of the form $I = a + b \times P + c \times P^2$, the coefficients of the linear and quadratic terms of the best-fit polynomial were b=-0.14 and c=0.018.

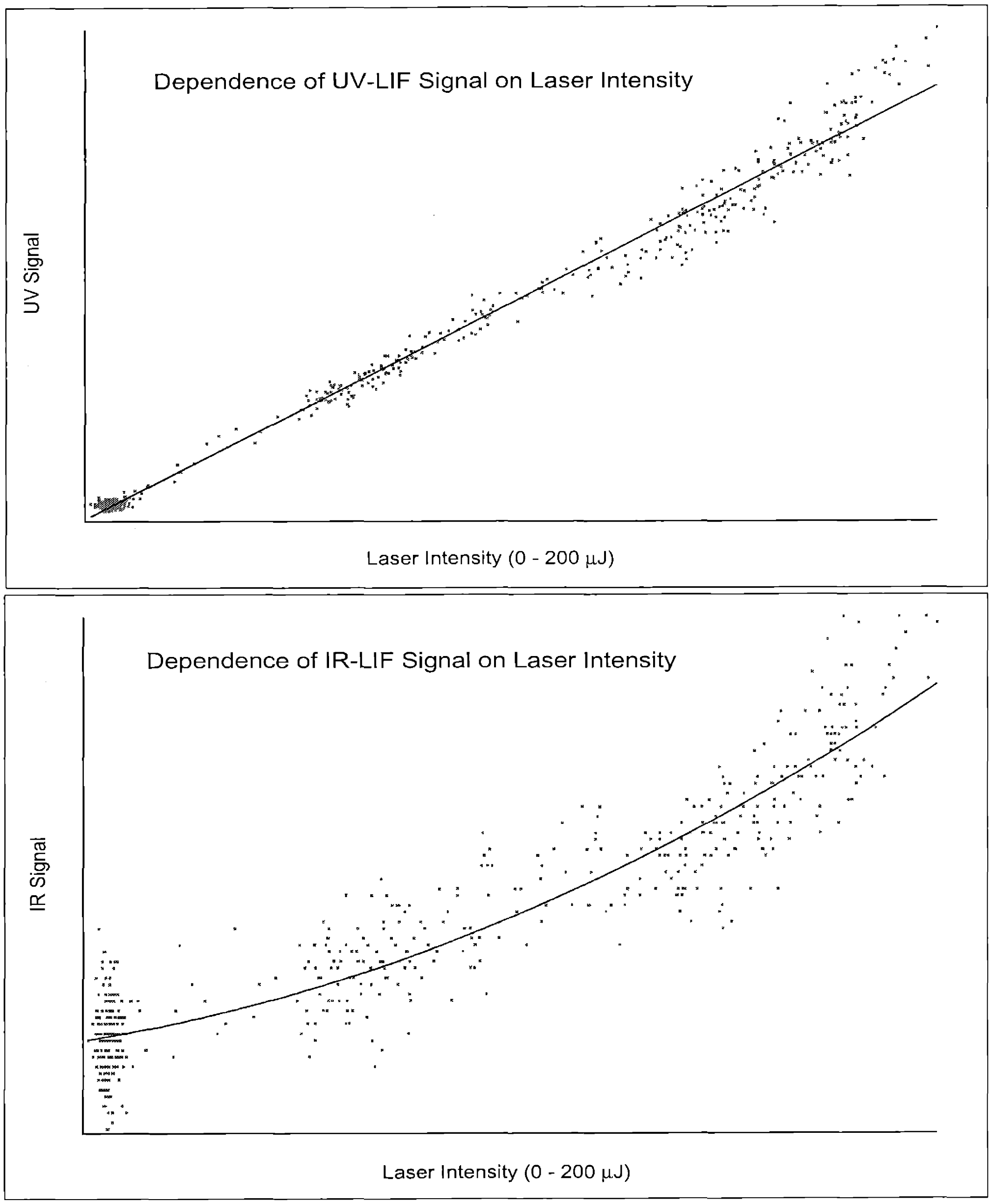

Figure 7-3: The dependence on laser intensity of the UV and IR components of the fluorescence from the R(1) line in the $V_0^3K_0^1$ subband of acetylene. The IR signal has a non-linear dependence on laser intensity, whereas the UV signal has a linear dependence. Data were collected with a tightly focussed laser beam (0.7 mm diameter).

dependence is attributable to the focussing of the laser beam. $I^{3/2}$ dependence is observed if the laser intensity exceeds a critical value and the saturation condition is satisfied *only* in a restricted region of the interaction volume. As the focus becomes tighter, the intensity goes up ($I \propto d^{-2}$ where d is the diameter of the beam) and the number of molecules in the focal region decreases (volume of focal region $\propto d^2 \propto$ no of molecules).

A simple calculation reveals the regime (saturation vs. non-saturation) at our typical laser power: We typically excite our molecules with 300 − 200μJ of laser light/pulse at 220 nm. We focus the beam to a ~ 1 mm diameter. This yields the following flux:

$$\begin{aligned} F &= \frac{\#\text{ of photons}}{\text{sec} * \text{cm}^2} \\ \#\text{ of photons} &= \frac{300 * 10^{-6}\text{J} * 220 * 10^{-7}\text{cm}}{6.626 * 10^{-34}\text{J.s} * 3 * 10^{10}\text{cm/s}} \\ F &\approx \frac{3.3 * 10^{14}}{6 * 10^{-9}\text{s} * 0.008\text{cm}^2} \\ F &\approx 7 * 10^{24}\text{photons}{*}\text{s}^{-1} * \text{cm}^{-2} \end{aligned} \tag{7.2}$$

We excite our molecules 40 nozzle diameters downstream from the nozzle (orifice diameter = 0.5 mm). It is possible to calculate various parameters of a jet expansion such as its density, temperature, Mach number, *etc.* at different points relative to the nozzle, given a set of reservoir conditions [4]. Based on calculations done for a He expansion, we can estimate the density of our molecular beam 40 nozzle diameters downstream from the nozzle as 10^{17} molecules /cm^3 [97]. The absorption coefficient for the $\tilde{A} - \tilde{X}$ $V_0^3 K_0^1$ subband (*i.e.* the first step in the multiphoton absorption process) has been measured by Ingold and King as 0.04 cm^{-1} [69]. In order to obtain the absorption cross-section, one needs to divide the absorption coefficient by the density of absorbers since,

---

[4] "Reservoir conditions" refer to the backing pressure and temperature of the gas to be expanded.

$$\kappa(\nu)(cm^{-1}) = N(cm^{-3}) \times \sigma(\nu)(cm^2) \tag{7.3}$$

In the cell experiment performed by Ingold and King, the density of absorbers was 3.76×10^{19} cm^{-3} [69]. Therefore, $\sigma = 1 \times 10^{-21}$ cm^2 for the acetylene $S_1\ 3\nu_3 \leftarrow S_0, \nu = 0$ transition. We can calculate a transition rate constant for the first step of the multiphoton process:

$$k = \sigma \times I \tag{7.4}$$

where σ is the absorption cross section in cm^2 and I is laser flux in photons$\times$s$^{-1}\times$cm^{-2}. The transition rate for the first step is 7×10^3 s^{-1}. Unfortunately, there have not been any measurements of absorption cross sections from intermediate states to Rydberg states in acetylene [5], therefore we cannot estimate the transition rate for the second step of the multiphoton process. However, we already have experimental data which shows that the absorption of a second photon that promotes population from the intermediate state to the wings of a predissociated Rydberg state, is a favored process. Therefore, it is expected that the second step in this multiphoton process, especially on resonance, will have a much larger absorption cross-section and much faster transition rate than the first step.

The laser pulse length, t_p, in our experiments is 5 - 7 ns. Therefore, $k * t_p \ll 1$ (where $k = 7 \times 10^3$ s^{-1}) for the first step. For laser intensities at which the second step of the multiphoton process also satisfies this condition, we will be in the non-saturation regime [89]. At higher fluxes where $k * t_p \geq 1$ for at least one of the one-photon events, saturation effects will set in.

Since it was desirable to acquire IR-LIF and SEELEM spectra simultaneously and since the SEELEM signal is maximized when the laser beam is unfocussed so as to obtain a large molecule/light interaction region, it was of interest to observe the effect on IR signal when the laser beam was made slightly larger (3-4 mm in diameter). Unfortunately, the IR signal was significantly reduced. However, the

---

[5] There have been two-photon absorption studies done in the 3p Rydberg energy region (72000 - 78000 cm^{-1}) of acetylene by Ashfold *et al.* and Takahashi *et al.*. These studies report the energies of the 3p Rydberg states and their geometry [8, 136].

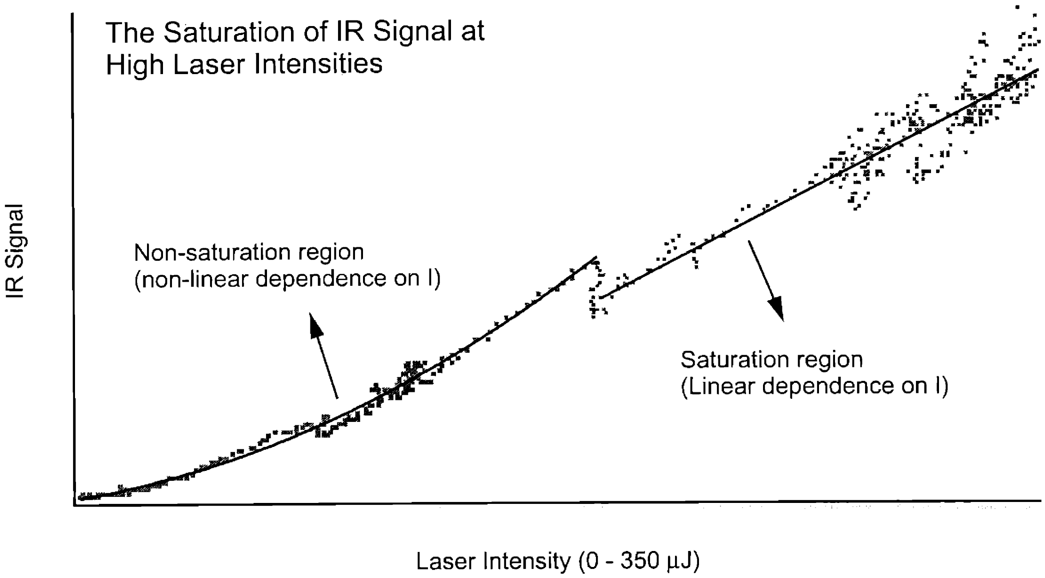

Figure 7-4: The laser intensity dependence of the IR signal becomes "bi-modal" when a loosely focussed laser beam is used. The non-saturation and saturation regimes are clearly identified by the different dependence of the IR signal on laser intensity. The kink seen in the data which coincides with the transition from one regime to the other, is attributed to a glitch in the data collection electronics.

power dependence of the signal also changed and became "bi-modal"(Fig. 7-4). In other words, the IR signal had a non-linear dependence on the laser intensity at low fluence (*i.e.* non-saturation regime) and the dependence switched to linear at high fluence (*i.e.* saturation regime).

The data displayed in Fig. 7-4 can be used to compute a lower-limit estimate of the absorption cross section for the second step of the multiphoton process: the transition from the intermediate level to the Lorentzian wing of a predissociated Rydberg state. For absorptions with fast enough transition rates such that $k * t_p \geq 1$ where t_p is the duration of the laser pulse, saturation becomes important [89]. We can assume that at a flux of $1 * 10^{24}$ photons*cm^{-2}*s^{-1}, where the switch from non-saturation to saturation has been observed to occur, $k * t_p = 1$ for the second step. Then one can calculate that $k = 1.7 * 10^8$ s^{-1} for this step ($t_p \approx 6 * 10^{-9}$ ns). This transition rate corresponds to an absorption coefficient of $1.7 * 10^{-16}$ cm^2 (Eq. 7.4). This absorption coefficient is orders of magnitude larger than the absorption coefficient of the first step ($\sigma = 1 \times 10^{-21}$ cm^2) as expected.

7.3 High Sensitivity of the IR-LIF Detection Scheme

The strongest piece of evidence we have that demonstrates how sensitive the IR-LIF signal can be if it is resonantly enhanced at the two-photon level, is a spectrum that was recorded in the origin band region of acetylene ($V_0^0 K_0^1$)[29]. This spectrum includes a band that appears to the red of the origin band peaks, which has been identified as a hot band ($V_2^1 K_2^3$). The IR signal in the hot band region is interesting because the corresponding UV signal is very weak (Fig. 7-5). This suggests that the IR signal in the hot band region is being enhanced at the *two*-photon level while the UV signal is being reduced by two-photon destruction.

This is an encouraging result, since it implies that introduction of a second tunable laser would permit selective resonance enhancement, via *either* triplet or singlet Rydberg states of intact acetylene and would lead to a significant enhancement in IR signal intensity. The two-photon process giving rise to the IR signal we have observed for the origin band and for various subbands of the $\tilde{A}$ state proceeds through a resonant intermediate state and terminates in the Lorentzian wing of a strongly predissociated $Ry \leftarrow S_1$ transition. The sharp features of the IR-LIF spectra are a consequence of resonance at the one-photon level.

A significant enhancement in absorption is expected to happen when the second laser is tuned to a frequency which maximizes the overlap between the sharp intermediate state and the predissociated Rydberg state. In other words, instead of exciting the far-wing of a predissociation-broadened Ry ← (S$_1$,T) transition, if we can promote excitation at the line center (*i.e.* resonance at the *two* photon level), we can achieve significant enhancement in IR signal.

In Fig. 7-5, the ratio of IR-LIF to UV-LIF is 8 times larger in the hot band than it is

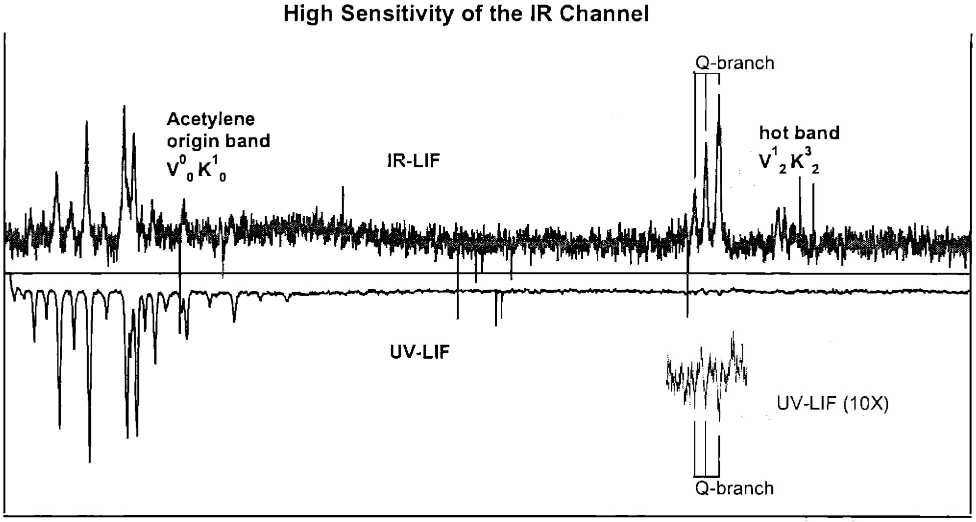

Figure 7-5: UV and IR-LIF spectra of vibronic bands in the acetylene $S_1 \leftarrow S_0$ $V_0^0K_0^1$ origin band region. Although the UV-LIF signal in the $V_2^1K_2^3$ two quanta of *trans*-bend hot band (~1200 cm^{-1} of vibrational excitation in a supersonic jet) is barely detectable, the IR signal is comparable in strength to the IR signal in the origin band. This is evidence of the fact that the hot band IR signal is being enhanced at the two-photon level while the one-photon UV signal is being suppressed. This figure is from Kevin L. Cunningham's thesis [29].

in the cold band [6]. The fact that the molecules have 1200 cm^{-1} of internal vibrational energy in the case of the hot band excitation, causes the second photon absorbed (recall that there is only one frequency of light exciting the molecules) to excite a different section of the predissociation-broadened Rydberg line (or possibly even a different line altogether). The enhancement in the overlap between the predissociated state and the intermediate state at this new energy translates into an enhancement in the IR signal level. Unfortunately it is not possible to accurately predict what the enhancement factor would be if the predissociated Rydberg line could be excited at the line-center. Due to absence of information about absorption strengths and frequencies of predissociated Rydberg lines, the only way to determine the enhancement factor is to perform a two-color experiment where the second laser can be continuously scanned to trace out the envelope of a predissociated Rydberg level. The two-photon IR-signal is expected to increase to a maximum as the second laser scans from the far-wing to the peak of the predissociated Rydberg line.

7.4 Significance of the IR-LIF Signal

The two-color IR-LIF experiment could become a very sensitive and selective scheme for characterizing the structure and dynamics of molecules in triplet states. The selectivity of IR-LIF for triplet states arises from the fact that photodissociation into the IR-emitting fragments can proceed through two pathways: singlet-mediated and triplet-mediated pathways. Singlet-mediated dissociation proceeds through a resonant intermediate state with a large singlet character and involves singlet Rydberg states of the parent molecule. Triplet-mediated dissociation, on the other hand, proceeds through a resonant intermediate state with a large triplet character and involves triplet Rydberg states of the parent molecule. By targeting triplet Rydberg states with the second tunable laser, one can select triplet-mediated dissociation of the parent molecule and obtain IR-LIF spectra that are related to the triplet character in

---

[6] Although the hot band signal is enhanced relative to the origin band signal, there is no reason to believe that the hot band transition is maximally enhanced at the second-photon level.

the intermediate states.

The advantages unique to the two-color IR-LIF scheme can be summarized as follows:

1) Extreme *sensitivity* due to resonance enhancement at the two-photon level. In fact, because of its sensitivity, two-color IR-LIF may be able to detect the exceedingly small population of excited molecules created in electronically forbidden $T_n \leftarrow S_0$ transitions at the one-photon level.

2) *Selectivity.* Singlet vs. triplet characters of the intermediate resonant states can be separately sampled by targeting $^3Ry \leftarrow\leftarrow S_0$ or $^1Ry \leftarrow\leftarrow S_0$ transitions. Singlet-mediated vs. triplet-mediated dissociation of the parent molecule will give rise to diagnostically different IR-LIF spectra recorded as the $(\mathrm{S}_1,\mathrm{T}) \leftarrow \mathrm{S}_0$ excitation laser is scanned. The IR-LIF spectra obtained via triplet-mediated dissociation will not follow the intensity profile of the UV-LIF signal from intermediate resonant states. However, the IR-LIF spectra obtained via the predissociated $^1\mathrm{Ry}$ state will more closely resemble the UV-LIF spectra. The two pathways are expected to have different dependences on laser intensity in the weak field limit where there are no saturation effects. IR signal from the singlet-mediated dissociation will obey the formal intensity law, *i.e.* quadratic dependence on laser intensity. IR signal from the triplet-mediated photodissociation may deviate from the formal intensity law. This is a consequence of the difference in the absorption cross-sections at the one-photon level between the two pathways and is explained in Section 7.5 using a rate equation approach.

3) The IR-LIF scheme can also find *general applicability.* Molecules that contain one or more multiple bonds or pairs of nonbonding electrons (diacetylene, cyanoacetylene, cyanogen, formaldehyde, biacetyl, propynal, acrolein ...) have properties that would make them good candidates for study by IR-LIF. The first excited triplet and, often, the first excited singlet states of these molecules lie below the lowest dissociation limit. Therefore, the spectra of these molecule are not complicated by effects of predissociation.

Molecules which contain the $-C \equiv C-$ and $-C \equiv N$ moieties are likely to dissociate into electronically excited photofragments analogous to the low-lying excited states of C_2H ($\tilde{A}^2\Pi$), CN($A^2\Pi_i$) [45]. This is because radicals such as CCH and CN with 9 valence electrons have a single vacancy in the nearly isoenergetic σ(sp-hybridized) and π(2p) molecular orbitals. As a result, transitions between these σ ($X^2\Sigma^+$) and π ($A^2\Pi$) states occur in the near IR or red region of the spectrum. When a photofragment has a low-lying electronically excited state, it should be possible to find members of a Rydberg series of the parent molecule that dissociate into near-IR emitting, electronically excited photofragments.

Owing to the presence of nonbonding electrons, unsaturated molecules are also characterized by spin-orbit interactions of magnitudes that make singlet$\sim$triplet coupling rate (10^{11} s^{-1} for a molecule such as acetylene) comparable to the rate of dissociation (ps timescale). Therefore, triplet states could be expected to play an important role in the dissociation process of unsaturated molecules. Since one of the strengths of the IR-LIF scheme is its capability to select and probe triplet states at the one- and two-photon levels, unsaturated molecules would be suitable candidates for study with this technique.

4) The two-color IR-LIF scheme may be *superior* to other techniques such as SEELEM in detecting forbidden $T_n \leftarrow S_0$ transitions. The most important reason for this is the fact that the IR-LIF scheme destroys the parent molecule and detects the IR emission from the resulting photofragments. Because of the large resonance enhancement factor, essentially every excited state created in a forbidden transition is converted into a detectable signal with 100% quantum efficiency. In other words, almost all molecules resonantly excited to the one-photon level will absorb another photon (of a different frequency) and dissociate. In contrast, techniques such as SEELEM rely on converting the intact parent molecule into a detectable signal. This entails preserving the parent molecule until it arrives at the detector surface. The efficiency of converting the excited parent molecule into signal is also much less than unity. The efficiency of detection is confounded by factors such as SEELEM surface cleanliness (Chapter 4). Therefore, if implemented correctly and successfully, the IR-LIF scheme has the potential to excel where other techniques fail.

7.5 Singlet-mediated vs. Triplet-mediated Photodissociation Pathways

Targeting triplet Rydberg states in a two-color IR-LIF experiment is expected to optimize the triplet-mediated dissociation pathway and enhance the selectivity of the IR-LIF channel for the intermediate states with large triplet character. Therefore, the IR-LIF signal can potentially be a very sensitive probe of "dominantly dark" resonant intermediate states. It can also provide new information about ^{3}Ry states because selecting states with large triplet character at the one-photon level will automatically target predissociated ^{3}Ry states at the two-photon level.

It is desirable to be able to distinguish the triplet-mediated pathway from the singlet-mediated pathway in order to understand and control which route to photodissociation is being taken by the excited molecules. The IR-LIF signal from a triplet-mediated dissociation process will not follow the corresponding UV-LIF signal profile because the resonant intermediate states of dominant triplet character will not contribute significantly to the UV-LIF signal. IR-LIF signal from a singlet-mediated pathway, on the other hand, will follow the UV-LIF signal since the resonant intermediate states of significant singlet character will precisely be the ones also contributing to the UV-LIF signal.

Triplet-mediated IR-LIF is also expected to have a different dependence on laser intensity than the singlet-mediated UV-LIF. The triplet-mediated IR-LIF signal is expected to have an apparent linear dependence on laser power at low flux because of the smaller cross-section of the absorption at the one-photon level (this transition would be from the singlet ground state to an eigenstate with a large triplet character). The singlet-mediated pathway will exhibit the I^2 intensity dependence expected for a two photon absorption process at low flux where saturation does not occur [7]. Therefore, dependence of the IR-signal on laser intensity could be a very useful diagnostic in distinguishing between the two pathways. The reason that the triplet-mediated

---

[7] Note that for the two pathways to exhibit diagnostically different dependence on laser intensity, one has to operate in the low-flux or non-saturation regime.

IR-LIF is expected to have an apparent linear dependence on laser power at low flux will be described next.

In multiphoton processes, the absorption rate constants are proportional to the cross sections of the one-photon steps as well as to the laser intensity. Therefore, if there is an appreciable difference in the cross sections of the one-photon events, this could alter the laser intensity dependence of the signal, even in the case of weak fields [89]. This will be outlined within the framework of a rate equation approach. The rate equation approach is suitable for studies of multiphoton processes because the large bandwidths of the lasers used in multiphoton experiments imply a short phase coherence time, and, hence, a minimal influence of coherence effects on multiphoton dynamics. Other approaches that are used in treating multiphoton events are time-dependent perturbation theory, the Green's function method, the density matrix method, and the susceptibility method [89]. Population rate equations can be derived from the density matrix equations and can be employed with confidence when the coherence properties of the system-laser field play an insignificant role in the dynamics. The rate equation approach has the advantage that it permits easy incorporation of physical phenomena such as irreversible, spontaneous decay (*e.g.* predissociation and radiationless relaxation) which are unique to molecular systems [153].

The rate equations associated with a simple model for resonant two-photon absorption that creates a final state w (the emitting photofragment C_2H^* in our case) from an initial state y (C_2H_2 in our case) through the resonant intermediate state x (an eigenstate of the $\tilde{A}$ electronic surface in our case) and the nonresonant state z (the predissociated Rydberg state in our case) can be expressed as,

$$\begin{aligned} d\rho_y(t)/dt &= -a\rho_y(t) + d\rho_x(t) \\ d\rho_x(t)/dt &= -d\rho_x(t) - b\rho_x(t) + a\rho_y(t) \\ d\rho_z(t)/dt &= b\rho_x(t) - c\rho_z(t) \\ d\rho_w(t)/dt &= c\rho_z(t) \end{aligned} \tag{7.5}$$

The schematic for this model is shown in Fig. 7-6. a is the transition rate from

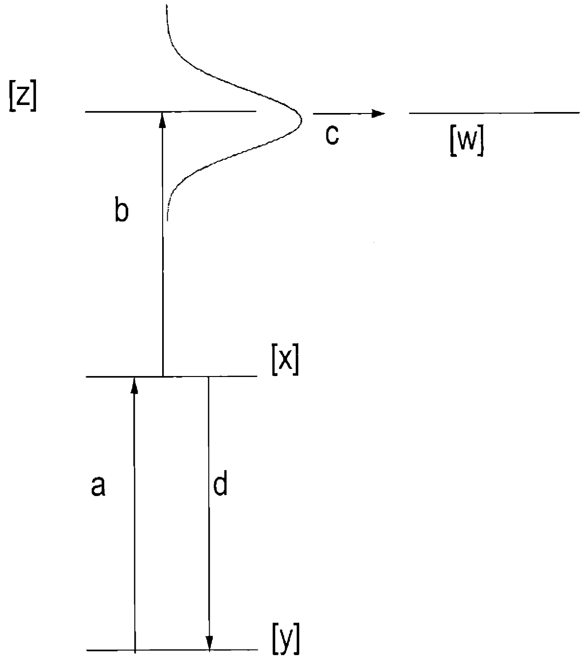

Figure 7-6: A schematic for a two-photon absorption event including an inital state y, a resonant intermediate state x, a non-resonant, broad state z, and a final state w.

the initial state y to the intermediate state x, d is the rate of population depletion of the intermediate state x due to stimulated emission and/or radiative decay, b is the transition rate from the resonant intermediate state x to the nonresonant intermediate state z, and c is the predissociation rate of state z into the final, emitting state w.

The coupled differential equations in Eq.(7.5) can be solved exactly using *Mathematica* assuming the initial conditions $\rho_y(t=0) = N_0$ and $\rho_x(t=0) = \rho_z(t=0) = \rho_w(t=0) = 0$. The exact equation which gives the rate of change of the population in the

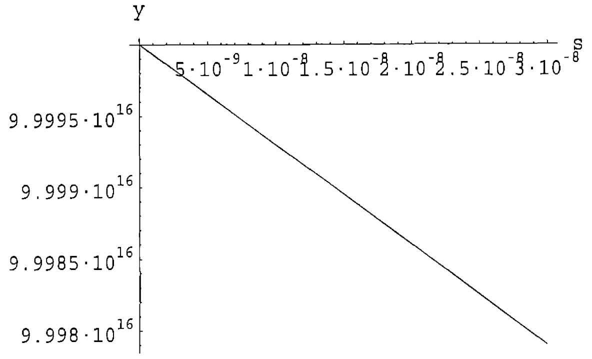

Figure 7-7: Change in the number of molecules/cm^3 that are in the initial state **y** as a function of time.

final state w as a function of time is given in Eq.(7.6).

$$\begin{aligned} d\rho_w(t)/dt &= \frac{-N_o abc E^{-\frac{1}{2}(a+b+d+\alpha)t} A}{D} \\ A &= 2c - d + \alpha - 2cE^{\alpha t} + dE^{\alpha t} + \\ &\quad \alpha E^{\alpha t} - 2\alpha E^{\frac{1}{2}(a+b-2c+d+\alpha)t} + \\ &\quad a(-1+E^{\alpha t}) + b(-1+E^{\alpha t}) \\ D &= 2[a(b-c) + c(-b+c-d)\alpha] \end{aligned} \tag{7.6}$$

The change in the number of species in each state (initial state **y**, intermediate state **x**, predissociated state **z**, and the product state **w**) is shown as a function of time in Figures 7-7, 7-8, 7-9, 7-10. The rate constants used for these plots were $a = 7 \times 10^3$ s^{-1}, $b = 2 \times 10^8$ s^{-1}, $c = 1 \times 10^{12}$ s^{-1}, $d = 7 \times 10^3$ s^{-1}. N$_0$ was assumed to be 1×10^{17}/cm^3 since this is the approximate number density of molecules in the laser excitation region in our experiment (Section 7.2).

It is interesting to note that, in this steady state approach, in a time window (0 - 3×10^{-8}s) that is relevant to the duration of the laser pulse (6×10^{-9}s), the equilibrium populations reached can be ordered as $y \gg x \cong w \gg z$. In other words, the population of the initial state **y** hardly changes (N$_0$ = 1×10^7/cm^3 was used as the initial value) while the population build-up in the predissociative state **z** attains a much smaller value than others.

In an attempt to assess the effect of laser intensity on the steady-state populations,

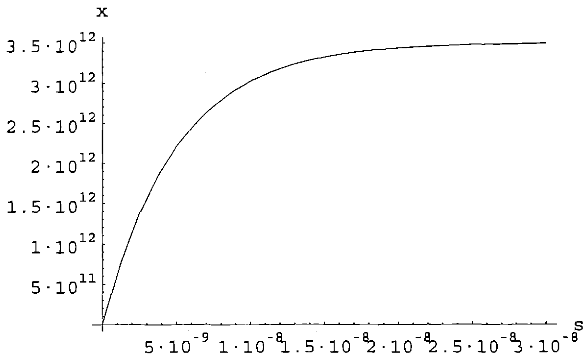

Figure 7-8: Change in the number of molecules/cm^3 that are in the intermediate state **x** as a function of time.

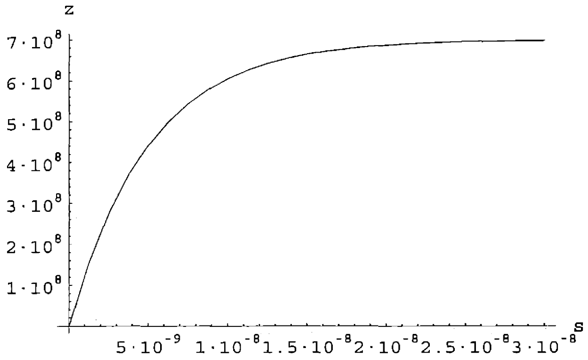

Figure 7-9: Change in the number of molecules/cm^3 that are in the predissociated state **z** as a function of time.

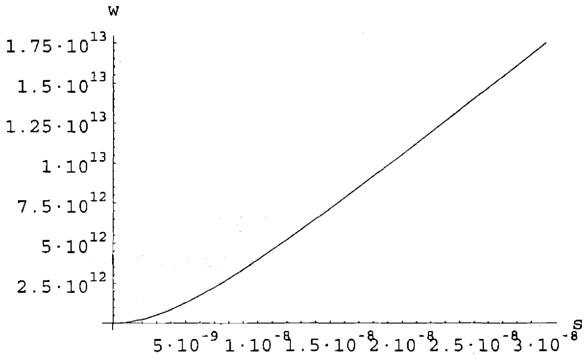

Figure 7-10: Change in the number of molecules/cm^3 that are in the product state **w** as a function of time.

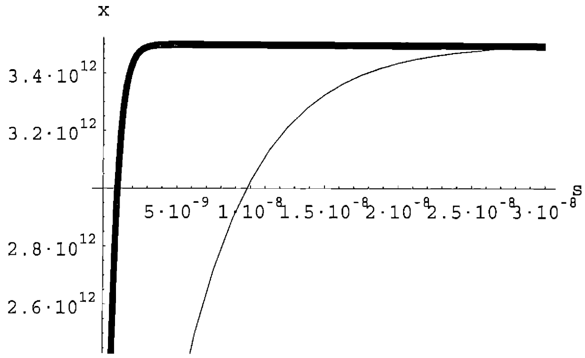

Figure 7-11: Change in the number of molecules/cm^3 that are in the intermediate state **x** as a function of time plotted for two laser intensities: I (light curve) and 10×I (thick curve). Equilibrium population is achieved much more quickly at high laser intensities.

the number of molecules/cm^3 in the intermediate state **x** was plotted as a function of time for two laser intensities differing by a factor of 10. As can be seen, although in the long-time limit, the equilibrium population of state **x** is the same for both laser intensities, this equilibrium population is reached much more quickly if the laser intensity is high. Figure 7-11 illustrates the difference in the two intensity regimes.

A few assumptions can be made to simplify Eq.(7.6) and obtain some physical insight into the production of the emitting state w. For the weak-field limit (*i.e.* low flux), stimulated emission can be assumed to be negligible (in other words the *rate* of stimulated emission (*i.e.* $d \times \rho_x$) can be assumed to be negligible in comparison to the rates of other events considered). The radiative lifetime of the resonant intermediate states (*i.e.* $\tilde{A}$ $3\nu_3$ states) are on the order of microseconds (Chapter 3). Since the duration of the laser pulse is $\sim 6 * 10^{-9}$ s, the effects of radiative relaxation can also be omitted. We can further assume that c, which is the predissociation rate of the state z, is much larger than a and b. The lifetimes of the predissociated Rydberg states are on the order of ps [62], and, hence, c is on the order of 10^{12} s^{-1}. We have previously determined that $a \approx 10^3$ s^{-1} and $b \approx a \times 10^4$ (Section 7.2). Incorporating these simplifications into Eq.(7.6) yields,

$$\begin{aligned} d\rho_w(t)/dt &\approx \frac{-N_o abc[E^{-at}(-2c) + E^{-ct}(2a-2b) + 2cE^{-bt}]}{D} \\ D &\approx 2c(-a-b+c)(b-a) \\ d\rho_w(t)/dt &\approx \frac{N_o ab[E^{-at} - E^{-bt}]}{b-a} \end{aligned} \tag{7.7}$$

In the case of weak laser field, in which the laser pulse duration, t_p, satisfies $at_p < 1$ and $bt_p < 1$, the formal intensity law, *i.e.* the quadratic dependence on laser intensity, holds:

$$\begin{aligned} \frac{d\rho_w(t)}{dt} &\approx abN_o tE^{-at} \\ &\approx abN_o t \\ &= \frac{\sigma_{xz}\sigma_{xy}}{\hbar^2\omega_r^2} N_o I^2 t \\ \text{since } b &= \frac{\sigma_{xz} I}{\hbar\omega_r} \end{aligned} \tag{7.8}$$

The last equality in Eq.(7.8) is the definition of a normalized one-photon absorption coefficient [30] and t here represents the duration of the laser pulse [8]. However, suppose there is a significant difference in the cross sections of the one-photon steps, as would be the case if the transition from the initial to the resonant intermediate state ($y \longrightarrow x$) was forbidden and the next absorption step ($x \longrightarrow z$) was allowed. Then we would have $\sigma_{xz} \gg \sigma_{yx}$ (*i.e* $b \gg a$) and Eq.(7.7) can be simplified to

$$\begin{aligned} d\rho_w(t)/dt &\approx aN_o E^{-at} \\ &\approx \frac{\sigma_{yx} I}{\hbar\omega_r} N_o E^{-at} \end{aligned} \tag{7.9}$$

As can be seen, in this special case, the two-photon process *can* exhibit a linear dependence on laser intensity.

---

[8] In this treatment, the specific shape of the laser pulse does not enter the calculation explicitly. In fact, in most rate-equation approaches, it is assumed that the pulse is a square pulse with constant intensity I in the duration $0 \le t \le t_p$.

7.6 The Two-Color IR-LIF Experiment

In the two-color IR-LIF scheme, the parameters that are important in obtaining efficient two-photon absorption and photofragment generation are the bandwidths of the two pulses and the time delay between them. Since we already know that the intermediate states are sharp resonances, it would be appropriate to use a narrow-bandwidth laser for the first absorption step. Using a large bandwidth laser could give rise to a broad background signal from absorption at the wings of the laser pulse. A pulse-amplified cw beam would be ideal for the first step since this beam would have a narrow bandwidth and still have high peak intensity.

The second pulse should be intense and can be broad since the predissociated Rydberg states are also broad (FWHM ≈ 30 cm^{-1} as calculated from the predissociation time of 1 ps). Whereas the first laser should be scanned at the highest possible resolution and tuned to single intermediate resonances, the second laser can be scanned at low resolution to cover large spectral regions. Operation of lasers in the low-resolution scanning mode without intracavity etalons (grating scans typically have a bandwidth of 0.4 cm^{-1}) is also characterized by pulse energies higher by about 50% compared to the high-resolution scanning mode.

The delay between the two pulses should be set to zero initially. Recent pump-probe experiments performed on the predissociated Rydberg states of acetylene [124] in which a 120 fs VUV (vacuum UV) pulse was used to populate an excited Rydberg state and a second short probe pulse was used to photoionize the prepared electronic state after a given time interval, have shown that the greatest ion yield was obtained when the two pulses were temporally overlapped (*i.e.* zero delay).

One issue that requires analysis in the two-color experiment is discrimination against signal that arises from absorption of only one laser frequency. In order to discriminate against this signal, one can use an "alternative data acquisition" scheme which was employed successfully by Takahashi *et al.* [136]. In this scheme, one laser would be operated at 10 Hz (the highest repetition rate that can be used in our experimental system since the nozzle operates at 10 Hz) and the other laser would be operated at 5 Hz by chopping alternative pulses. Two kinds of signals would be collected simultaneously: one would arise from the two-color absorption and the other would arise from absorption of the light from the 10 Hz laser. Both signals would be integrated separately. Subtracting the one-color spectrum from the two-photon absorption spectrum would eliminate the contribution from unwanted one-color signal.

It is important to realize that the alternative data acquisition scheme may not work effectively if the background contribution to two-photon signal is very large. It is necessary to suppress the background noise as much as possible, perhaps by using judiciously selected pulse intensities, before employing background substraction techniques. The rate equation approach outlined in Section 7.5 could be a good starting point to construct a quantitative model of the two-color experiment. The model presented in Section 7.5 assumes a single laser intensity (*i.e.* one laser) and treats the laser as a square pulse (*i.e.* the laser intensity stays constant during the duration of the pulse). It would be interesting to elaborate on this model by explicitly including two different lasers and computing the population profiles of the states at times when the laser pulse is off. Based on the findings, it may be possible to select wise values for the various parameters of the two-color experiment.

Chapter 8

Conclusion

Progress made so far in the investigation of the triplet states of acetylene and of the intersystem crossing process that populates these states, has given rise to new questions that will direct the future path of our quest. The experimental capability afforded by the second-generation apparatus has opened up the possibility of pursuing challenging projects such as observation of direct singlet-triplet transitions (Chapter 4). Equipped with our initial results, new experimental capabilities, and recently developed data analysis methods, we are in a position to refine and extend our questions regarding the triplet states of acetylene and radiationless electronic relaxation mechanisms.

The most interesting questions that came into focus during our exploratory experiments on the triplet states of acetylene are:

1) Can either SEELEM on low work-function metals (Chapter 4) or the two-color IR-LIF experiment (Chapter 7) be sensitive enough to detect direct singlet-triplet transitions in acetylene? Could either of these techniques find general applicability for other molecules if proven to have high sensitivity?

2) How would the SEELEM spectra of triplet states produced by different excitation methods (direct optical excitation, excitation by an electron gun [1], excitation by

---

[1] An electron gun is basically a filament - thorium oxide coated tungsten wire is usually used - which emits electrons upon being heated to temperatures in the range 1950° - 2150°. The electrons move away from the filament to an anode following a well-defined trajectory in a homogenous

energy transfer from photosensitized Hg [146] compare? In a direct optical transition the wavelength of the laser is scanned. In excitation by an electron gun, signal is recorded as the electron accelerating voltage is swept over a range of few tenths of eV centered at the electronic transition energy. In experiments which involve transfer of excitation energy from photosensitized species, molecules in a certain excited electronic state are created, there is no parameter that is scanned ($\tilde{a}^3B_2$ state of acetylene can be created by transfer of energy from photosensitized Hg [137]).

3) What is the mechanism of energy transfer from excited metastable molecules to metal surfaces (*i.e.* the mechanism of the SEELEM process)? We have shown that under high background pressures, the triplet de-excitation pathway becomes very inefficient and may even shut down (Chapter 4). This is a consequence of the fact that de-excitation of the triplet character of a metastable molecule occurs via a short-range interaction (*i.e.* tunnelling) pathway and, hence, is more sensitive to vacuum conditions. This empirical finding has been incorporated into the SEELEM signal expression as a scaling factor, $\alpha(p)$ (Chapter 4), which reduces the detectivity of the triplet character with respect to the singlet character as a function of background pressure. What is the numerical value of $\alpha(p)$ for a given molecule and background pressure? What is the quantitative dependence of $\alpha(p)$ on the background pressure p? Is $\alpha(p)$ a molecule-specific parameter or is it a universal parameter which describes how inefficient the triplet de-excitation pathway becomes relative to the singlet de-excitation pathway as the background pressure increases?

4) Can surfaces other than metals be used as SEELEM surfaces? The draw-

---

magnetic field. The voltage applied to the anode determines to what kinetic energy the electrons accelerate. The molecular beam passes through the beam of electrons emitted from the filament. During transit, the molecules may be promoted to excited levels if they collide with the electrons from the electron gun. However, in the excitation process, an exchange of electrons can happen such that an electron from the gun may replace the electron of the molecule being excited. In that case, the incoming electron may either go into a triplet or a singlet excited electronic state since its spin would be uncorrelated to that of the remaining hole in the HOMO of the molecule. Therefore, an electron gun can induce direct transitions between states of different multiplicity. A description of a successful electron gun (or bombarder) can be found in [48].

back of metal surfaces is that the low work-function metals are alkali metals, which are extremely reactive and, hence, difficult to work with. An intriguing alternative would be to use a semiconductor as the SEELEM surface. The challenge associated with this idea is to find an effective way to measure the minuscule current that would be generated from the promotion of an electron from the valence band of the semiconductor to its conduction band upon transfer of excitation energy from the incident metastable molecule. However, if semiconductors could be used as SEELEM surfaces, then one could continually vary the "SEELEM selectivity" to different electronic states by changing the band-gap of the semiconductor used. Semiconductors would afford continuous fine-tuning of SEELEM selectivity. In fact, direct detection of electron-hole pairs generated by chemical reactions on metal surfaces has been attempted by Nienhaus *et al.* [103, 102].

5) It is well-established that neither vibrational nor translational energy contributes to SEELEM detectivity [53]. Only the vertical electronic energy of the incident metastable molecule can give rise to ejection of electrons from the SEELEM surface if it exceeds the work function of the SEELEM metal. Considering that electronic motion occurs on a much faster time scale than nuclear motion (Born-Oppenheimer approximation), it is reasonable to assume that the coupling of molecular vibrational energy into the metal surface will not occur fast enough to contribute to the ejection of electrons from the SEELEM surface. However, vibrational excitation *can* turn on SEELEM detectivity by giving Franck-Condon access to a nuclear geometry for which the vertical electronic excitation energy is larger than the work function of the metal. It would be interesting to investigate this possibility by conducting an experiment where SEELEM detectivity can be measured as a function of the number of quanta of vibrational excitation in various vibrational modes. An empirically determined relationship between vibrational energy and SEELEM detectivity could reveal interesting trends.

The experiments planned to address some of these questions will be briefly summarized in the following sections.

8.1 Direct Singlet-Triplet Transitions

Preliminary results have shown that the sensitivity of SEELEM with Cs as the detection surface (Cs-SEELEM) is significantly enhanced relative to that of SEELEM with Au as the detection surface (Au-SEELEM) (Chapter 4). Therefore, it may be possible to detect direct singlet-triplet ($T_i \leftarrow S_0$) transitions using Cs as the SEELEM surface. The feasibility of such an attempt was discussed in Chapter 4. These experiments are currently ongoing. Observation of the desired signal will depend on how much the sensitivity limit of Cs-SEELEM can be improved [2] and whether the correct resonance regions will be scanned.

There have been several theoretical and experimental studies of the triplet excited states of acetylene [134, 148, 55, 94, 146, 137, 151]. The predicted equilibrium geometries for the low-lying excited triplet states and for the ground state of acetylene are given in Table 8.1.

Based on these *ab initio* studies, a schematic of the electronic states of acetylene and their relative energies is presented in Fig. 8-1.

Electron energy loss (EEL) spectra of acetylene was obtained both in the solid phase [134] and in the gas phase [148]. Energy-loss spectroscopy offers considerable advantages for the study of spin- or symmetry-forbidden electronic states. There were three distinct regions observed in the gas and solid phase EEL spectra of acetylene, which correlated surprisingly well with each other:

1) A region below 4.9 eV, which is reported to access the ^3B_u (T_1 *trans* well) and $^3B_2$ (T_1 *cis* well) states by Swiderek *et al.*

---

[2] The sensitiviy of Cs-SEELEM can be increased by improving the background pressure (and, hence, the S/N ratio) in the chamber. This can be achieved by cooling the Cs surface to reduce the background counts from thermionic electrons. A recent modification to the chamber, the installment of a magnetically coupled rotary feedthrough, is also expected to improve the background pressure. The magnetic feedthrough replaced the o-ring feedthrough which was used previously to introduce the rotating wheel shaft into vacuum. The o-ring seal was continuously eroded by the rotating motion of the rod, giving rise to small leaks. The magnetic feedthrough uses a magnetic fluid to make a seal against vacuum. Such a seal is not prone to being degraded by the rotating wheel shaft.

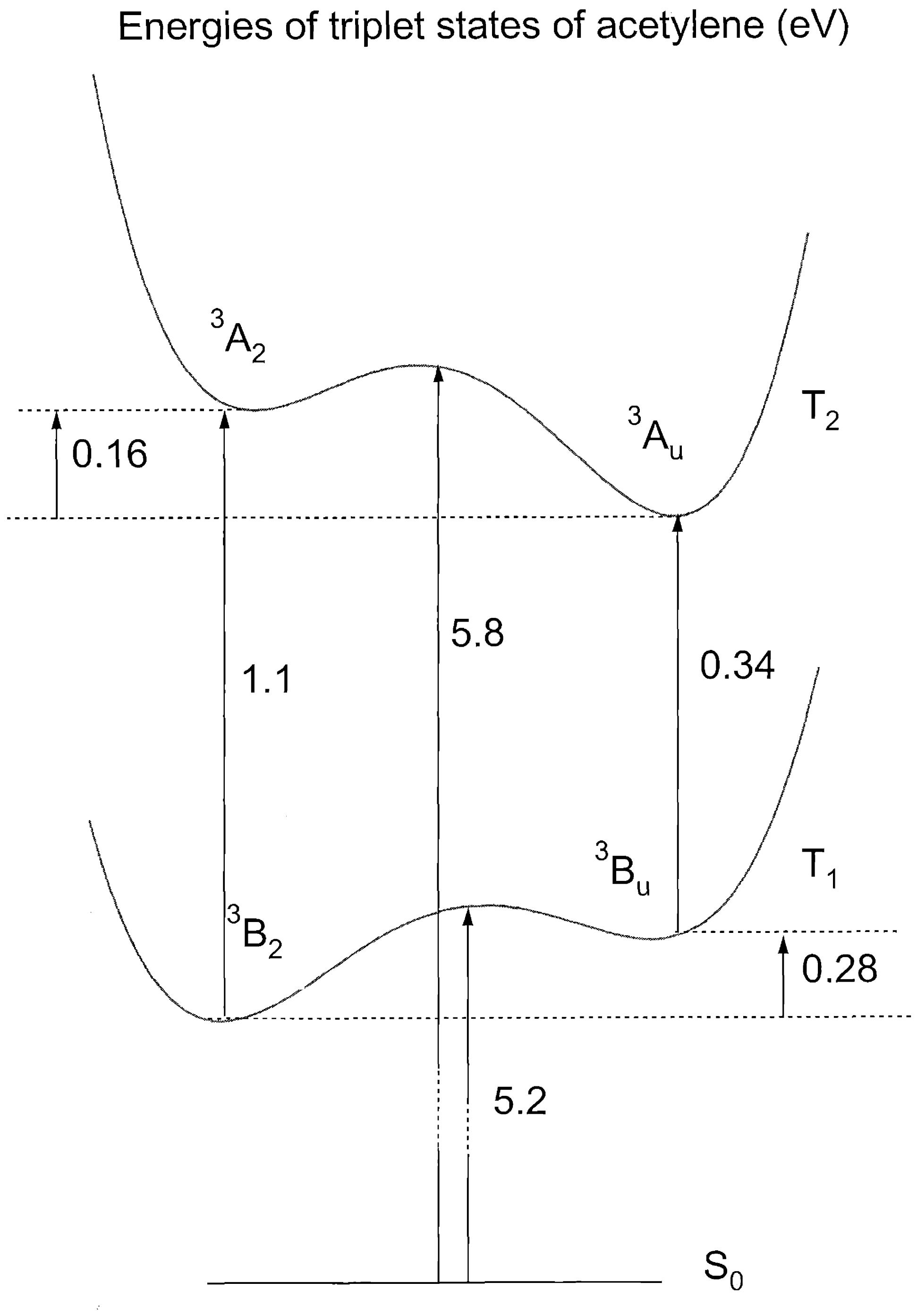

Figure 8-1: A schematic of the relative energies of the excited states of acetylene. T_2/T_3 are predicted to cross at 5.45 eV within C_2 symmetry and S_1/T_3 are predicted to cross at 5.64 eV within C_2 symmetry [28].

Table 8.1: Summary of theoretical predictions for acetylene ground and excited states [110]

Electronic state	r_e(CC) Å	r_e(CH) Å	θ_e(HCC)
$X^1\Sigma_g^+$	1.210	1.064	180.0°
$X^1\Sigma_g^{+*}$	1.210	1.064	180.0°
a^3B_2	1.340	1.091	128.0°
b^3B_u	1.345	1.082	131.5°
c^3A_u	1.386	1.094	120.5°
d^3A_2	1.360	1.095	130.3°

*Experimental results from Baldacci *et al.*([10])

2) A region between 4.9 eV and 5.7 eV, which Swiderek *et al.* and Wilden *et al.* claim contains vibrational progressions into the ^3A_u (T_2 *trans* well) state.

3) A region beyond 5.7 eV, which is complicated by contributions from the singlet excited state.

A threshold electron impact spectrum of acetylene was also obtained by Hammond *et al.* in the region 3.5 - 13.5 eV. Hammond and colleagues were able to obtain excitation energies of the acetylene Rydberg states with a $^2\Pi$ ion core in this experiment.

The EEL spectrum of acetylene has still not been conclusively assigned. There are still disagreements between experimentalists and theorists about the identification of the bands seen in the spectra. For example, Wilden and Swiderek [134, 148] assign the bands seen in the 4.9 eV - 5.7 eV region to $^3A_u \leftarrow {}^1\Sigma_g^+$ transitions. This region consists of three different parts: an irregular section between 4.43 eV and 4.56 eV, a short progression with three members and a spacing of 800 cm^{-1} between 4.62 eV and 4.82 eV, and a longer progression with an average spacing of 680 cm^{-1} between 4.97 eV and 5.56 eV. T_2 is the electronic energy surface that lies in this energy region according to *ab initio* calculations. However, T_2 has two stable minima: the *cis* well, $^3A_2$ and the *trans* well, ^3A_u. Swiderek claims that the long progression with an average spacing of 680 cm^{-1} cannot belong to $^3A_2$ since the $^3A_u \leftarrow {}^1\Sigma_g^+$ excitation spectrum should be dominated by a vibronic spacing of 771 cm^{-1}. This was shown by Wendt and *et al.* [146]. Therefore, by elimination, Swiderek claims the progression must belong to ^3A_u. Wilden also assigns this progression to the ^3A_u state. He, in fact, does not even consider $^3A_2$ since transitions to this electronic state are both spin and symmetry forbidden from the ground electronic state, and hence, should be at least 10 times weaker in EEL spectra, compared to other transitions.

Malsch *et al.*, on the other hand, representing theorists' sentiments, object to the assignment of the "680 cm^{-1} progression" to ^3A_u, claiming that the computed harmonic frequency for this level is 1137 cm^{-1}, a discrepancy just too large to be acceptable to the theorists. They claim that this progression probably belongs to the $^3A_2$ state. They point out that this progression dies out just as it approaches the calculated linear barrier of T_2. They also suggest an alternative assignment to either T_1 or T_3.

As can be seen, the observations in EEL spectra are yet to be conclusively described. This situation makes it even more exciting to be able to record spectra by direct optical excitation in this region. New data could contribute towards the resolution of the assignment issues.

It is also interesting that there is the possibility of at least one progression belonging to T_3 in the observed EEL spectra . However, as pointed out by Malsch *et al.* [94] the finding by Cui *et al.* [28] that T_3 is nonplanar makes this possible assignment rather unlikely. A strongly nonplanar structure should give rise to small Franck-Condon factors and it is, therefore, unlikely that a progression which is clearly visible down to 5 eV results from a nonplanar T_3 surface.

Table 8.2 is a compilation of the energies where EEL bands were observed [148] [3]. The tentative assignments of the features in each region were reported by Swiderek

---

[3] There is also a recent theoretical study reporting the excitation energies of the low-lying triplet states of acetylene [110]. According to this study $T_0(\tilde{a}^3B_2) = 30900 \pm 230$ cm^{-1}, $T_0(\tilde{a}^3B_u) = 33570 \pm 230$ cm^{-1}, $T_0(\tilde{b}^3A_2) = 38380 \pm 260$ cm^{-1}, and $T_0(\tilde{b}^3A_u) = 36040 \pm 260$ cm^{-1}.

et al. [134]. These should be the regions scanned in a direct singlet-triplet excitation scheme. The scanning should be done in a low-resolution mode to be able to cover large spectral regions with high-intensity pulses.

One modification that can be made to the current experimental set-up in order to increase the probability of exciting a direct singlet-triplet transition is the incorporation of a two-spherical mirror multipass cell which would allow efficient coupling of the laser beam to the collimated molecular beam at the center of the cell. Such a cell was used successfully by Kaur *et al.* for the direct absorption spectroscopy of jet-cooled acetylene, propyne, and 1-butyne in the 3-μm region [78].

The important parameters in the alignment of two spherical mirrors to achieve a certain number of passes and certain waist at the center where the multiple beams intersect the molecular jet, are the mirror separation and the relative vertical tilt of the mirrors with respect to the optical axis joining their centers of curvatures.

In the concentric limit where the separation between the two mirrors is exactly 2R where R is the radius of curvature, equally spaced spots (spacing = 2a) result in a straight line across each mirror. A small vertical tilt of one mirror separates the centers of curvature by a distance δ and causes the progression of spots to turn around into a circular, elliptical, or parabolic pattern. However, it is not practical to operate in the concentric limit since this limit does not allow "bunching" (*i.e.* focussing) of the beams into a tight waist at the center of the cell. Therefore, the distance between the mirrors (L) is usually set to a number slightly less than 2R. The fractional deviation of L from the concentric value is an important parameter and is given by,

$$\epsilon = (2R - L)/2R \tag{8.1}$$

This parameter controls the number of reflections, n, which may appear on each mirror. The number of spots on each mirror, in turn, controls the number of passes through the cell.

The focussing properties of the multipass cell are also important. The rays going through the cell collectively form a waist in the center of the cell with vertical dimension *a*, where *a* is the separation between two consecutive spots on the mirrors.

Table 8.2: Energies of the features observed in the EEL spectra of acetylene in the range 4-8 eV [148] (***It was observed that there is an increased intensity due to overlap of two bands at this energy.**)

eV	nm
Below 4.9 eV	$^3B_u/^3B_2$ bands
4.367±0.007	283.913±0.5
4.467±0.005	277.557±0.3
4.555±0.005	272.195 ± 0.3
4.645±0.005	266.921±0.3
4.735±0.005	261.847±0.3
4.829±0.005	256.750±0.3
4.9 - 5.7 eV	^3A_u progressions
*4.912±0.005	252.412±0.3
4.999±0.005	248.019±0.3
5.083±0.005	243.920±0.3
5.170±0.005	239.816±0.3
5.256±0.005	235.892±0.3
5.331±0.005	232.573±0.3
5.430±0.005	228.333±0.3
5.516±0.007	224.773±0.4
5.604±0.010	221.243±0.6

The horizontal thickness of this collective waist is the spot size of the individual laser rays at the center of the cell. The rays are equally spaced in the vertical dimension. If the rays are focussed loosely at the center, not all of them will be able to intersect the molecular jet and the expected multipass improvement will not be attained. An analysis of the multipass resonator is described by Trutna and Byer [139].

The parameters and their typical values used in the experiment by Kaur are given in Table 8.3.

The multipass cell idea was attempted by placing two spherical mirrors on either side of the molecular beam machine. The optical axis of the mirrors was perpendicular to the molecular beam axis. Preliminary visual alignment of the mirrors to obtain the desired elliptical pattern of spots using a helium-neon laser permitted the collinear UV laser beam to be adjusted without difficulty. However, it was found that getting the rays to focus to a tight spot at the center of the resonator was difficult. Another difficulty arose from the fact that at each pass, the rays were going through the laser entrance/exit windows and this was causing a reduction in energy by 10% for each pass. It was clear that a much better multipass cell design would place the spherical mirrors *inside* the chamber on motorized mounts which would facilitate external control of the mirror adjustments. Although the space in the source chamber for such an addition is tight, a carefully designed resonator could still fit in front of the nozzle between the two laser windows. The alignment of the mirrors would first have to be done on the bench and fine-alignment would be done with the external controls once the mirrors are inside the chamber under vacuum. Successful addition of such a multipass resonator to the source chamber would increase the singlet-triplet transition probability by a factor roughly proportional to the number of passes.

Table 8.3: Parameters and Typical Values for a Two-Spherical Mirror Multipass Resonator [78]

QUANTITY	SYMBOL	VALUE
Radius of curvature	R	101 mm
Mirror spacing	L	2R(1 - ϵ)
Fractional deviation of mirror spacing from concentricity	ϵ	1.5×10^{-3}
Vertical waist of ray pattern in center of cell	a	4 mm
Number of passes	N	41
Number of spots on each mirror	n	20
Wavelength	λ	3.0 μm
Spot size (center)	ω_0	0.06 mm
Spot size (at mirrors)	ω	1.6 mm

8.2 Relative SEELEM Detectivities of the Singlet vs. Triplet Characters of Metastable Molecules

An experiment that could shed light on the parameter $\alpha(\mathrm{p})$, which is a pressure-dependent measure of the relative SEELEM detectivities of the singlet vs. triplet characters of metastable molecules, would involve a molecular transition which has been well-studied, understood, and quantitatively described. If the singlet state characters of the eigenstates observed in the SEELEM spectrum of a molecular transition are known *a priori*, it would be possible to isolate the contribution of the triplet character to the SEELEM detectivity.

A good candidate for such an experiment would be the spin-forbidden $a^3\Pi \leftarrow X^1\Sigma^+$ transition of CO (Cameron bands). The $a^3\Pi$ state is the lowest triplet state of CO and most of the intensity of the forbidden a-X transition is due to the spin-orbit interaction of $a^3\Pi$ with $A^1\Pi$. There is a wealth of spectroscopic understanding of the CO $a^3\Pi \leftarrow X^1\Sigma^+$ system [46, 47]. The oscillator strength of the $a^3\Pi \leftarrow X^1\Sigma^+$ transition was determined to be $(1.50 \pm 0.1) \times 10^{-7}$ by James and the average lifetime of this state was calculated to be 9.51±0.63 msec [71]. In addition to the absorption studies done on the $a^3\Pi$ state of CO, this metastable state was also detected by SEELEM [131].

Simultaneously acquired SEELEM/UV-LIF spectra of the $a^3\Pi \leftarrow X^1\Sigma^+$ transition could reveal the value of the parameter $\alpha(\mathrm{p})$, at least for CO. Meijer and colleagues *were* able to observe fluorescence from the $a^3\Pi$ state of CO in their experiments which involved state-to-state scattering of metastable CO molecules from a LiF(100) surface [72]. Once the UV-LIF spectrum is assigned, the singlet character of the eigenstates can be determined from the known excited state Hamiltonian matrix [46]. Then, the corresponding eigenstates in the SEELEM spectrum can be identified and their signal strength can be compared to their *a priori* known singlet state character and non-singlet state character. A comparison of the SEELEM signal strengths of eigenstates with different fractional singlet characters would reveal a trend as to the contribution of the non-singlet character (*i.e.* triplet) of the eigenstates to their

SEELEM detectivity.

The advantage of this experiment lies in the fact that it does not require absolute SEELEM intensity measurements to be made. The quantitative information about α(p) can be obtained from the relative intensities of the SEELEM peaks.

This experiment could be repeated under different background pressures to determine the dependence of α(p) on vacuum conditions. The $a^3\Pi \leftarrow X^1\Sigma^+$ transition of CO can be excited using 206 nm light. Tunable radiation around this wavelength can be generated by doubling the output of a dye called Exalite 411 (Lambda Physik) which has a peak at 411 nm and a tunable range between 401-422 nm. The solvent used for Exalite 411 is p-dioxane. The output of the dye can be doubled in a type I $\beta-$barium borate (BBO) crystal cut at $\Theta = 83°, \Phi = 0°$.

One drawback is that, although this experiment may yield a quantitative value for α(p), it will leave open the question of whether the result can be generalized to other molecules as well. It would be necessary to carry out similar experiments on well-known transitions of other molecules to determine a range of α(p) values.

8.3 Can Vibrational Excitation Contribute to the SEELEM Process?

In order to address the question of whether vibrational energy plays a role in the SEELEM process, one would need to measure the SEELEM detectivity of a molecule as a function of vibrational excitation. To achieve this, one must populate a metastable state of the molecule which (1) possesses electronic excitation energy slightly lower [4] than the work function of a chemically stable surface (*i.e.* SEELEM surface) and, (2) exhibits a metastable lifetime longer than typical times of flight in molecular beam experiments of about 100-200 μs. Nitric oxide (NO) has a low lying quartet state, $a^4\Pi$, which could be a good candidate for this study. The other low lying quartet state, $b^4\Sigma^-$, is known to radiatively relax to the $a^4\Pi$ state and has an experimentally

---

[4] The deficiency should be such that it can be made up by several quanta of vibrational excitation.

determined fluorescence lifetime of 4 - 7 μs, which is short with respect to flight times in a typical SEELEM experiment [36]. The lifetime of the $a^4\Pi$ state, in comparison, is estimated to be 50 ms [36].

Since the first observation of direct optical excitation of the $a^4\Pi \leftarrow X^2\Pi$ bands of NO [22], high precision vibrational, rotational, and spin-coupling constants as well as an RKR potential, which is accurate at least up to 0.2 eV below the dissociation limit, for the $a^4\Pi$ state has been reported [36]. An extensive X/a (ground electronic state / low lying excited electronic state) Franck-Condon matrix calculated using the RKR potential is also available for this state. The electronic excitation energy of the $a^4\Pi$ state has been found to be 4.744 eV, greater than the work functions of many metals [64].

The direct excitation spectrum of the $a^4\Pi$ state in a molecular beam can be complicated by strong signal from the $B^2\Pi$ levels because energy transfer, due to perturbations between $a^4\Pi$ and $B^2\Pi$, following $a^4\Pi$ excitation favors emission out of the $B^2\Pi(v = 0, 3)$ states [23]. However, the unwanted signal from the $B^2\Pi \rightarrow X^2\Pi$ relaxation can be discriminated against by moving the boxcar gate to favor the delayed $a^4\Pi-$associated signal over the prompt $B^2\Pi$ signal [23].

In the first direct photoexcitation of the $a^4\Pi$ state, signal from the $v = 11$ level was observed [22]. The excitation was done with the doubled output of tunable radiation between 416-422 nm. Drabbels *et al.* was able to observe $a^4\Pi(v = 13-15)$ [36] taking advantage of the high spectral brightness of a pulse-amplified ring-dye-laser system (radiation near 200 nm with an energy of 0.5-1.0 mJ/pulse and a Fourier transform limited bandwidth of 180 MHz). The term energy of $a^4\Pi(v = 11)$ is 47930 cm^{-1} [23], which is higher than the work function of even Pt ($\Phi = 45938.669$ cm^{-1} or 5.7 eV). However, the electronic excitation energy of $a^4\Pi$ is only 4.744 eV [64], about 1 eV lower than Φ_{Pt}. Therefore, an experiment which is aimed at detecting SEELEM signal from metastable NO in the $a^4\Pi(v \geq 11)$ state on Pt could answer the question of whether vibrational energy can promote SEELEM detectivity. If vibrational energy *can* turn on detectivity by giving Franck-Condon access to a nuclear geometry for which the vertical electronic excitation energy is larger than the work function of the SEELEM metal, it should be possible to observe this effect by exciting different vibrational levels (and, hence, different excited state geometries) of the NO $a^4\Pi$ state.

The dependence of SEELEM detectivity on vibrational excitation can also be investigated in this experiment since it would be possible to obtain signal from different vibrational levels of the NO $a^4\Pi$ state. However, this is a more challenging investigation since it would require accurate normalization of the SEELEM signal between the different vibrational states populated. The number of excited metastable molecules created in each vibrational level will be a function of Franck-Condon factors and the SEELEM signal should be corrected for the number of molecules excited into each excited vibrational state. Since an extensive X/a Franck-Condon matrix is available for NO, accomplishing this should not, in principle, be very difficult.

As mentioned above, one mechanism by which vibrational energy can turn on SEELEM detectivity is by providing Franck-Condon access to a nuclear geometry for which the vertical electronic excitation energy is larger than the work function of the SEELEM metal. A second mechanism is suggested by the work of Wodtke and colleagues. Wodtke *et al.* have shown that high levels of vibrational excitation can promote electron transfer from a metal surface to a gas phase molecule [152] in their experiments which involved laser-preparation of specific quantum states of NO. They report that the dependence of the electron transfer rates on molecular vibration stems from the fact that the shape of the molecule changes upon charge transfer - vibrationally excited states may look more or less like the product ion. Vibrational excitation can enhance formation of anions because vibrational excursions can modulate the energetic barriers to electron transfer. Wodtke *et al.* have observed that large amounts of vibrational energy (8 vibrational quanta representing about 150 kJ/mol of energy) could be transferred from the NO molecule to the metal surface on a sub-picosecond (0.1 ps) timescale - a strong evidence for an electron-mediated process. In contrast, pure mechanical gas-surface vibrational relaxation of small molecules with large vibrational spacings on insulating surfaces occurs on a millisecond time-scale indicating that vibration couples very weakly to phonons of the solid [63].

As the study of Wodtke and colleagues [152] suggests, vibrational energy could be expected to play a role in the SEELEM process if it could somehow "prepare" the incident molecule "toward" its final state. Since there is no net charge transfer in the SEELEM process, the question becomes "what is the final state of the molecule?" Would there be any preference on the part of the molecule to populate a certain set of the neutral, electronically unexcited quantum states available to it after the collision with the SEELEM surface? Alternatively, vibrational excitation could play a role in the SEELEM process by modulating the electron affinity of the incident molecule. Electron affinity is a function of internuclear distance and is an important parameter in the SEELEM process, especially in the triplet-mediated short-range interaction pathway (Chapter 4). The short-range interaction pathway can be thought of as a sequential process in which a molecular ion is created which then gets neutralized by an electron from the conduction band of the SEELEM metal. Electron affinity would play a key role in the energetics of this sequential process. These ideas are offered merely to stimulate further reflection on this question in the light of the available theory regarding excited molecule-surface interactions [17]. If a vibrational dependence of the SEELEM signal is observed, this could open the door to refining the existing theories in the important area of gas-surface interactions.

Bibliography

[1] Photomultiplier tubes. RCA.

[2] H. Abe, S. Kamei, N. Mikami, and M. Ito. *Chem. Phys. Lett.*, (109)217, 1984.

[3] E. Abramson, C. Kittrell, J. L. Kinsey, and R. W. Field. Excitation spectroscopy of the acetylene $\tilde{A} - \tilde{X}$ transition in the 220 nm wavelength region. *J. Chem. Phys.*, (76)2293–2295, 1982.

[4] M. Ahmed, D. S. Peterka, and A. G. Suits. *J. Chem. Phys.*, (110)4248, 1999.

[5] S. Altunata and R. W. Field. *J. Chem. Phys.*, (113)6640, 2000.

[6] S. Altunata and R. W. Field. *J. Chem. Phys.*, (114)6557, 2001.

[7] N. Arutyunyan, G. A. Askar'yan, and V. A. Pogosyan. *Solv. Phys. - JETP (Engl. Transl)*, (3)548, 1970.

[8] N. R. Ashfold, B. Tutcher, B. Yang, Z. K. Jin, and S. L. Anderson. *J. Chem. Phys.*, (87)5105, 1987.

[9] P. Avouris, W. M. Gelbart, and M. A. El Sayed. *Chem. Revs.*, (77)793, 1977.

[10] A. Baldacci, S. Ghersetti, S. C. Hurlock, and K. Narahari Rao. *J. Mol. Spectrosc.*, (59)116, 1976.

[11] I. Becker and O. Cheshnovsky. *J. Chem. Phys.*, (101)3649, 1994.

[12] J. O. Berg. *Chem. Phys. Lett.*, (41)547, 1976.

[13] P. F. Bernath. *Spectra of Atoms and Molecules.* Oxford University Press, New York, 1995.

[14] M. Bixon and J. Jortner. *J. Chem. Phys.*, (48)715, 1967.

[15] Jack Cariou and Paul Luc. *Atlas Du Spectre D'Absorption de la Molecule de Tellur.* Technical report, Laboratoire AIME-Cotton CNRS II 91405 Orsay (France), 1980.

[16] B. L. Chadwick, D. A. King, L. Berzins, and B. J. Orr. *J. Chem. Phys.*, (91)7994, 1989.

[17] R. R. Chance, A. Prock, and R. Silbey. *Advances in Chemical Physics*, (37)1, 1978.

[18] Y. Chen, D. M. Jonas, J. L. Kinsey, and R. W. Field. *J. Chem. Phys.*, (91)3976, 1989.

[19] P. Y. Cheng, S. S. Ju, M. Y. Hahn, and H. L. Dai. Intersystem crossing of C_2H_2 (S_1) induced by Ar at different orientations: A van der Waals complex study. *Chem. Phys. Lett.*, (190)109–114, 1992.

[20] P. Y. Cheng, L. Lapierre, S. S. Ju, P. Derose, and H. L. Dai. Orientation dependence in collision-induced electronic relaxation studied through van der Waals complexes with isomeric structures. *Z. Phys. D.*, (31)105–115, 1994.

[21] O. Cheshnovsky and A. Amirav. *Chem. Phys. Lett.*, (109)368, 1984.

[22] R. A. Copeland, M. J. Dyer, D. C. Huestis, and T. G. Slanger. The NO($a^4\Pi$) state: direct photoexcitation from the ground state. *Chem. Phys. Lett.*, (236)350–355, 1995.

[23] P. C. Cosby, R. A. Copeland, D. G. Williamson, and G. Gaudin. The NO($a^4\Pi$) state: Spectroscopy of the $a^4\Pi_i \leftarrow X^2\Pi_r$ $11-0$ and $14-0$ bands. *J. Chem. Phys.*, (107)(7)2249–2256, 1997.

[24] Q. Cui and K. Morokuma. Personal Communication.

[25] Q. Cui and K. Morokuma. *Ab initio* MO studies on the photodissociation of C_2H_2 from the S_1 $(^1\tilde{A}_u)$ state. II. Mechanism involving triplet states. *Chem. Phys. Lett.*, (272)319–327, 1997.

[26] Q. Cui and K. Morokuma. *Ab initio* molecular orbital studies on the structure, energies and photodissociation of the electronic excited states of C_2H. *J. Chem. Phys.*, (108)626, 1998.

[27] Q. Cui, K. Morokuma, and J. F. Stanton. *Chem. Phys. Lett.*, (7)19, 1970.

[28] Q. Cui, K. Morokuma, and J. F. Stanton. *Ab initio* MO studies on the photodissociation of C_2H_2 from the S_1 (^1A_u) state. I. Non-adiabatic effects and S-T interaction. *Chem. Phys. Lett.*, (263)46, 1996.

[29] K. L. Cunningham. *The Surface Ejection of Electrons by Laser Excited Metastables Spectroscopy of Acetylene.* Ph.D. Thesis, MIT, 2000.

[30] G. P. Das, R. Vaia, A. T. Yeates, and D. S. Dudis. A theoretical model for excited state absorption. *Synthetic Metals*, (116)281–283, 2000.

[31] D. Demoulin. *Chem. Phys.*, (11)329, 1975.

[32] T. G. Dietz, M. A. Duncan, A. C. Pulu, and R. E. Smalley. *J. Chem. Phys.*, (86)4026, 1982.

[33] T. G. Dietz, M. A. Duncan, and R. E. Smalley. *J. Chem. Phys.*, (76)1227, 1982.

[34] S. Doli. *J. Chem. Phys.*, (72)3880, 1980.

[35] M. Drabbels, J. Heinz, and W. L. Meerts. *J. Chem. Phys.*, (100)(1)165, 1994.

[36] M. Drabbels, C. G. Morgan, and A. M. Wodtke. The spin-frobidden $a^4\Pi(v = 13{-}15)$ and $b^4\Sigma^-(v = 3) \leftarrow X^2\Pi(v = 0)$ bands of nitric oxide: A new scheme for quantum state-specific high-resolution kinetic energy measurements. *J. Chem. Phys.*, (103)(18)7700–7707, 1995.

[37] S. Drucker, J. P. O'Brien, P. Patel, and R. W. Field. *J. Chem. Phys.*, (106)3423, 1997.

[38] D. DuFlot, J. M. Robbe, and J. P. Flament. *Ab inito* potential energy surfaces for $C_2H \rightarrow C_2 + H$ photodissociation. *J. Chem. Phys.*, (100)1236, 1994.

[39] M. A. Duncan, T. G. Dietz, M. G. Liverman, and R. E. Smalley. *J. Chem. Phys.*, (85)7, 1981.

[40] P. Dupré. *Chem. Phys.*, (196)239, 1995.

[41] P. Dupré and P. G. Green. *Chem. Phys. Lett.*, (212)555, 1993.

[42] P. Dupré, P. G. Green, and R. W. Field. *Chem. Phys.*, (196)211, 1995.

[43] P. Dupré, R. Jost, M. Lombardi, P. G. Green, E. Abramson, and R. W. Field. *Chem. Phys.*, (152)(1)293, 1991.

[44] M. A. El Sayed. *Accounts Chem. Res.*, (1)8, 1968.

[45] R. W. Field. "Long-Lived, Energetic States of Small Molecules". PRF Research Proposal, 2000.

[46] R. W. Field. *Spectroscopy and Perturbation Analysis in Excited States of CO and CS.* Ph.D. Thesis, Harvard, 1971.

[47] R. W. Field, S. G. Tillford, R. A. Howard, and J. D. Simmons. *J. Mol. Spec.*, (44)347, 1972.

[48] R. S. Freund. *Molecular Beam Spectrum of Metastable CO.* Ph.D. Thesis, Harvard, 1965.

[49] R. S. Freund and W. Klemperer. *J. Chem. Phys.*, (47)2897, 1967.

[50] K. M. Gough and W. F. Murphy. *J. Mol. Struct.*, (224)73, 1990.

[51] P. G. Green, J. L. Kinsey, and R. W. Field. *J. Chem. Phys.*, (91)5160, 1989.

[52] F. C. Hagemeister, C. A. Arrington, B. J. Giles, B. Quimpo, L. Zhang, and T. S. Zwier. Cavity ringdown methods for studying intramolecular and intermolecular dynamics, In *Cavity Ring-down Spectroscopy: An Ultratrace-Absorption Measurement Technique.* , K. S. Busch and M. A. Busch, editors, number 720, pages 210–232, UK, 1999. ACS, Oxford University Press.

[53] H. D. Hagstrum. *Phys. Rev.*, (96)325, 1954.

[54] C. E. Hamilton, R. W. Field, T. R. Huet, and M. Herman. *J. Mol. Spectrosc.*, (137)427, 1989.

[55] P. Hammond, J. Jureta, D. Cvejanović, G. C. King, and F. H. Read. The threshold electron impact spectrum of acetylene. *J. Phys. B: At. Mol. Phys.*, (20)3547–3556, 1987.

[56] N. Hashimoto, N. Yonekura, and T. Suzuki. Pump-probe measurements of the predissociation reaction time of C_2H_2 from (^1A_u) state. *Chem. Phys. Lett.*, (264)545-550, 1997.

[57] J. C. Hemminger, B. G. Wicke, and W. Klemperer. *J. Chem. Phys.*, (65)2798, 1976.

[58] J.C. Hemminger, B.G. Wicke, and W. Klemperer. Delocalization of electronic energy in the lowest triplet staes of molecules. *J. Chem. Phys.*, (65)2798–2804, 1976.

[59] M. Herman, T. R. Huet, and M. Vervloet. *Mol. Phys.*, (66)333, 1989.

[60] V. W. Horneman, S. Alanko, and J. Hietanen. *J. Mol. Spectrosc.*, (135)191, 1989.

[61] H. Hotop. *Experimental Methods in the Physical Sciences*, (29B)191, 1996.

[62] Y. C. Hsu, M. S. Lin, and C. P. Hsu. *J. Chem. Phys.*, (94)7832, 1991.

[63] C. Huan-Cheng and G. E. Ewing. *Phys. Rev. Lett.*, (65)2125–2128, 1990.

[64] K. P. Huber and M. Vervloet. *J. Mol. Spectrosc.*, (129)1988, 1988.

[65] T. R. Huet, M. Godefroid, and M. Herman. *J. Mol. Spectrosc.*, (144)32, 1990.

[66] T. R. Huet and M. Herman. *J. Mol. Spectrosc.*, (137)396, 1989.

[67] T. R. Huet, M. Herman, and J. W. C. Johns. *J. Chem. Phys.*, (94)3407, 1991.

[68] S. J. Humphrey, C. G. Morgan, A. M. Wodtke, K. L. Cunningham, S. Drucker, and R. W. Field. *J. Chem. Phys.*, (107)(1)49, 1997.

[69] C. K. Ingold and G. W. King. *J. Chem. Soc.*, ()2702–2745, 1953.

[70] K. K. Innes. *J.Chem.Phys.*, (22)863, 1954.

[71] T. C. James. Intensity Measurements of the 0, 0 Band of the $a^3\Pi - X^1\Sigma$ Cameron System of CO. *J. Mol. Spec.*, (40)545–553, 1971.

[72] R. T. Jongma, G. Berden, D. van der Zande, T. Rasing, H. Zacharias, and G. Meijer. State-to-state Scattering of Metastable CO Molecules from a LiF(100) Surface. *Phys. Rev. Lett.*, (78)1375-1378, 1997.

[73] R. T. Jongma, T. Rasing, and G. Meijer. *J. Chem. Phys.*, (102)1925, 1995.

[74] S. S. Ju, P. Y. Cheng, M. Y. Hahn, and H. L. Dai. Isomeric structures of the electronically excited acetylene Ar complex: Spectroscopy and potential calculations. *J. Chem. Phys.*, (103)2850–2862, 1995.

[75] S. Kamei, N. Mikami, and M. Ito. *J. Chem. Phys.*, (90)2321, 1986.

[76] S. Kamei, K. Okuyamam, H. Abe, N. Mikami, and M. Ito. *J. Chem. Phys.*, (90)93, 1986.

[77] W. E. Kammer. *Chem. Phys. Lett.*, (6)529, 1970.

[78] D. Kaur, A. M. de Souza, J. Wanna, S. A. Hammad, L. Mercorelli, and D. S. Perry. Multipass cell for molecular beam absorption spectroscopy. *Applied Optics*, (29)119-124, 1990.

[79] G. W. King and C. K. Ingold. *Nature*, (169)1101, 1952.

[80] J. L. Knee and P. M. Johnson. *J. Chem. Phys.*, (80)13, 1984.

[81] W. J. Lafferty and A. S. Pine. *J. Mol. Spectrosc.*, (141)223, 1990.

[82] W. D. Lawrance and A. E. W. Knight. *J. Phys. Chem. A*, (95)7557, 1991.

[83] W. D. Lawrance and A. E. W.Knight. *J. Chem. Phys.*, (89)917, 1985.

[84] W. D. Lawrance and A. E. W.Knight. *J. Chem. Phys.*, (95)7557, 1991.

[85] H. Lefebvre-Brion and R. W. Field. *Perturbations in the Spectra of Diatomic Molecules.* Academic Press, Orlando, 1986.

[86] H. Lefebvre-Brion and F. Guerin. *J. Phys. Chem. A*, (49)1446, 1968.

[87] K. H. Lehmann. *J. Chem. Phys.*, (91)2759, 1989.

[88] K. K. Lehmann. *J. Phys. Chem. A*, (95)7556, 1991.

[89] S. H. Lin, Y. Fujimura, H. J. Neusser, and E. W. Schlag. *Multiphoton Spectroscopy of Molecules.* Academic Press, Orlando, 1984.

[90] H. Lischka and A. Karpfen. *Ab initio* calculations on the excited states of π systems. I. Valence excitation in acetylene. *Chem. Phys.*, (102)77–89, 1986.

[91] J. M. Lisy and W. Klemperer. *J. Chem. Phys.*, (72)3880, 1980.

[92] P. Löffler, E. Wrede, L. Schneider, J. B. Halpern, W. M. Jackson, and K. H. Welge. Dissociation dynamics of acetylene Rydberg states as a function of excited state lifetime. *J. Chem. Phys.*, (109)5231–5245, 1998.

[93] J. K. Lundberg and R. W. Field. *J. Chem. Phys.*, (98)8384, 1993.

[94] K. Malsch, R. Rebentisch, P. Swiderek, and G. Hohlneicher. Excited states of acetylene: a CAPSPT2 study. *Theor. Chem. Acc.*, (100)171–182, 1998.

[95] N. J. Mason and W. R. Newell. *Meas. Sci. Technol.*, (2)568, 1991.

[96] J. R McDonald, A. P. Baronavski, and V. M. Donnelly. Multiphoton-Vacuum-Ultraviolet Laser Photodissociation of Acetylene: Emission From Electronically Excited Fragments. *Chem. Phys.*, (33)161–170, 1978.

[97] T. A. Miller. Chemistry and Chemical Intermediates in Supersonic Jet Expansions. *Science*, (223)545–553, 1984.

[98] A. Moravec, G. Winnewisser, K. M. T. Yamada, and C. E. Bloom. *Z. Naturforsch*, (A45)946, 1990.

[99] D. H. Mordaunt and M. N. R. Ashfold. Near ultraviolet photolysis of C_2H_2: A precise determination of D_0(HCC−H). *J. Chem. Phys.*, (101)2630–2631, 1994.

[100] N. Moriwaki, T. Tsuchida, Y. Takehisa, and N. Ohashi. *J. Mol. Spectrosc.*, (137)230, 1989.

[101] R. S. Mulliken. *Phys. Rev.*, (60)506, 1941.

[102] H. Nienhaus, H. S. Bergh, B. Gergen, A. Majumdar, W. H. Weinberg, and E. W. McFarland. Electron-Hole Pair Creation at Ag and Cu Surfaces by Adsorption of Atomic Hydrogen and Deuterium. *Phys. Rev. Lett.*, (82)446–449, 1999.

[103] H. Nienhaus, H. S. Bergh, B. Gergen, A. Majumdar, W. H. Weinberg, and E. W. McFarland. Direct detection of electron-hole pairs generated by chemical reactions on metal surfaces. *Surf. Sci.*, (445)335–342, 2000.

[104] N. Ochi and S. Tsuchiya. Quantum beat spectroscopy of Zeeman splitting and level anticrossing of rotationally selected acetylene ($\tilde{A}\ ^1A_u\ 3\nu_3$) under weak magnetic fields. *Chem. Phys. Lett.*, (140)20–25, 1987.

[105] N. Ochi and S. Tsuchiya. Rovibronic level structure of electronically excited acetylene ($\tilde{A}\ ^1A_u$) in a supersonic jet as studied by laser-induced fluorescence and Zeeman quantum beat spectroscopy. *Chem. Phys.*, (152)319–336, 1991.

[106] N. Ohmori, T. Suzuki, and M. Ito. *J. Chem. Phys.*, (92)1086, 1988.

[107] C. E. Otis, J. L. Knee, and P. M. Johnson. *J. Chem. Phys.*, (78)2091, 1983.

[108] A. Penner, Y. Oreg, E. Villa, E. C. Lim, and A. Amirav. *Chem. Phys. Lett.*, (150)243, 1988.

[109] A. S. Pine and J. P. Looney. *J. Chem. Phys.*, (94)3407, 1991.

[110] C. D. Sherrill, E. F. C. Byrd, and M. Head-Gordon. Complete basis set extrapolations for low-lying triplet electronic states of acetylene and vinylidene. *J. Chem. Phys.*, (113)1447–1454, 2000.

[111] C. D. Sherrill, G. Vacek, Y. Yamaguchi, III H. F. Schaefer, J. F. Stanton, and J. Gauss. The $\tilde{A}$ ^1A_u state and the T_2 potential surface of acetylene: Implications for triplet perturbations in the fluorescence spectra of the $\tilde{A}$ state. *J. Chem. Phys.*, (104)8507–8515, 1996.

[112] Y. Shi and T. Suzuki. Formation of metastable triplet acetylene from the $\tilde{A}$ (^1A_u) state near the dissociation threshold. *J. Phys. Chem. A*, (102)7417–7419, 1998.

[113] F. Shokoohi, T. A. Watson, H. Reisler, F. Kong, A. M. Renlund, and C. Wittig. Photolytic Production of C_2H: Collisional Quenching of $\tilde{A}^2\Pi \rightarrow \tilde{X}^2\Sigma^+$ Infrared Emission and the Removal of Excited $C_2H^\dagger$. *J. Phys. Chem. A*, (90)5695–5700, 1986.

[114] R. E. Smalley. *J. Phys. Chem. A*, (86)3504, 1982.

[115] B. C. Smith and J. S. Winn. *J. Chem. Phys.*, (94)4120, 1991.

[116] O. Sneh, A. Amirav, and O. Cheshnovsky. *J. Chem. Phys.*, (91)7154, 1989.

[117] O. Sneh and O. Cheshnovsky. *Chem. Phys. Lett.*, (130)53, 1986.

[118] O. Sneh and O. Cheshnovsky. *Chem. Phys. Lett.*, (130)487, 1986.

[119] O. Sneh and O. Cheshnovsky. *Chem. Phys. Lett.*, (146)216, 1988.

[120] O. Sneh and O. Cheshnovsky. *Israel Journal of Chemistry*, (30)13, 1990.

[121] O. Sneh and O. Cheshnovsky. *J. Phys. Chem. A*, (95)7154, 1991.

[122] O. Sneh and O. Cheshnovsky. *J. Chem. Phys.*, (96)8095, 1992.

[123] O. Sneh, D. Dünn-Kittenplon, and O. Cheshnovsky. *J. Chem. Phys*, (91)7331, 1989.

[124] S. L. Sorensen, O. Björneholm, I. Hjelte, T. Kihlgren, G. Öhrwall, S. Sundin, S. Svensson, S. Buil, D. Descamps, A. L'Huillier, J. Norin, and C. G. Wahlström. Femtosecond pump-probe photoelectron spectroscopy of predissociative Rydberg states in acetylene. *J. Chem. Phys.*, (112)8038–8042, 2000.

[125] L. H. Spangler, Y. Matsumoto, and D. W. Pratt. *Phys. Chem.*, (87)4781, 1983.

[126] L. H. Spangler and D. W.Pratt. *J. Chem. Phys.*, (84)4789, 1986.

[127] L. H. Spangler, D. W.Pratt, and F. W. Birss. *J. Chem. Phys.*, (85)3229, 1986.

[128] S. Speiser and J. Jortner. *Chem. Phys. Lett.*, (44)399, 1976.

[129] S. Speiser and S. Kimel. *Chem. Phys. Lett.*, (263)46, 1996.

[130] J. C. Stephenson, J. A. Blazy, and D. S. King. Spectroscopy and collisional quenching rates for $\tilde{A}$ C_2H_2 ($\nu_3 = 0, 1, 2$). *Chem. Phys.*, (110)31–38, 1984.

[131] R. C. Stern, R. H. Gammon, M. E. Lesk, R. S. Freund, and W. A. Klemperer. *J. Chem. Phys.*, (52)3467, 1970.

[132] A. Sur and P. M. Johnson. *J. Chem. Phys.*, (84)1206, 1986.

[133] T. Suzuki, Y. Shi, and H. Kohguchi. Detection of metastable triplet acetylene produced by intersystem crossing from the excited $\tilde{A}$ (^1A_u) state. *J. Chem. Phys.*, (106)5292–5295, 1997.

[134] P. Swiderek, M. Michaud, and L. Sanche. *J. Chem. Phys.*, (106)9403, 1997.

[135] M. Takahashi, M. Fujii, and M. Ito. *J. Chem. Phys.*, (96)6486, 1992.

[136] M. Takahashi, M. Fujii, and M. Ito. Two-color double resonance spectroscopy via ^1A_u state of acetylene: 3p Rydberg state and its Renner-Teller effect. *J. Chem. Phys.*, (96)6486–6494, 1992.

[137] K. Tanigawa and H. Kanamori. "High-Resolution Study of Triplet Acetylene". Personal Communication.

[138] J. L. Tomer, K. W.Holtzclaw, and D. W. Pratt. *J. Chem. Phys.*, (88)1528, 1988.

[139] W. R. Trutna and R. L. Byer. Multiple-pass Raman gain cell. *Applied Optics*, (19)301–312, 1980.

[140] A. L. Utz, J. D. Tobiason, M. E. Carrasquillo, L. J. Sanders, and F. F. Crim. The direct observation, assignment, and partial deperturbation of the ν_4 and ν_6 vibrational fundamentals in $\tilde{A}^1A_u$ acetylene (C_2H_2). *J. Chem. Phys.*, (98)2742–2753, 1993.

[141] G. Vacek, C. D. Sherrill, Y. Yamaguchi, and III H. F. Schaefer. *J. Chem. Phys.*, (104)1774, 1996.

[142] J. Vander Auwera, T. R. Huet, M. Herman, C. E. Hamilton, J. L. Kinsey, and R. W. Field. *J. Mol. Spectrosc.*, (137)381, 1989.

[143] E. Villa, A. Amirav, and E. C. Lim. *Chem. Phys. Lett.*, (147)43, 1988.

[144] E. Villa, M. Terazima, and E.C. Lim. *Chem. Phys. Lett.*, (129)336, 1986.

[145] J. K. G. Watson. *J. Mol. Spectrosc.*, (), August 2001.

[146] H. R. Wendt, H. Hippler, and H. E. Hunziker. *J. Chem. Phys.*, (70)4044, 1979.

[147] R. W. Wetmore and H. F. Schaefer. Triplet electronic states of acetylene: *cis* and *trans* structures and energetics. *J. Chem. Phys.*, (69)1648–1654, 1978.

[148] D. G. Wilden, P. J. Hicks, and J. Comer. *J. Phys. B: Atom. Molec. Phys.*, ()L403, 1977.

[149] G. Winkelhofer, R. Janoscheck, F. Fratev, and P. von R. Schleyer. *Croat. Chim. Acta*, (56)509, 1983.

[150] G. Wlodarczak, J. Demaison, J. Burie, and M. C. Lasne. *Mol. Phys.*, (66)669, 1989.

[151] Y. Yamaguchi, G. Vacek, and H. F. Schaefer. *Theo. Chim. Acta*, (86)97, 1993.

[152] H. Yuhui, C. T. Rettner, D. J. Auerbach, and A. M. Wodtke. Vibrational Promotion of Electron Transfer. *Science*, (290)111–114, 2000.

[153] D. S. Zakheim and P. M. Johnson. Rate Equation Modelling of Molecular Multiphoton Ionization Dynamics. *Chem. Phys.*, (46)263–272, 1980.

[154] A. R. Ziv and W. Rhodes. *J. Chem. Phys.*, (65)4895, 1976.